

DISS. ETH NO. 20913

Experimental Analysis of Aggregate Breakup in Flows Observed by Three Dimensional Particle Tracking Velocimetry

A dissertation submitted to

ETH ZURICH

for the degree of

Doctor of Sciences

presented by

DEBASHISH SAHA

M. Sc. Chem. Eng., Technische Universität Dortmund

Date of birth

February 18, 1982

citizen of

Bangladesh

accepted on the recommendation of

Prof. Dr. W. Kinzelbach, examiner

Prof. Dr. M. Morbidelli, co-examiner

Dr. B. Lüthi, co-examiner

Dr. M. Holzner, co-examiner

2013

Abstract

Breakup of fractal aggregates in laminar and turbulent flow has been investigated experimentally by three dimensional particle tracking velocimetry (3D-PTV). The motivation of the thesis is to understand the breakup mechanism in Lagrangian frame so that the entire history of the flow dynamics around the aggregate can be unveiled. This will render access to the intriguing evolution of the "character" of the key parameters responsible for breakup. Our current understanding on aggregate breakup within the scope of experiment and numerics is limited to measuring the average size distribution and proposing the so called breakage kernels accordingly. This is where we bring forward the essential question which is: What is the Lagrangian contribution of the flow field to which an aggregate is exposed to for a certain time before it breaks apart?

Our intention to investigate breakup aligns with this question throughout this work which involves some stand alone features worth mentioning. We take the advantage of the capability of 3D-PTV to simultaneously measure the full tensor of the velocity gradient, $\frac{\partial u_i}{\partial x_j}$, around the aggregate and track it in a Lagrangian way while looking at the breakage phenomena as it happens. That means we come to know how an aggregate along its life time is experiencing the instantaneous velocity gradients which in turn will complement our present knowledge on breakup mechanism. Finite size non inertial aggregates are injected into the flow individually which ensures that the carrier fluid property is not subject to change due to high concentrations of the particle phase and technically it is easier to track a single breakage event once at a time. First we analyze the breakup in laminar flow condition, i.e., axisymmetric elongational flow generated in an orifice where the rate of strain increases monotonically towards the orifice. Because of the steady nature of the flow, we measure the flow field separately and analyze the aggregate breakup based on the averaged flow field using an Eulerian grid with a spacing of $\Delta = 0.5mm$. The domain symmetry provides a useful means to determine the accuracy of the measured velocity field. The accuracy is sufficient to take spatial derivatives and thus to obtain the complete field of velocity gradients, $\frac{\partial u_i}{\partial x_j}$. Before the orifice entrance, the intermediate eigen vector λ_2 together with the equally strong λ_3 of the rate of strain tensor $s_{ij} = \frac{1}{2} \left(\frac{\partial u_i}{\partial x_j} + \frac{\partial u_j}{\partial x_i} \right)$ play an effective role by compressing the aggregates with the stretching exerted by λ_1 , whereas the most extensional eigen vector λ_1 and the ratio of the intermediate to the most compressive eigen value, i.e., $|\frac{\lambda_2}{\lambda_3}| \rightarrow 0$ past the orifice acts as a demarcation for the transition from elongation to simple shear. We found most of the breakage taking place within $\sim 2-3$ mm on either side of the contraction where s^2 reaches its maximum value.

In the second part of the experiment, we analyze breakup in fully turbulent flow. To study the structure of the homogeneous quasi isotropic turbulence at a Taylor based Reynolds number $Re_\lambda = 90$ around the aggregate we compute the coarse grained velocity derivative, $\frac{\partial \tilde{u}_i}{\partial x_j}$ which exhibits roughly the same characteristic properties like their small scale counterpart. Probably one of the most important properties we have observed is $\langle \Lambda_2 \rangle > 0$ which indicates that $\frac{\partial \tilde{u}_i}{\partial x_j}$ also feels self amplification at our scale of

measurement, which is just at the upper end of the viscous scale. More generally, the effect of the small scale dynamics on the aggregates can be reflected appropriately through the measured coarse grained velocity derivative. We measure the coarse grained strain \tilde{s}^2 and enstrophy $\tilde{\omega}^2$ along the Lagrangian trajectories of the aggregate which are on an average $\sim 10\tau_\eta$ long where τ_η is the Kolmogorov time scale of the flow. That means we are capable of looking into the history of the instantaneous flow dynamics in the proximity of the aggregates as long as $10\tau_\eta$ which is supposed to be sufficient for understanding the Lagrangian influence on breakup because the characteristic time scale of vorticity and strain is of order $\mathcal{O}(\tau_\eta)$. While s^2 is the key agent for the structural deformation, ω^2 governs the rotation of the aggregates along its trajectory. Hence in the region of high ω^2 an aggregate is expected to experience less deformation but to tumble whereas in s^2 dominated regions of the flow an aggregate is subject to larger deformation. Besides studying how the strain \tilde{s}^2 and enstrophy $\tilde{\omega}^2$ evolve over time along the aggregate trajectory, we also study the role of the competing mechanism of \tilde{s}^2 and $\tilde{\omega}^2$ on the breakup. Therefore, we examine the orientation of the aggregate with respect to the eigen frame of the rate of strain tensor, i.e., λ_i 's. That sheds light on how the aggregate responds to the rapid evolution of the strain eigen frame that continuously exerts stretching and compression. We measure the separation vector \mathbf{r} , a vector between the fragments at the time of breakage. It is interesting to observe how consistently \mathbf{r} aligns itself with λ_1 , the most extensional eigen vector along its Lagrangian trajectory. For inconsistent alignment, this will also show how frequently ω^2 interferes with s^2 to deflect the aggregate from λ_i 's. To address the situations where an aggregate might sustain higher s^2 but undergoes fragmentation at somewhat lower s^2 , we investigate if strain is directionally biased towards the separation direction between the fragments. If we assume the plane across which an aggregate breaks apart is the weakest plane, i.e., mechanical anisotropy is more pronounced there than anywhere inside the aggregate, then before the breakage, stretching along \mathbf{r} should exhibit a smaller value than the one at breakage. In principle, we want to explore if there exists a critical behavior between the strain and the direction along which breakup occurs. This is informative to understand, at least on a qualitative level, the effect of s_{ij} on the aggregate's mechanical property. Finally, to study the cumulative effect of $\frac{\partial \tilde{u}}{\partial x_j}$ on the aggregate, we use the Cauchy-Green deformation tensor \mathbb{W} . The aggregates are soft matter and fractal in morphology. Therefore they are susceptible to deform considerably over a certain time scale and that is why the pointwise measure of s^2 or ω^2 might prove inadequate to explain the underlying breakup mechanics simply due to the reason that the instantaneous estimate does not acknowledge the preceding history. If the aggregates experience finite deformation over a finite length of time and thereafter fail to sustain their unbroken state then we stress on the importance to investigate critical deformation and the time that yields that state. The ratio of the intermediate eigen value of \mathbb{W} to the most extensional one allows to estimate the "shape" of the deformed aggregate and consequently the dominant role between the two. We found that, indeed the direction along which breakage takes place is the most stretching direction of the Cauchy-Green eigen vector. That means an aggregate breaks into two parts in the direction along which it experiences the maximum integrated stretching. The appropriate time scale for which we found this result most pronounced is about twice the Batchelor time scale which is equivalent to four Kolmogorov time scales in our experiment.

Zusammenfassung

In dieser Doktorarbeit wurde das Brechverhalten von fraktalen, kolloiden Polymer-Aggregaten experimentell mittels drei-dimensionaler Particle Tracking Velocimetry (3D-PTV) unter laminaren sowie turbulenten Strömungsbedingungen untersucht. Die Zielsetzung war ein tieferes Verständnis der Brechmechanismen in einem Lagrange'schen Bezugssystem, das Zugang zum zeitlichen Ablauf der Strömungsdynamik in der direkten Umgebung und entlang der Bahnlinien von Aggregaten ermöglicht. Dies brachte neue Einblicke in die Eigenschaften von Brechmechanismen und deren Schlüsselparameter. Unser bisheriges Verständnis von Brechverhalten von kolloiden Aggregaten stützte sich vor allem auf experimentell und numerisch erfasste mittlere Grössenverteilungen und damit verbundene Bruchkriterien. Letztere basieren im Wesentlichen auf unmittelbar wirkende Kräfte und lassen ihre zeitliche Entwicklung und kumulierten Effekt ausser Acht. Hier setzt unsere Kernfrage an, die lautet: was ist der Lagrange'sche Beitrag des Strömungsfeldes, welchem ein Aggregat für eine bestimmte Zeit ausgesetzt ist bevor es letztendlich bricht?

Unsere Vorhaben, das Brechverhalten zu untersuchen ist auf diese Frage ausgerichtet und basiert auf folgenden Eckpunkten. In erster Linie wurde die Fähigkeit der Messmethode 3D-PTV, den vollen Geschwindigkeitsgradienten Tensor entlang der Bahnkurven von Aggregaten während des Brechens ermitteln zu können, ausgeschöpft. Das heisst, es konnten Informationen darüber ermittelt werden, wie Aggregate über ihrer Lebenszeit durch Geschwindigkeitsgradienten beeinflusst werden, was direkte Auskunft über Bruchmechanismen gab. Aggregate finiter Grösse wurden einzeln in die Strömung eingebracht, sodass die Strömung selbst nicht durch die Aggregate beeinflusst wurde, und damit nur jeweils ein Brechereignis stattfinden konnte, was die Detektion vereinfachte. Als erstes wurde das Brechverhalten unter laminaren Bedingungen, und zwar unter einer achsensymmetrischen Dehnströmung untersucht. Diese wurde durch einen Fluss durch eine kleine Mündung realisiert, gegen welche die Dehnung monoton zunimmt. Wegen der stationären Natur der Strömung wurden Brechverhalten und Geschwindigkeitsmessungen separat untersucht und nicht simultan erfasst. Die Symmetrie der Strömung ermöglicht eine Abschätzung der Messgenauigkeit, die ausreichte, um den Geschwindigkeitsgradienten Tensor $\frac{\partial u_i}{\partial x_j}$ zu berechnen. Vor der Mündung spielt der zweite Eigenvektor λ_2 des Dehnungstensors $s_{ij} = \frac{\partial u_i}{\partial x_j} + \frac{\partial u_j}{\partial x_i}$ zusammen mit dem gleichstarken dritten Eigenvektor λ_3 eine effektive Rolle, indem sie eine Kompression ausüben, während λ_1 für starke Dehnung verantwortlich ist. Das Verhältnis der Eigenwerte des Dehntensors $|\frac{\lambda_2}{\lambda_3}| \rightarrow 0$ nach der Mündung markiert den Übergang von der Dehn- zu einer Scherströmung. Die Messungen ergaben, dass die meisten Brüche an einem Abstand von etwa 2-3 mm vor und nach der Mündung auftraten, wo s_{ij}^2 maximal war.

Im zweiten Experiment wurde das Brechen von Aggregaten in einer voll entwickelten turbulenten Strömung untersucht. Um die Struktur der homogenen, quasi isotropen Turbulenz mit einer Taylor Reynoldszahl von $Re_\lambda = 90$ zu erfassen, wurde der gefilterte Geschwindigkeitsgradienten Tensor $\frac{\partial \tilde{u}_i}{\partial x_j}$ gemessen, welcher

im Wesentlichen dieselben Eigenschaften seines fein-skalierten Gegenübers erfüllt. Möglicherweise die wichtigste Eigenschaft, die beobachtet wurde war $\Lambda_2 > 0$, welche besagt, dass $\frac{\partial u_i}{\partial x_j}$ Selbstverstärkung auf unserer Messskala, welche am oberen Ende des viskosen Bereichs liegt, spürt. Im Allgemeinen konnte der Effekt von fein-skalierten Dynamik auf Aggregaten angemessen durch den gefilterten Geschwindigkeitsgradienten Tensors wiedergegeben werden. Die gefilterte Dehnung s_{ij}^2 und Wirbelstärke ω^2 wurde entlang Aggregatsbahnen gemessen, die im Mittel etwa $10\tau_\eta$ lang waren, wo τ_η die Kolmogorov Zeit der Strömung ist. Das heisst, die instantane Strömungsdynamik konnte über eine Zeitspanne von $10\tau_\eta$ bevor dem Brechen ermittelt werden. Diese Zeitspanne ist ausreichend um den Lagrange'schen Einfluss auf das Brechverhalten zu untersuchen, da die charakteristische Zeitskala von Dehnung und Wirbelstärke $\mathcal{O}(\tau_\eta)$ ist. Während s_{ij}^2 strukturelle Deformation verursacht, ist ω^2 verantwortlich für die Rotation von Aggregaten entlang ihrer Bahnkurven. In Regionen, wo ω^2 dominant ist, rotiert ein Aggregat stark und wird nur schwach deformiert, während in Regionen, wo s_{ij}^2 dominiert, das Gegenteil der Fall ist. Neben der Studie von s_{ij}^2 und ω^2 entlang Partikelbahnen, wurde auch die konkurrierende Rolle von s_{ij}^2 und ω^2 für das Brechverhalten untersucht, das sich in der Ausrichtung zwischen Aggregat und den Eigenvektoren des Dehntensors manifestiert. Dies brachte Einblicke wie ein Aggregat auf die schnelle Dynamik des Dehntensors und abwechselnde Kompression und Dehnung reagiert. Der Abstandsvektor zwischen den Fragmenten zeigte eine präferentielle Ausrichtung mit dem Dehneigenvektor λ_1 entlang ihrer Bahnkurven. Bei schwacher Ausrichtung kann ein Einfluss von ω^2 festgestellt werden, der Aggregate von einer bestimmten Ausgangskonfiguration wegdreht. Um Situationen zu verstehen, in denen ein Aggregat starke Dehnung überlebt, um dann an einem späteren Zeitpunkt bei relativ schwacher Dehnung zu brechen, wurde die Dehnung entlang \mathbf{r} untersucht. Unter der Annahme, dass die Ebene entlang der ein Aggregat bricht, die mechanisch schwächste Ebene sei, d.h. die mechanische Anisotropie ist am stärksten entlang dieser Ebene, sollte die Dehnung entlang \mathbf{r} bevor dem Brechen kleiner sein, als zum Brechzeitpunkt selbst. Das heisst, die Dehnkomponente entlang \mathbf{r} sollte ein kritisches Verhalten zeigen und gleichzeitig Aufschluss auf die mechanische Anisotropie der Aggregate geben. Letztlich wurde der Cauchy-Green Tensor \mathbb{W} berechnet, um den kumulativen Effekt von $\frac{\partial u_i}{\partial x_j}$ zu erfassen. Aggregate sind aus flexiblem Material und haben eine fraktale Form, deshalb können sie über eine bestimmte Zeit erheblich deformiert werden. Das heisst auch, dass das momentane s_{ij}^2 und ω^2 wohl nicht ausreichend sind, um Brechmechanismen vollständig zu erklären, da der zeitliche Ablauf eine wichtige Rolle spielt. Wenn ein Aggregat eine endliche Deformierung über eine bestimmte Zeitdauer erfährt, und folglich dem Brechen nicht standhalten kann, weist das auf die Wichtigkeit von kritischer Deformierung sowie der Zeitdauer, um diese zu erreichen, hin. Das Verhältnis zwischen mittlerem und grösstem Eigenwert von \mathbb{W} erlaubt Rückschlüsse auf die Form der Deformierung des Aggregats. Es hat sich herausgestellt, dass die Brechrichtung mit dem Eigenvektor des grössten Eigenwertes von \mathbb{W} ausgerichtet ist. Das heisst, ein Aggregat bricht in zwei Teile in der Richtung entlang der es die grösste integrierte Dehnung erfährt. Die passende Zeitskala, für die dieses Resultat am ausgeprägtesten war, ist etwa zwei Batchelor Zeiten, was ungefähr vier Kolmogorov Zeiten in unserer Strömung entspricht.

Contents

Abstract	i
Zusammenfassung	ii
1 Introduction	1
1.1 Literature background of the previous work	2
1.2 Framing the present work	4
2 Materials and methods	7
2.1 Orifice: Extensional flow	8
2.2 Turbulent box: Homogeneous Isotropic Turbulence	9
2.3 Aggregates	10
2.4 3D-PTV	12
2.4.1 Optical arrangement	14
2.4.2 Illumination	16
2.4.3 Calibration	16
2.5 Breakage detection	17
2.5.1 Breakage detection in orifice	18
2.5.2 Breakage detection in turbulent flow	20
2.6 Ellipse fitting	20
2.7 Aggregate in turbulence	25
3 Results	31
3.1 Flow field analysis: Orifice	32
3.2 Breakage analysis in orifice	40
3.2.1 Example analysis	40
3.2.2 Statistical analysis	43
3.3 Concluding remark: Breakup in orifice	49

3.4	Flow field analysis : Homogeneous quasi isotropic turbulence	49
3.5	Breakage analysis in turbulence	57
3.5.1	Example analysis	57
3.5.2	Statistical analysis	59
3.5.3	Alignments with the principal strain and deformation	64
3.5.4	Integrated deformation analysis	66
3.6	Concluding remark: Breakup in homogeneous quasi isotropic turbulence	72
4	Conclusion	73
	Bibliography	74

List of Figures

2.1	Orifice setup made of plexiglass	8
2.2	Setup made of PVC.	9
2.3	A laboratory view of the experimental setup	10
2.4	A schematic view showing the disks connected with gears	11
2.5	Aggregates grown in quiescent flow	12
2.6	Projection of epipolar lines from different cameras	13
2.7	Correspondence and tracking phase of 3D-PTV	14
2.9	Optical setup using four mirrors and an image splitter	16
2.10	Calibration target inside the orifice	17
2.11	Change in total pixel number when an aggregate is broken into two parts	18
2.12	An arbitrary breakage event seen from a single camera	21
2.13	Change in grey value over time is a measure of the segmentation	22
2.14	Ellipse fitting for different aggregate shapes.	22
2.15	Overestimated approximation of the aggregate area	23
2.16	Accurate approximation of the aggregate shape	23
2.17	A set of ellipses are drawn using different number of boundary pixel coordinate	24
2.18	Comparison of an aggregate shape by one ellipse and two ellipse	24
3.1	Flow trajectories in the orifice	32
3.2	Pdf of the trajectory length	33
3.3	Velocity vectors in the orifice	33
3.4	Velocity magnitude close to the wall and along the centerline of the orifice	34
3.5	Flow trajectories showing the time to reach the orifice	34
3.6	Ensemble average of the velocity as a function of time and along the downstream in orifice	35
3.7	Strain iso surface in the orifice	36
3.8	Eigen vectors of the rate of strain tensor in the orifice	38
3.9	Orientation of λ_1 and λ_3 along the downstream in the orifice and the pdf of Λ_i 's	39

3.10 Iso surface of the Λ_i 's in the orifice	39
3.11 Examples of the aggregates bigger than the channel width	40
3.12 Aggregate breakage along the channel	41
3.13 An aggregates breaks into two parts	41
3.14 An aggregates breaks into four parts	41
3.15 Trajectories of the parent and the children from two arbitrary breakage events	42
3.16 s^2 along the trajectories from two arbitrary breakage events	42
3.17 Breakage locations in the orifice labeled with strain rate (isometric view)	43
3.18 Breakage locations in the orifice labeled with strain rate (planar view)	44
3.19 Pdf of the breakage locations and s^2 at breakage in the orifice experiment	44
3.20 Breakage locations in the orifice labeled with $ \Lambda_2/\Lambda_3 $ (isometric view) in the orifice	45
3.21 Breakage locations in the orifice labeled with $ \Lambda_2/\Lambda_3 $ (planar view) in the orifice	45
3.22 Aggregate's initial size as a function of s^2 at breakage labeled with $ \Lambda_2/\Lambda_3 $ in the orifice	46
3.23 $ \Lambda_2/\Lambda_3 $ at breakage along the downstream in the orifice experiment	46
3.24 Evidence of the power law scaling comparing with the results from SALS	48
3.25 Trajectories in homogeneous quasi isotropic turbulence	50
3.26 Pdf of the trajectories in turbulent flow	51
3.27 Quality check of the measurements in turbulent flow	52
3.28 The joint pdf of each component of the kinematic relation $\frac{\partial u_i}{\partial x_i} = \frac{\partial u_j}{\partial x_j} + \frac{\partial u_k}{\partial x_k}$	53
3.29 The joint pdf of each component of the kinematic relation $\frac{\partial u_i}{\partial t} = \frac{\partial u_i}{\partial t} + u_j \frac{\partial u_i}{\partial x_j}$	53
3.30 R-Q plot	54
3.31 Pdf of $\cos(\omega, W)$ and $ \frac{\Lambda_2}{\Lambda_1} $ in turbulent flow	54
3.32 Eulerian second order longitudinal velocity structure function $S_2(r)$	55
3.33 Pdf of the instantaneous velocity component	55
3.34 Trajectories from a breakage event as seen from four camera	58
3.35 An arbitrary breakage event in turbulent flow	58
3.36 Elastic deformation of the aggregate is seen in turbulent flow	59
3.37 s^2 and ω^2 over time along a breaking trajectory	60
3.38 A breaking trajectory labeled with s^2 and ω^2	60
3.39 Λ_1 and $ \frac{\Lambda_1}{\Lambda_3} $ along the breaking trajectory	61
3.40 A set of breakage events taking place at $s_b^2 \rightarrow s_{max,g}^2$ or $s_{max,\ell}^2$	61
3.41 Breakage events where s^2 and ω^2 at breakage differs by a large margin	62
3.42 Breakage events where s^2 and ω^2 tends to equate each other	62
3.43 Aggregates survive the global maxima of s^2 and ω^2	63

3.44 Breakup events taking place at the pick of s^2	63
3.45 Orientation of the aggregate with the strain eigen frame	64
3.46 Mutual orientation of λ_1 and λ_2 with aggregate trajectory	65
3.47 The most compressive eigen vector of s_{ij} along the parent and children trajectory.	66
3.48 Pdf of the alignment between the separation vector and λ_i 's	66
3.49 With respect to \mathbf{r} orientation of the aggregate with λ_i	67
3.50 Integrated deformation of an aggregate	68
3.51 Pdf of $\cos(W_{1,3}, \mathbf{r})$ where Cauchy-Green deformation tensor is integrated over different τ_B	69
3.52 Orientation of \mathbf{r} relative to \mathbb{W} over $2\tau_B$	70
3.53 Pdf of the alignment between \mathbf{r} and Cauchy-Green eigen vector	70
3.54 Joint pdf of Λ_1 and Λ_2 and $\ln w_1$ and $\ln w_2$	71
3.55 Aggregate size as a function of the critical strain in turbulent flow	71

List of Tables

3.1 Flow properties of the turbulent flow	56
---	----

Chapter 1

Introduction

Aggregates are constellations of tiny particles. They are subject to breaking into fragments in turbulent and non-turbulent flows. The objective of this thesis is to experimentally investigate the breakup mechanism of aggregates. Indeed, an aggregate breaks at a certain time and space in a flow but when the mechanism comes into the question, i.e., how and why an aggregate breaks, one needs to carefully study the history of the forces that a colloid is exposed to until it disintegrates. This is where the motivation of the thesis sets in. We want to capture the underlying physics of the breakup in the Lagrangian frame work i.e., using a reference system that moves with the particle for which we realize the first ever experimental effort of its kind. We will use three dimensional particle tracking velocimetry (3D-PTV), a whole field non intrusive flow diagnostic technique based on image acquisition, as the working tool. The novelty of this experimental work is to exploit the proven ability of 3D-PTV to simultaneously measure the flow field and track the aggregate itself. It gives access to the properties of the fluid phase, i.e., the full tensor of the velocity gradient in the close proximity of the aggregate before, during and after the breakage. In plain words, the field of strain applies the force on the aggregate and vorticity determines the orientation of the aggregate relative to this force. Since 3D-PTV can disclose the entire history of the interactive dynamics of strain and vorticity along the aggregate trajectory it will allow us to substantiate the present understanding of breakup providing broader insight through the Lagrangian effect on breakage kinetics.

1.1 Literature background of the previous work

Suspensions of aggregates are quite prevalent in industrial and environmental flows. Aggregates and their interaction with the carrier fluid play an integral role in a number of chemical processes such as crystallization, separation processes and reaction in multiphase systems [21, 60, 104]. For the dense colloidal systems, suspension properties like rheology, conductivity and opacity are determined by the evolution of the size of the aggregates and the internal structure during operations like polymer manufacturing, pharmaceutical industry, food processing and many others [12, 37, 20, 117, 121]. Further, colloid aggregation and breakage is also involved in environmental flows. Marine colloids have received increased attention because of their significance in biogeochemical cycling of organic matter as well as the fate and transport of the elements of marine chemistry which in turn influence the carbon budget in the ocean [93, 63, 106, 88, 131]. Aerosols are also colloids and they are playing a key role in climate dynamics [1, 61]. The most recent medical application of aggregate breakage shows the promise to bust the blood clot obstructing critical blood vessel because of thrombosis by means of nano particles coated with drugs [94]. Due to this broad spectrum of application, significant efforts have been invested to understand aggregation and breakage dynamics.

Since Smoluchowski [110, 111] put forward the dynamics of aggregation, the mechanism of floc growth in solutions has been studied in significant detail and clarified fairly well, both in modeling [135, 64, 65, 66, 105, 136] and experiments [33, 62]. In parallel, theoretical interpretation developed so far confirms the experimental outcome [33, 62, 8, 7, 116]. On the other hand breakup mechanism of coagulated particles, especially large aggregates of arbitrary shape remains poorly understood up to now [2, 137, 48].

The number of bonds and cohesive force of the bonds between the constituent particles determines the aggregate strength [120, 76, 58, 112]. The bond strength is a function of the material and surface properties of the primary particle and chemical properties of the flocculant while the number of bonds inside an aggregate depends on the structure of the aggregates itself. There exists no direct way to measure the strength of the aggregate because of the structural heterogeneity, diverse physicochemical properties of the aggregate, wide range of aggregation mechanisms and lack of quantification of the relevant flow properties in a realistic flow environment that drives the breakage kinetics. The most common approach to examine the strength of an aggregate is to break it under a particular flow condition and analyze the produced fragments.

In a flow, an aggregate experiences both fluid-particle and inter-particle interactions. An equilibrium among all the interactions determines if an aggregate will be broken or restructured, i.e., spatial rearrangement of primary particles within the cluster occurs [36]. Breakage is believed to occur at a cost of local hydrodynamic stress transcending the bond energy associated with the aggregate, i.e., aggregate strength [28, 112, 132, 100, 95, 119, 128]. Van de Van and Hunter [126] pointed out the crucial factors involved in the breakup process. Depending on the variation in severity of the event, breakup is classified into two distinct modes [97, 99]. Gradual dispersion of tiny fragments from the surface of the parent aggregate is referred to as *erosion* [55, 109, 41] and large scale disintegration or breakage into fragments of comparable sizes is recognized as *fragmentation* [40, 68, 125]. In principal, tangential shear and tensile stress exerted on the radial and axial direction of the aggregate mass, respectively, are responsible for generating these two breakage modes [122, 90]. The rate of energy dissipation and relevant time scales of the flow are also qualitatively reflected through these modes. Lower energy input causes erosion between cohesionless or weakly cohesive primary particles [102] while higher energy input triggers fracture along the plane transecting through the center of aggregate mass [11]. These two

modes also show different time scales. Fragmentation is abrupt and hence needs a shorter time scale, i.e., it is discontinuous in time leading to a step reduction in initial mass, whereas continuously shearing off the particles from the surface takes place over a longer time scale [97]. Physicochemical properties of the flocculant environment also influence the mode [40]. Vassileva et al. [127] concluded that only large particles are subject to fragmentation which is due to the defects within aggregate structure, in agreement with Yeung et al.'s [134] finding that breakup occurs at the weakest point in the aggregate. The size dependence of breakage is attributed to the fact that a large particle experiences a larger normal force in the center of mass while restructuring in the central part is unlikely. This triggers the breakup by crack growth in the particle body [102]. On the other hand, small particles can undergo restructuring which inhibits crack growth but erosion can take place deep inside the center.

There exists a canonical power law behavior between the the statistical mean of the steady state radius of gyration of the floc and applied stress where the exponent corresponds to the fractal dimension of the aggregate. The fractal dimension is an indicator of inhomogeneous internal structure with density decreasing away from the center of gravity, i.e., structure is somewhat open and tenuous [112, 40, 46, 113, 34, 52]. Zaccone et al. [136] attributed the structural property as characterized by the fractal dimension and the mechanical property given by the elasticity to the power law scaling of the steady-state fragment size with the hydrodynamic stress. The breakage rate also shows a power law scaling with the product of aggregate size and stress, but as opposed to the relation between steady state size of the fragments and stress, it is sensitive to the size of the primary particle [45]. The structure of the final aggregates is reported to be more compact than the structure of the initial ones [101]. The evolution of the morphology of the aggregate is observed only for open structured aggregates independent of the primary particle size. This infers that, breakage and restructuring are coexisting for open aggregates but for dense aggregates only breakage is present. That means that the evolution to the final aggregate morphology is a function of the aggregate's initial structure [46]. According to Glasgow et. al [40] the strength per unit mass decreases with increasing floc size, i.e., the critical shear rate depends weakly on the aggregate's initial size independent of the initial size of the constituent particle and modes of breakup [57, 134, 58, 127].

A systematic investigation revealed different breakup behavior in shear and in elongational flow. Kao and Mason [55] first observed that simple shear and strain have different influences on the breakage of the particles. Photographic observation from Blaser et al. [16] found floc rotation is more pronounced than stretching in simple shear. Constituent particles are discretely and gradually disengaged from the aggregate surface leading to fine particle erosion and insignificant distortion in shape [112]. Shear flow keeps the aggregate rotating and hence the stress on its surface varies with time. As a result it escapes the persistent stretching along the eigen direction of the rate of strain tensor. Rotation is absent in converging flow [15, 50, 112, 49] and flocs undergo a remarkable change in shape from nearly spherical to ellipsoidal. Flocs are aligned and broken along the axis of strain. That is why elongational flow is more efficient to break aggregates than simple shear. In elongational flow, the variation of average radii of gyration with the strain rate is insignificant in contrast to the result from shear flow [112] where there is a variable drag force exerted on the constituent particles at different axial positions as summarized by Higashitani et al. [50]. Flocs of comparable size might have variable vulnerability towards breakup in elongational flow partly because of the fact that streamlines carrying the aggregates might experience slightly different residence time near the stagnation point among other reasons like mechanical stability and structure being different in different flocs.

Experimental results in a Taylor Couette reactor from Serra et al. [108] showed that the final aggregate

diameter in the turbulent regime is independent of monomer size and is instead fully controlled by the Kolmogorov scale as also found by Jankowski et. al [53]. In isotropic turbulence the maximum floc size is a function of dissipation in the viscous subrange [120], hence confirming that the flow dissipation is important for breakage. The fragment mass distribution is also defined by turbulent fluctuations of stress and the fragmentation rate is controlled by the frequency of the critical hydrodynamic stress [5]. Whereas for the laminar flow regime the final diameter of the aggregates exhibits a weak tendency to decrease with increasing diameter of the constituent particle. Marchisio et al. [87] simulated the evolution of colloid size distributions in a Taylor Couette flow to test for different breakage kernels (in the context of numerical simulations, aggregation and breakage models are called as kernels), exponential and power law, with several assumptions on how colloids break apart. Best agreement with experiment is found for power law kernels that assume colloids breaking into parts of comparable size. Discrete element method [48], finite element simulation [13] and Stokesian dynamics [19] are the most prominent and commonly used modeling schemes to analyze aggregate breakup in shear flow. Among other limitations, these models are used to analyze only one kind of interaction in necessary detail, i.e., either hydrodynamic or inter particle while the other is dealt with an empirical approach [30, 13, 14, 44, 49] which in turn could be insufficient for robust interpretation of the breakup mechanism. However, it is strongly felt that better understanding of colloid breakage is necessary for further progress in this field, see, e.g., [87, 86] and [117, 118, 116] among others. It is at this point where an image based technique like 3D-PTV becomes desirable. In particular, one that could simultaneously measure the local strain or shear field while observing breakage events.

1.2 Framing the present work

The vast literature clearly shows the deficit in understanding of the physics underlying the breakup mechanism. There is no probing experimental result that could couple aggregate breakup to the hydrodynamic interaction. The previous experimental works on breakup of aggregates were limited to some prescribed geometry with steady state laminar conditions where the flow field was resolved either analytically or numerically while similar studies in turbulence are missing. Due to the very broad distribution of the velocity gradient and the large variation of the hydrodynamic stress, experimental investigation of breakup in turbulent flow remained challenging and the intricacy of the problem clearly pushed the choice towards the units operating under laminar conditions where a narrower distribution of the hydrodynamic stress exists, e.g., rheometers and four roll mills [16] or contracting nozzles [58, 54]. Technically, experimental methods were not developed sufficiently to offer the required resolution, considering the fact that breakage is a very fast and small scale process [112, 6], allowing the observation of the motion of the particles of small size and simultaneously accessing the details of the turbulent flow field carrying them.

From the work of Blaser, Marchisio and Soos [16, 15, 87, 86, 115, 118] it is clear that image based analysis is necessary to advance understanding of breakage. Moreover implementing high speed cameras enables the detection of individual breakage events. Glasgow and Hsu [40] and Liu and Glasgow [41] applied this method to study the breakup of aggregates in a turbulent jet ($600 > Re_{jet} > 5400$). The common conclusion of mechanisms governing breakage being poorly understood leaves an implication that more factors than “shear” are important and the role of vorticity was found to be crucial [16, 15]. In situations with equal strain, breakage may or may not occur depending on instantaneous vorticity. If strain is balanced by vorticity, i.e. in a shear situation, aggregates remain stable. Only in situations with extensional straining, i.e. in the absence of vorticity, aggregates break apart. In helical flows, i.e. flocs

spinning along their flow path, breakage was strongest, presumably because of more persistent straining, i.e., as an effect of the Lagrangian history. The main message is that intensity of velocity gradients in turbulent flows is influencing the competing mechanisms of colloid aggregation and breakage [41, 2]. An important feature of the field of turbulent velocity gradients is self amplification. This self amplification results in production of strain and vorticity and ultimately it is responsible for dissipation of kinetic energy into heat [124]. Turbulent flow constantly produces small scale gradients [124], causing strong shear of the colloids. This straining field and its cumulative effect on a colloid moving through the shear field are believed to govern colloid breakage. This already indicates the emphasis on hydrodynamic Lagrangian effects on colloid breakage. The critical hydrodynamic stress depends on the colloid orientation with respect to the straining field. This implies that also the flow history of the passive colloid plays a role. From the basic point of view the understanding of colloid breakage is closely related to the field of passive objects such as material lines and surfaces, fluid particles and the evolution of multi-point constellations in turbulent flows. How passive small objects move and orient themselves in a turbulent flow is discussed by, e.g., Girimaji et al. and Guala et al. [39] and [77] among others. If breakage is the final result of a fatigue process then the breakage dependence on the hydrodynamics stresses becomes even more complicated. This leads to difficulties in breakage parameterization for given material properties as a function of colloid scale and turbulence intensity. The objective of this thesis is to relate the colloid breakage mechanism to the dynamics of the local velocity gradient field both in laminar and turbulent flow, i.e., measure simultaneously velocity gradients and breakage with 3D-PTV in axisymmetric straining flow and identify Lagrangian velocity gradient breakage criteria in homogeneous isotropic turbulence. Ultimately we want to measure the local straining and vorticity fields of the fluid phase around a breaking colloid employing a three dimensional particle tracking velocimetry (3D-PTV) system.

Chapter 2

Materials and methods

Experiments on aggregate breakage were carried out for two different flows in two different setups. In the first experiments, breakage was observed in axisymmetric and extensional steady flow, i.e., $\frac{\partial}{\partial t}(\cdot) = 0$ and $\nabla \times \vec{v} = 0$ but $\frac{1}{2}(\frac{\partial u_i}{\partial x_j} + \frac{\partial u_j}{\partial x_i}) \neq 0$. In the second experiment, aggregates were broken in quasi homogeneous isotropic turbulence, $\langle u_1^2 \rangle = \langle u_2^2 \rangle = \langle u_3^2 \rangle$, with zero mean flow. Technically, among others, off the shelf high end optical accessories were used for imaging the flow and colloidal particles as well as detecting the breakage. The method of aggregation of colloidal particles proved to be the most crucial part from the experimental point of view. Because of the intent of the investigation, the aggregates need to be strong enough so that they are broken after leaving a trail of Lagrangian history. Since breakage will be observed directly by identifying individual fragments, aggregates and fragments have to be not too small to be detectable on the images. Furthermore, the flow field where breakage takes place should be resolved appropriately by 3D-PTV, i.e., the spatio-temporal resolution needs to be high enough to resolve velocity gradients. Such a set of a priori requirements proved to be challenging, requiring e.g. the ability to manipulate the strength of the aggregate and thereby the aggregation procedure. This chapter will illustrate in detail the experimental setups, the aggregation method and the data analysis tools used in this thesis.

2.1 Orifice: Extensional flow

The first setup realizes an extensional flow through an orifice. The flow chamber is made of PVC (Poly Vinyl Chloride). Considering transparency for convenient access of an illumination on to the observation domain, the setup was made of plexi glass in the beginning. But the drawback of the material as seen in Fig. 2.1, is the intense reflection upon illumination which outshines the brightness of the aggregate. This clearly hampers an unambiguous visual detection of tracer particles and colloidal aggregates. As every material tends to reflect to a certain degree, the set up was reconstructed from relatively less reflective and opaque PVC. To inhibit the reflection below the level that could upset the detection, the observation domain was painted black.

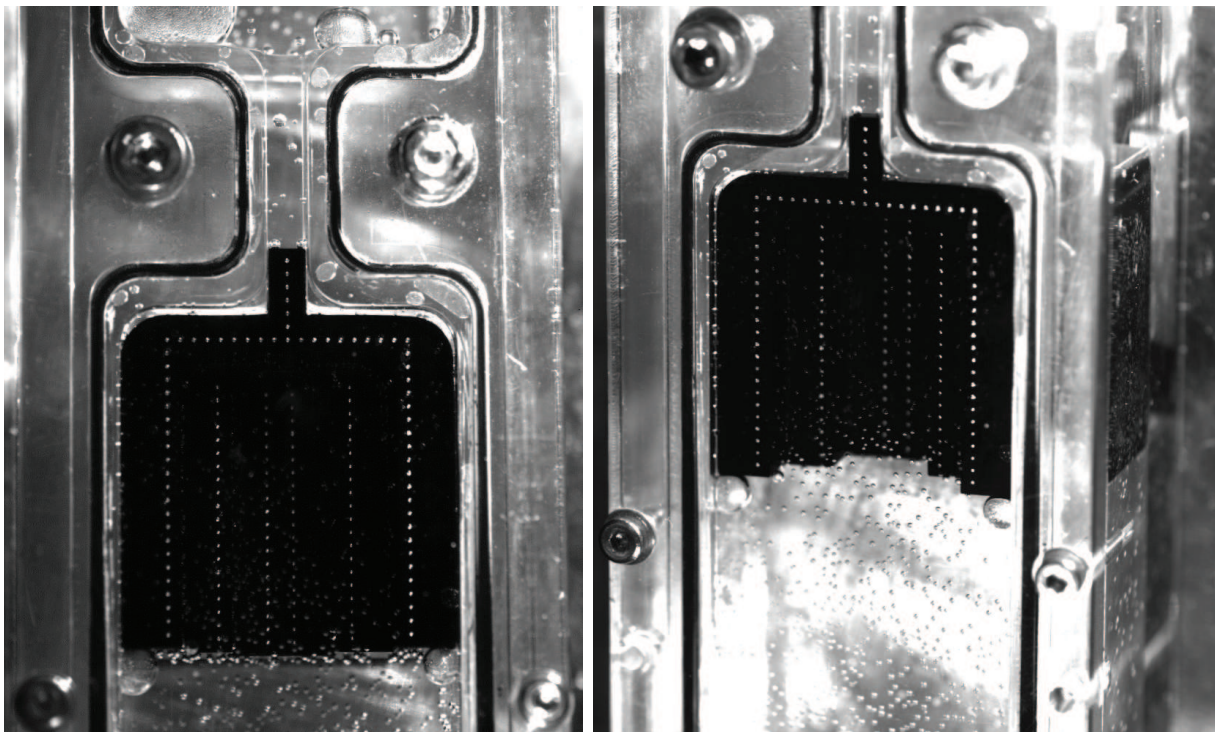


Figure 2.1: Orifice setup made of plexiglass. Under incandescent light the channel (left) and the chamber (right) are undesirably reflective. The photograph shows the flow chamber with a calibration block (black part with dotted pattern) contained in it. The block is removed after calibration and then the flow and breakage measurements are realized.

Geometrically the setup consists of two identical rectangular sinks ($75 \text{ mm} \times 15 \text{ mm}$) on each side of a narrow and shallow channel ($20 \times 3 \times 3 \text{ mm}^3$) as seen in Fig. 2.2. The entire design is imparted to its shape by a mold from a single piece of a PVC block. Soos et al. [113] employed an equivalent setup but much simpler in construction using two modified syringes connecting head on. This abrupt contraction in axisymmetric structure causes a monotonic increment in velocity. There are three inlets in the upstream of the channel. Two transverse inlets are used for the fluid and the inlet at the bottom is used for injecting the aggregates. The entire chamber is sealed with a glass cover closed to the PVC by a series of closely spaced screws. To prevent leakage, a slender elastic thread is inserted into the incised macro canal enclosing the whole chamber. Because of the geometry of the narrow channel, the system required a

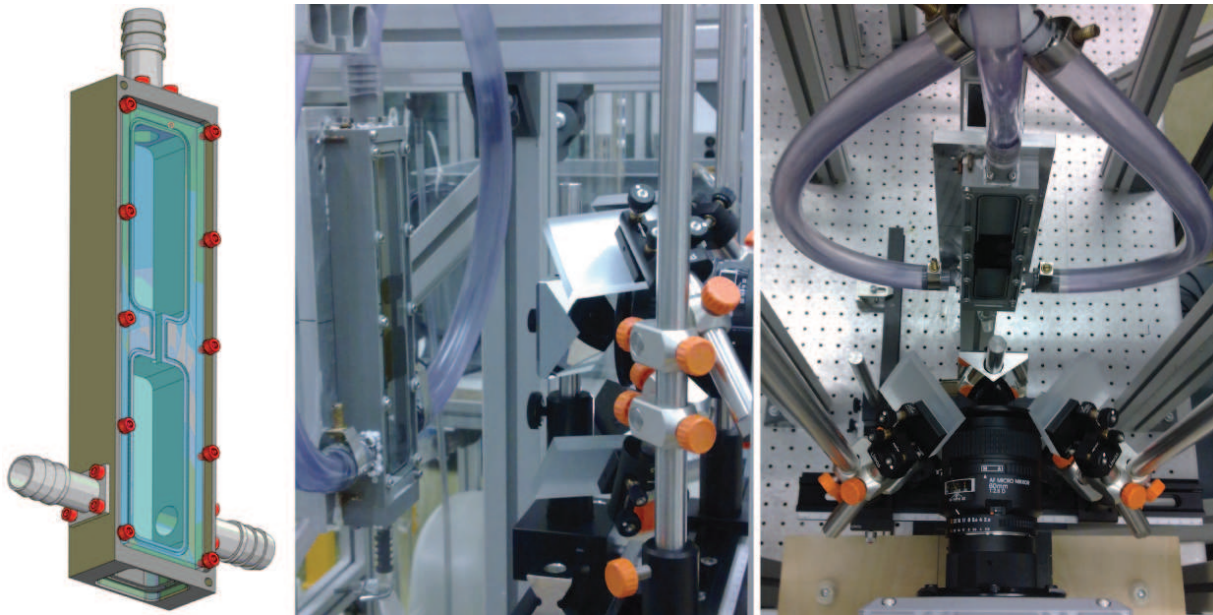


Figure 2.2: Orifice setup made of PVC. Schematic drawing showing the flow chamber (left) and photographs showing a complete assembly with optical system from side (middle) and top view (right).

very steep viewing angle which makes the optical arrangement very congested as seen from Fig. 2.2 (right).

2.2 Turbulent box: Homogeneous Isotropic Turbulence

The second experiment was a quasi homogeneous and isotropic turbulent flow. It was performed inside a glass tank with the dimensions $420 \times 420 \times 440 \text{ mm}^3$ as shown in Fig. 2.3. Turbulent flow was generated by eight counter rotating disks with a diameter of 40 mm. Two sets of four disks, equidistant and square positioned, were braced across 140 mm to the hollow plate containing the gear shaft assembly (see Fig. 2.4). Powered by an AC Servo motor (230V), a maximum angular speed of 4000 rpm can be achieved. In this study, an observation volume of $30 \times 30 \times 40 \text{ mm}^3$ was used to capture breakage. In Fig. 2.4 (left), the location of the observation volume is indicated in between the rotating disks. From Fig. 2.3 it is clear that the only way to illuminate the experimental domain is from the bottom of the glass tank because two sides and the top wall are blocked by the walls of the stirring device and two sides are taken by the optics and the colloidal particle inlet, respectively. Fig. 2.4 (top right) shows the illuminated flow volume seeded with tracer particles. There is a mirror attached to the top wall of the structure to reflect back laser light and enhance the available light intensity. Introducing the aggregates into the flow was a non trivial task. In Fig. 2.4 (bottom right) it can be seen that a PTFE (polytetrafluoroethylene) tube with a diameter of 2 mm is intruding into the domain. This tube carrying the aggregate is delicately placed to the back layer of the illuminated volume in order to avoid reflection coming from the surface of the tube. The aggregates were pushed gently into the turbulent flow by a syringe pump. Multiple aggregates might collide with each other leading to further aggregation or breakage. Therefore, in both experiments aggregate injection was controlled such that a single aggregate appears in the investigation regime at a time. The whole

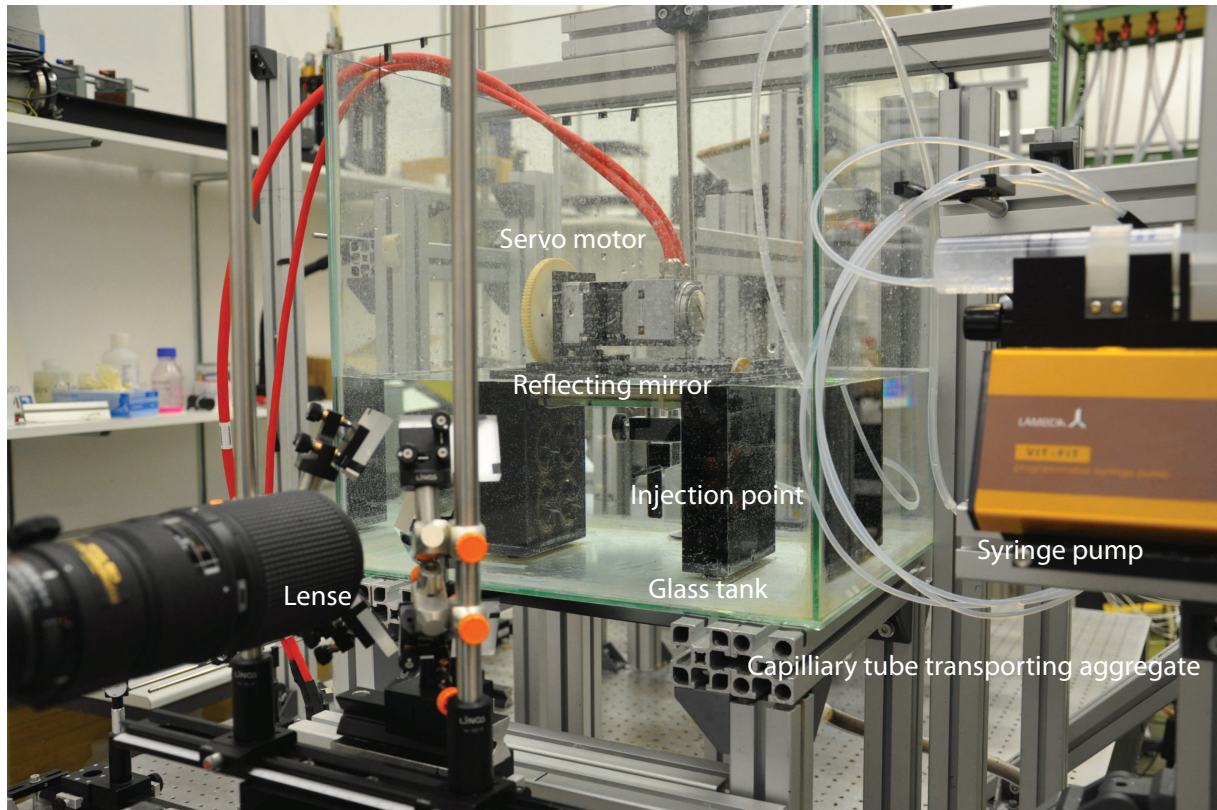


Figure 2.3: A laboratory view of the experimental setup for the breakage of aggregates in turbulence.

process to seize a breakage event is further complicated that aggregates often may not break and be advected out of the observed volume. This uncertainty leads to prohibitively long experimentation time for gathering a large number of breakage events.

2.3 Aggregates

The most challenging part of this experimental work was the preparation of the aggregate. The flow field and the experimental technique dictate the size and strength of the aggregate suitable for the experiment. This potentially limits the degrees of freedom while trying different aggregation methods and using different constituent particles. The essential requirements of the experiment are as follows

- 1) The initial size of the aggregate should be on the order of the smallest length scale of the flow.
- 2) The aggregates should neither be vulnerable nor resilient to the strain field.
- 3) The aggregates should sustain the strain for a few characteristic flow time scales to obtain adequate Lagrangian data to examine the effect of flow history on breakage.

Those constraints leave little window to vary the aggregation methods. For example, perikinetic aggregation where the constituent particles are driven by Brownian motion to form clusters [75] proved to be suitable for straining flow through an orifice although these aggregates are too fragile when put into turbulent flow at moderate Reynolds number, i.e., they are broken almost immediately the moment they

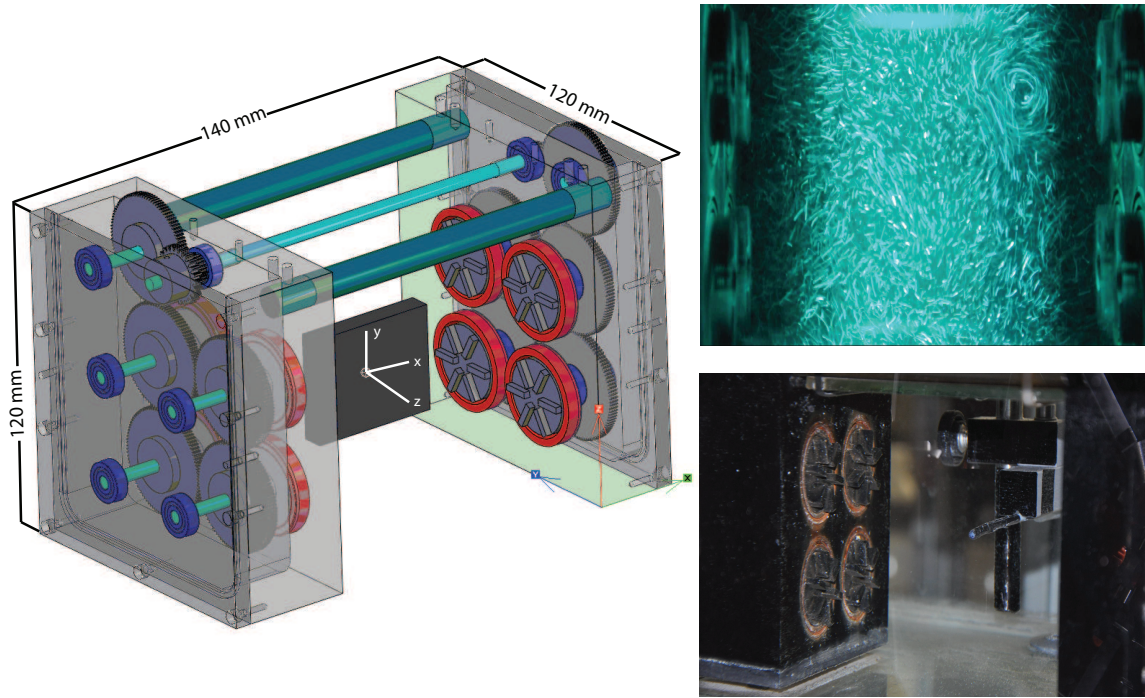


Figure 2.4: A schematic view showing the disks connected with gears and the location of the observation volume (left). On the top right, an illustration of the flow field seeded with tracer particles under laser light is shown. The figure on the bottom right shows the position of the tube carrying the aggregate into the flow field.

are introduced into the flow. On the other hand, aggregates produced by orthokinetic aggregation where flocs are formed from the constituent particles exposed to a velocity gradients are relatively stronger. But in this case the final floc size becomes unfavorably small to be detected by 3D-PTV.

A diffusion limited cluster aggregates (DLCA) are used for the breakage experiment in the orifice setup. These aggregates possess a fractal morphology. The fractal character of the aggregate can be attributed to the fact that the systematic growth of an aggregate is not a function of its size. Fractal aggregates exhibit a scaling behavior between their mass, m and radius, R_G , as $m \propto (R_g/R_p)^{d_f}$ where the radius of gyration of the aggregate, R_g , is normalized by the constituent primary particle radius, R_p , and where the fractal dimension, d_f , appears as an exponent. The fractal dimension is an estimate of the internal architecture of the produced aggregates, i.e., how the primary particles are arranged inside the cluster. A higher fractal dimension is indicative of a compact aggregate whereas a lower fractal dimension is associated with very open aggregates as explained by Ehrl et al. [31] and Lu et al. [71].

Lin et al. [67] reported $d_f \approx 1.8$ when aggregation is carried out in quiescent conditions using fully destabilized primary particles. However, Ehrl et al. [32] and Soos et al. [114] found $d_f \approx 2.7$ when aggregates are prepared under turbulent flow conditions. Aggregates were prepared from surfactant free mono disperse white sulphate polystyrene latex of diameter 420 nm manufactured by Interfacial Dynamics Corp. (IDC), Portland, OR (USA) (Product- No: 1-800, cumulative variation = 2%, batch no: 642, 4, solid% = 8.0 SO_4^{-2} charge and charge density $5.2 \mu\text{C}/\text{cm}^2$). Initially, 0.3 mL of latex solution were diluted in 15 mL deionized water and then destabilized by dissolving in 15 mL of 2.5 molar NaCl.

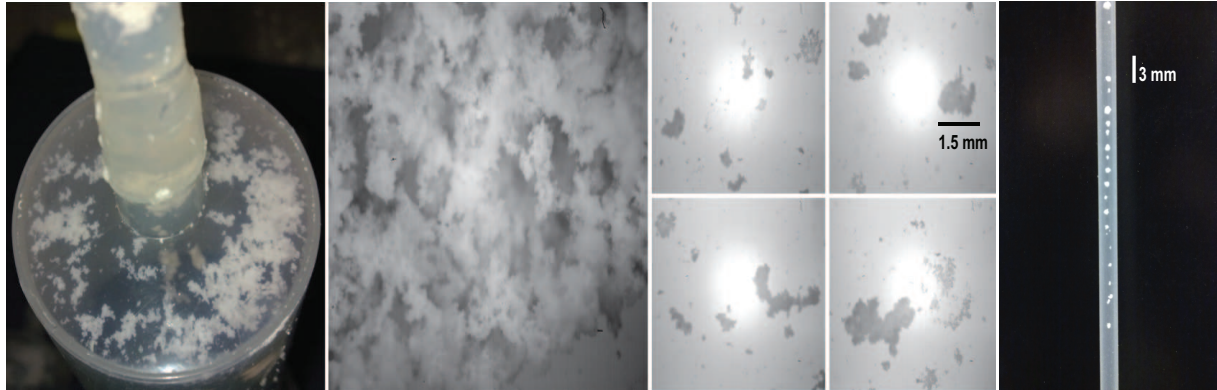


Figure 2.5: Aggregates grown in quiescent flow (left), macroscopic view showing the amorphous structure (middle). Aggregates grown in shear flow condition (right).

The final solid volume fraction of the solution was $10^{-4}(m^3/m^3)$ and its density is $1.05 \text{ kg}/m^3$. Therefore the produced aggregates are expected to be neutrally buoyant in deionized water. Approximately 12 hours were required to grow the aggregates. Floccs appeared as chunks with random shape and size suspended in the solution as seen in Fig. 2.5. A gentle shaking helped to segregate the larger lumps to suitable size, i.e., preferably smaller than the orifice width (3 mm). These floccs were too weak to use in homogeneous turbulent flow as they were observed to pulverize as soon as they were exposed to the turbulent flow. Therefore, for the turbulence, flow induced aggregation was opted for. The solution carrying primary particles are subject to periodic circulation through the tube driven by a syringe pump where the piston moves back and forth at a speed of $2 \text{ mm}/\text{sec}$. Neutrally buoyant tracers (polyamide particles with a mean diameter of $100 \mu\text{m}$, trade name: Vestosint, manufactured by Evonik Industries, Germany) were used for flow characterization.

2.4 3D-PTV

Three dimensional particle tracking velocimetry (3D-PTV) is an image analysis based nonintrusive Lagrangian flow measurement technique. Only a synopsis of the core idea governing the working principle of 3D-PTV and those parameters pertinent to the context of this experimental work will be given in the following description rather than revisiting the rigorous explanation of the technical details by Mass et al. [81, 80, 78, 82] and Malik et al. [84, 85].

The determination of the particle position from image to object space and the linking those positions in time, forms the basic framework of 3D-PTV. On an image, an observed object occupies a patch consisting of a certain number of pixels. Therefore, the particle detection mainly relies on pixel width and grey scale intensity. The particle center is computed as the arithmetic mean of the pixel coordinates weighted by the associated grey values. This particle detection and determination of particle coordinates constitutes the first step of the PTV algorithm. Through a stereoscopic principle and careful calibration of camera positions and orientations, 3D particle positions are computed from 2D images of the particles observed from different viewing directions at a given time instant. Before this can be done, a particle image from a given camera view needs to be associated with the corresponding particle images in the other camera views, the so-called *correspondences* step. The particles used as flow markers do not feature any unique

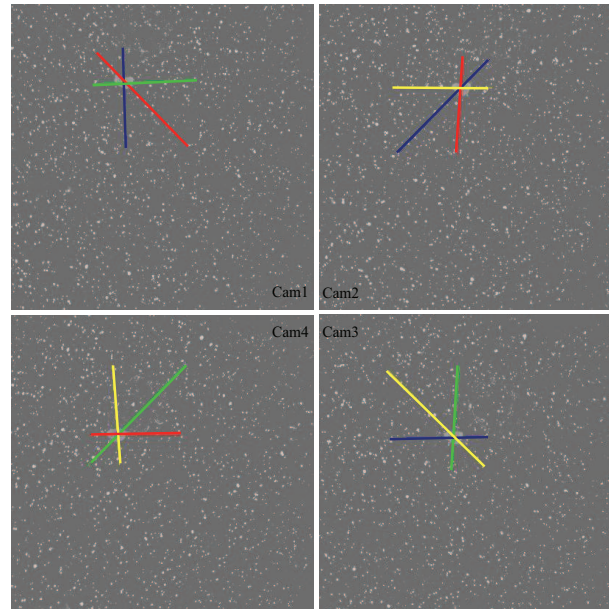


Figure 2.6: The projection of epipolar lines from different cameras intersect to obtain 3D coordinates from 2D images in the so-called *correspondences* step of the PTV algorithm

character by which they can be identified individually by the cameras. Therefore, image coordinates of a stereo pair are used to compute 3-D particle coordinate, i.e., 2D particle coordinates are matched in 3D cartesian space based on epipolar constraints as seen from Fig. 2.6. A particular image point on one camera can be found on the epipolar line of another camera computed by using the orientation parameters of the calibrated system. There could be more than one candidate particle on the epipolar line for the corresponding particle. In order to reduce position ambiguities due to the large number of particles, an empirical tolerance threshold is used to narrow the epipolar search domain and four cameras have been used which reduces ambiguities substantially as compared to a two-camera system [81].

Having 3D positions established, the next step goes on to track corresponding particles through consecutive time steps. This is called the *tracking* phase and builds the candidate Lagrangian trajectories. In the first step, the location of the particle in the next time step is predicted. Based on the assumption that a particle moves with insignificant acceleration, the predicted position from the residence frame to the immediate next frame is a linear function of the velocity, i.e.,

$$x_{f_{n+1}} = x_{f_n} + v_{f_n} \Delta t \quad (2.1)$$

where x_f and x_{f+1} refer to the position in the present and the next frame respectively and Δt is the time interval between the consecutive frames.

A core part of the tracking deals with the demarcation of the search volume centered at this predicted position in order to detect the authentic position of the particle. The maximum radius of the search neighborhood is bounded through an estimate of the maximum flow velocity. Another possibility is to use the velocity decorrelation over δt obtained from Lagrangian structure function in turbulent flow as a measure of the search radius. More precisely, the position to be linked in the future in frame, f_{n+1} , forms a set of trajectories with all the possible positions within the search radius in frame f_{n+2} including the predicted position together with the established links from the current frame, f_n . Using the central

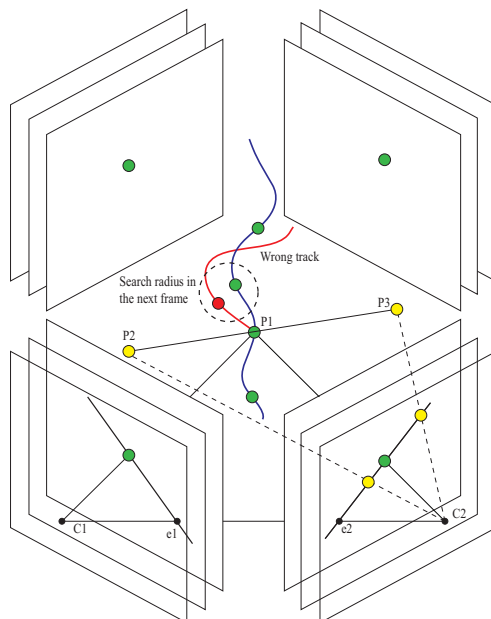


Figure 2.7: Figure showing the correspondence and tracking phase of 3D-PTV. A point, P1, seen by a camera can be found on the epipolar line of the next camera together with other possible points (marked by yellow dots). After the true correspondence of the particle in all four images, this particle is tracked in time based on minimum acceleration criterion.

differences, the acceleration along each possible link is computed as

$$a_{f_n} = \frac{x_{f_n} - 2x_{f_{n+1}} + x_{f_{n+2}}}{2\Delta t^2} \quad (2.2)$$

Among the set of candidate links, the one satisfying the minimum acceleration criterion qualifies for the true link between x_{f_n} and $x_{f_{n+1}}$. Fig. 2.7 briefly illustrates the concept of correspondence and tracking. A rigorous description explaining the conceptual and algorithmic aspects of the tracking procedure can be found in Guezennec et al., Hassan et al., Malik et al. and Papantoniou et al. [43, 47, 84, 85, 98]. Obtained trajectories are post-processed and velocity gradients are obtained by using the methods described by Luethi et al. [74].

2.4.1 Optical arrangement

A stereoscopic observation system has to be arranged with camera views focused on a common observation volume, as shown in Fig. 2.9. The generic setup of a synchronized four camera system can be replaced by a cost effective design introduced by Hoyer et al. [51] that needs a single camera without compromising the robustness provided by four camera stations. In this "image splitter" design a four camera assembly is emulated by a combination of four mirrors and a four face prism placed in front of the camera. Four separate pieces of mirrors are overlaid on to the outer surfaces of the convex part of the image splitter. Hoyer et al. [51] used four separate mirrors glued on the surface of the pyramid to obtain a four face prism. Differently, the image splitter used in this experiment ($50\text{mm} \times 50\text{mm} \times 41\text{mm}$) is made of one piece. The entire pyramid surface is coated with SiO_2 and acts as a single convoluted mirror

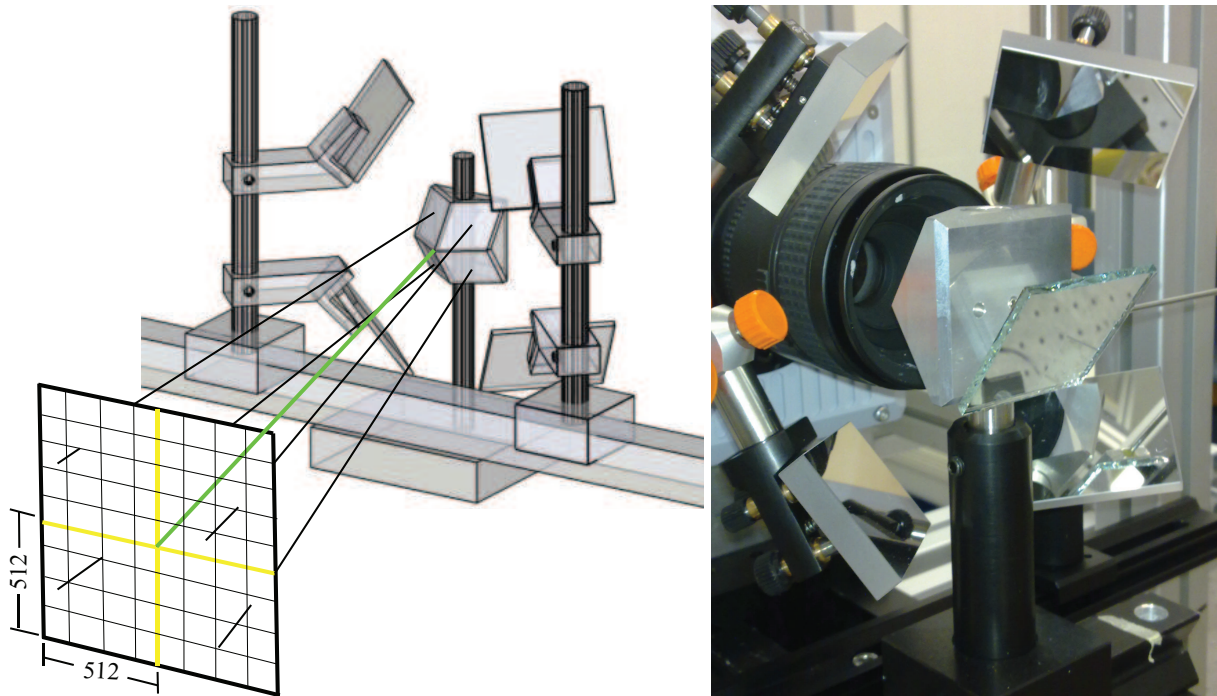


Figure 2.8: Schematic illustrating how an image splitter aligned with the center of the chip (denoted by green line) projects an image reflected by four mirrors onto the camera chip in four different parts and mimic a four camera system. Laboratory view of the optical setup from the back of the image splitter shows the arrangement of the mirror with respect to the position of the image splitter.

facing out in four different directions. Successful imitation of the four camera system needs the tip of the pyramid to be aligned with the mid point of the image chip which in consequence splits the image chip of size 1024×1024 pixel into four equal virtual image chips of 512×512 pixel each. Four mirrors, each 40×58 mm², are installed on the off-the-shelf mounting column, inclined towards the four pyramid surfaces. The connection clamps enable the mirrors to tilt, translate and rotate facilitating independent adjustment of the viewing angle to observe the investigation domain. There are three more tuning screws on the back of the mirror base offering additional three degrees of freedom of movement for fine adjustment. This set of mirrors reflects an observation point on to the pyramid surface. Each surface then projects the same image on a different quarter of the same chip. This is how a combination of mirrors and image splitter emulates the four camera system by utilizing one camera. Fig. 2.8 (left) shows schematically how an image chip is divided into four quarters using the combination of the image splitter and four mirrors and Fig. 2.8 (right) shows the laboratory view of the system. Fig. 2.9 presents a four camera and a single camera system with image splitter. The high speed camera used for this experiment is a FASTCAM SA5 from Photron USA, Inc., which can record up to 7000 frames per second at maximum spatial resolution of 1024×1024 pixel. With 16 GB built-in memory, it is capable of storing 10918 images at the full resolution. In this study a Nikkor Micro 60 mm lens was used with an f -stop 11 and imaging frequency of 4000 Hz for the orifice and 250 Hz for the turbulence experiment.

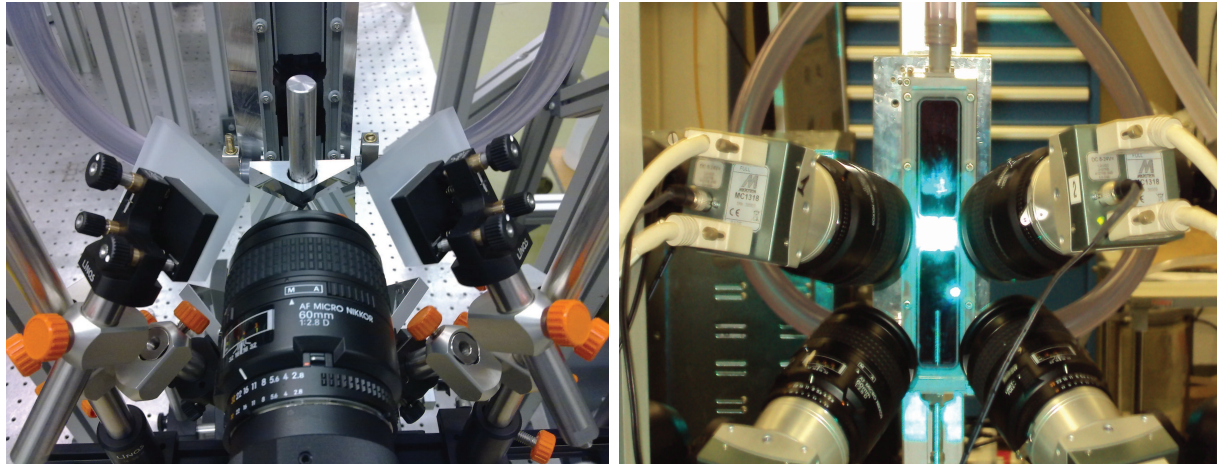


Figure 2.9: Photograph of the high speed camera system and optical setup using four mirrors and an image splitter (left) and the conventional system with four cameras (right).

2.4.2 Illumination

3D-PTV is a volumetric flow visualization technique that requires an illuminated volume. The illumination intensity has to be sufficient for the depth of view within which small tracer particles can be followed reliably. Since the location of a breakage event in turbulent flow is highly probabilistic, it is necessary to use a thick volume in order to visualize the breakage. This requires a strong light source. In this experiment a 20 Watt Ar Ion continuous laser ($\lambda = 513nm$) has been used. The brightness of the particle is also influenced by the spectral response of the CCD sensor of the camera and the optical properties of the particle. The CCD sensor yields the maximum sensitivity in the red color spectrum ($\lambda = 620 - 750nm$) whereas for the Ar-Ion laser ($\lambda = 514nm$), the image sensor responds only up to 70% of the spectral intensity of the Ar Ion laser. The tracer particle scatters light and the scattering intensity varies depending on the stereo angle of the cameras. It is unfeasible to place all the cameras in the same favorable direction from where the particles look most bright. This is the main reason of variable brightness of the same particle on different locations of the same image sensor. In an attempt to resolve this problem to some degree, a mirror is attached perpendicular to the laser path in the turbulent flow setup. Laser light is monochromatic and therefore free of optical dispersion. But the Gaussian distribution of the intensity on either side of the illuminated volume causes the particles near the boundary of the investigation regime to be poorly illuminated. For this reason a few breakage events taking place close to the boundary were discarded as there exists almost no illuminated tracer particle around it to calculate the velocity gradients.

2.4.3 Calibration

The PTV system has to be calibrated for the determination of accurate 3-D particle coordinates. Calibration means determination of the exterior and interior orientation parameters of the camera with respect to the observation domain. Optical aberrations, diffraction, lens distortion, inhomogeneous glass walls disturbing the incidence angle, local temperature gradients affecting the refractive index are the major causes that may deteriorate image quality which potentially leads to the large errors in particle coordinate

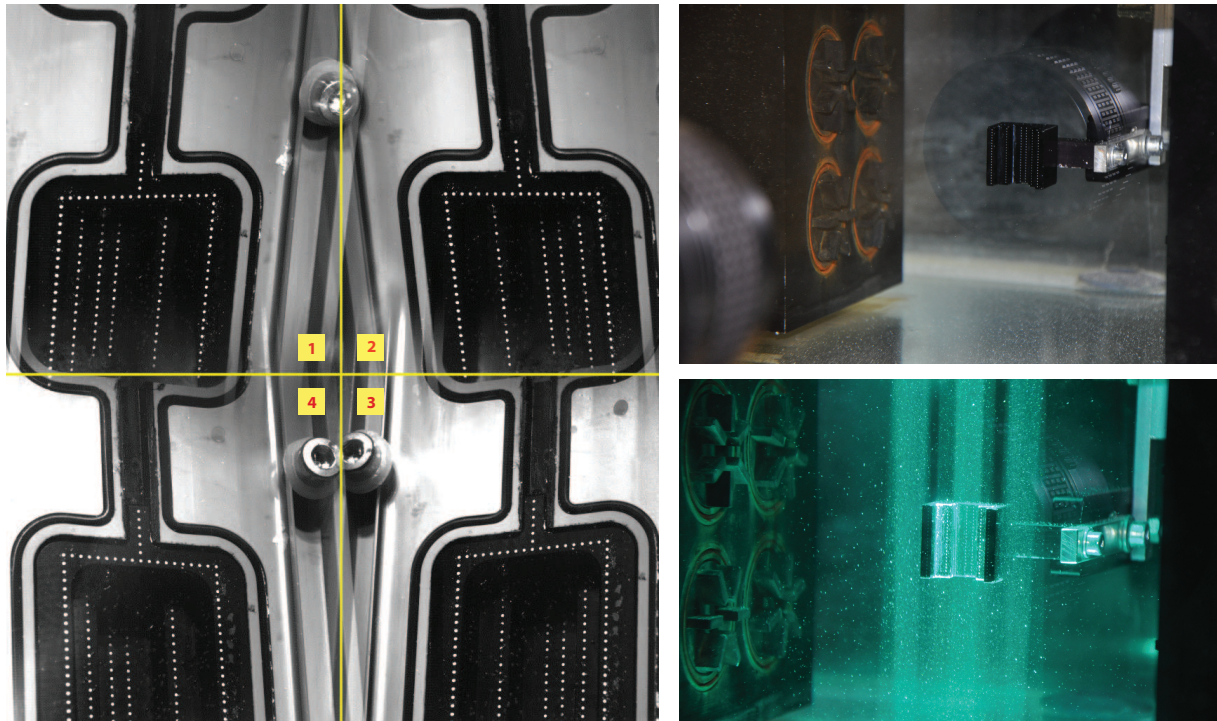


Figure 2.10: Calibration target inside the orifice (left) and within the investigation domain of the turbulent flow setup (right).

determination. The fundamental photogrammetric model based on the laws of perspective projection i.e., object point, camera projective center and image point should lie on a straight line according to the collinearity condition, is revised to take these effects into account (e.g., see Mass et al. [82, 78, 79], Gruen et al. [42], Kotowski et al. [59] and Nishino et al. [96]). As a result, a linearized functional model emerges as the observation equation and is applied to the calibration procedure. The *reference frame* method is used to calibrate the camera system in this experimental work. For this study, a calibration block with uniformly bright target points of diameter $300 \mu\text{m}$ which are set apart by 1 mm from each other and distributed in three equidistant layers was placed into the observation volume and imaged once by all cameras of the system (see Fig. 2.11). Calibration begins with the user's pre-defined arbitrary orientation of the camera and a set of four points on the reference body as an initial input to the model. This invokes the calibration to make a preliminary estimate of the parameters to adjust user supported feed in the beginning.

2.5 Breakage detection

The 3D-PTV software outputs for each particle the number of pixels in x and y directions on the image and the "total" number as well. The number of pixels occupied by the particle is a measure of its size. A reduction in size is indicative of a breakage event and can be used to detect breakage. In addition to the size, 3D-PTV also measures the gray value weighted center of gravity of the particle. The gray value intensity continuously moves away from the center as an aggregate undergoes breakage. Hence discontinuity in gray value intensity can also be used to identify breakup. Due to the difficult viewing

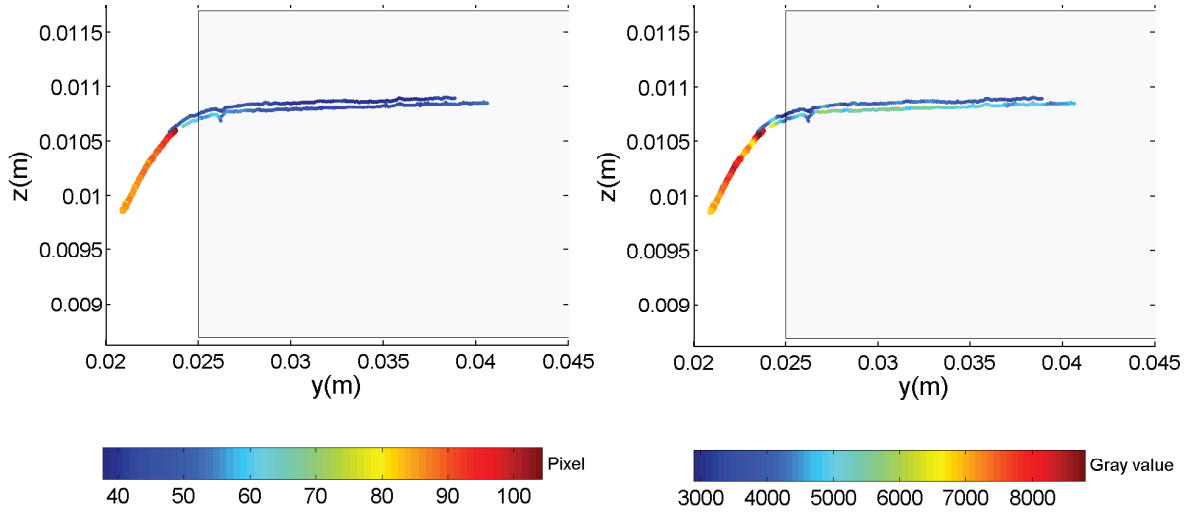


Figure 2.11: Change in total pixel when an aggregate is broken into two parts close to the entrance of the orifice (left). The drop in gray value is another indicator of the same breakage event (right).

angle of the mirrors for the orifice setup, several Lagrangian trajectories of the aggregate appeared interrupted. This results in ambiguous discontinuity in aggregate's gray value more than the size. Therefore, a reduction in size has been used to detect the breakage in orifice. In the turbulent experiment, none of the aggregate trajectories are interrupted. Hence gray value discontinuity was used as the breakage detection parameter.

2.5.1 Breakage detection in orifice

Breakage in axisymmetric converging flow in an orifice is detected in a rigorous way by systematic examination of the reduction of the size (i.e. total number of pixels on the image) of the aggregate along the Lagrangian trajectory. An aggregate subject to break will inevitably be reduced in its size which is measured in the number of pixels of the image patch pertaining to the particle. Hence, segmentation that takes place at one single time can be identified by a large drop in the number of pixels. But the pixel scale in image space can vary depending on the position of the aggregate in object space with respect to the objective center of the lens due to the reasons explained above (inhomogeneous distribution of available light intensity etc.). Therefore an arbitrary sharp drop in pixel value is not necessarily implicative of a size reduction and consequently considered to be breakage. Therefore, a moving time integrated change in the number of pixels number is measured along the parent track to identify the time span where the change of size over a certain time interval is significant which is expressed as

$$\mathcal{P}_i = \int_{t_i}^{t_i + \alpha \Delta t} \partial P(t) \partial t \quad (2.3)$$

The pre-factor α is an integer number that refers to the integration window and ∂P is the change in the number of pixels at a given frame. In this experiment, a change in the number of pixels, $\partial P(t)$, over thirty time steps is integrated along the parent track. To validate the breakage detection, an accuracy potential vector, ξ , is set as

$$\xi = \left[\delta x \quad \delta y \quad \delta z \quad \mathcal{P}' \quad \delta r \quad \Omega \right] \quad (2.4)$$

where δx , δy , and δz denote the rms of the position inaccuracy of the aggregate and \mathcal{P}' is an empirical tolerable deviation in the number of pixels. δr is the spatial tolerance used to capture the probable children tracks associated with the parent track whereas Ω is the non dimensional breakage tolerance that is used to measure the distance between the child and the parent track.

If there exists a drop exceeding the threshold of tolerable deviation in total pixel number, i.e., $\mathcal{P}_i < -\mathcal{P}'$, then it provides the preliminary indication of a breakage event. In this case, the entire Lagrangian trajectory contains both the parent track (up to the breakage point) and thereafter one of the fragment tracks. Local minima of the number of pixels within that particular time interval pin points the time when breakage occurs. On the contrary, if the integral change in the number of pixels along the Lagrangian trajectory of the aggregate stays within the tolerable fluctuation, i.e., $\mathcal{P}_i > -\mathcal{P}'$, then breakage is assumed to occur at the terminal point of the trajectory. The difference between the mean pixel number value before and after the breakage, $\Delta\langle\mathcal{P}\rangle = \langle\mathcal{P}^{parent}\rangle - \langle\mathcal{P}^{fragment}\rangle$, is measured to further validate the trajectory of the aggregate undergoing breakage with an inequality condition such that

$$\Delta\langle\mathcal{P}\rangle > \mathcal{P}'$$

This particular constraint is justified by the fact that considerable size reduction is attributed to the breakage event. For the case where a parent track is long only up to the breakage point, this condition is recalled after identifying the related child track. It is obvious that this condition requires the pixel information from the child track. Detecting the children trajectories can be non trivial especially when there are multiple breakage events, each producing several fragments taking place within a short time interval.

Finding the children trajectory is based on the principle of recursive nearest neighborhood search around the breakage point in time and space. First, within a selected time scale (which is the integration time window of thirty time steps in this experiment) with respect to the time when breakage occurs, all the isolated trajectories are considered and a second order polynomial is fitted for each spatial component as a function of time.

Using those polynomials, the children tracks are projected onto the time of breakage to derive 3D-coordinates of the interpolated neighbors close to the breakage location. The spatial tolerance, δr , defines an isotropic search radius centered at the breakage point and includes the most probable set of starting points of the children track. The minimum spatial offset, normalized by the position inaccuracy δx_i , between the breakage position and the set of close neighbors is then measured with the stipulated threshold for breakage tolerance, Ω , which is a multiple of the square root of the tracking dimension in cartesian coordinates. A children track is found if the minimum offset is smaller than the prescribed breakage tolerance. Fig. 2.11 illustrates the result of the breakage detection algorithm through an example where an aggregate is fragmented into two parts when characterized by the number of pixels. This particular breakage event also exhibits a substantial decrease in grey value along the children track since the smaller children particles scatter less light and appear less bright on the image compared to the parent particle.

2.5.2 Breakage detection in turbulent flow

Breakage detection in homogeneous isotropic turbulence is not based on size, but on the gray value intensity. Every pixel that is a part of an image of the aggregate possesses a certain intensity information. In 3D-PTV the color depth of the recorded image is 8-bit grey scale, i.e., the intensity of a pixel can be represented by a value ranging from 0 (black) to 255 (white). In 3D-PTV, the image coordinates of the particle are determined by the grey value weighted center of gravity as

$$\chi = \frac{\int w_{g,i} x_i}{\int w_{g,i}}$$

where w_g is the corresponding grey value of the pixel coordinate x_i . In principle, a particle is detected when the grey value from all the pixels occupied by that particle are larger than a given threshold set by the user threshold. Although a particle exhibits only one local maximum of gray value, it starts to attenuate radially. An anisotropic threshold operator, \mathcal{G} , makes use of this property to examine the discontinuity of the grey value inside a particle image and if it exceeds an empirical threshold of tolerable discontinuity then the image is assumed to be composed of two separate particles and is splitted into two parts. This criterion to detect breakup of an aggregate has been verified by comparison to visual observation. Fig. 2.12 shows a breakage event (large particle) in a sequence of four time steps overlaid onto one image in homogeneous isotropic turbulent flow seeded with tracer seen as tiny white particles. By measuring the grey value along the Lagrangian trajectory of the parent as a function of time, normalized by the smallest time scale of the flow, i.e., the Kolmogorov time scale, τ_η , this breakage event is detected in time as set to zero on the time axis (see Fig. 2.13). Among the minor fluctuations along the time series of the gray value, there is a large and distinct drop within $\mathcal{O}(\tau_\eta)$ that is below the threshold of tolerable discontinuity and duely characterizes the breakage event.

The breakage detection approach based on the drop in the number of pixels, i.e., the size difference between the parent and the children can be regarded as an additional measure while discontinuity in gray value is proven to be adequate. In the orifice experiment, where several breakage events occurred almost simultaneously, children trajectories were required to be appropriately identified with the respective parent track and therefore size difference was the proper criterion for breakage detection. In the case of breakage in homogeneous isotropic turbulence, where only one event at a time was recorded whenever possible, no further detection operator than \mathcal{G} was required.

2.6 Ellipse fitting

In an attempt to measure the size of the aggregate beyond the number of pixels given in two directions of the image coordinate system, a standard geometric shape is chosen for parametric fitting. Fractal aggregates prepared under non turbulent flow conditions posses an anisotropic shapes and can be elongated when exposed to stresses. Because of the dynamic change in shape, an aggregate is approximated by an ellipse using the generic conic equation

$$ax^2 + bxy + cy^2 + dx + ey + f = 0 \quad (2.5)$$

for the set of boundary pixel coordinates according to a non weighted least squares fit. Fig. 2.14 shows an ensemble of aggregate shapes from different experiments which are appropriately enclosed by an ellipse.

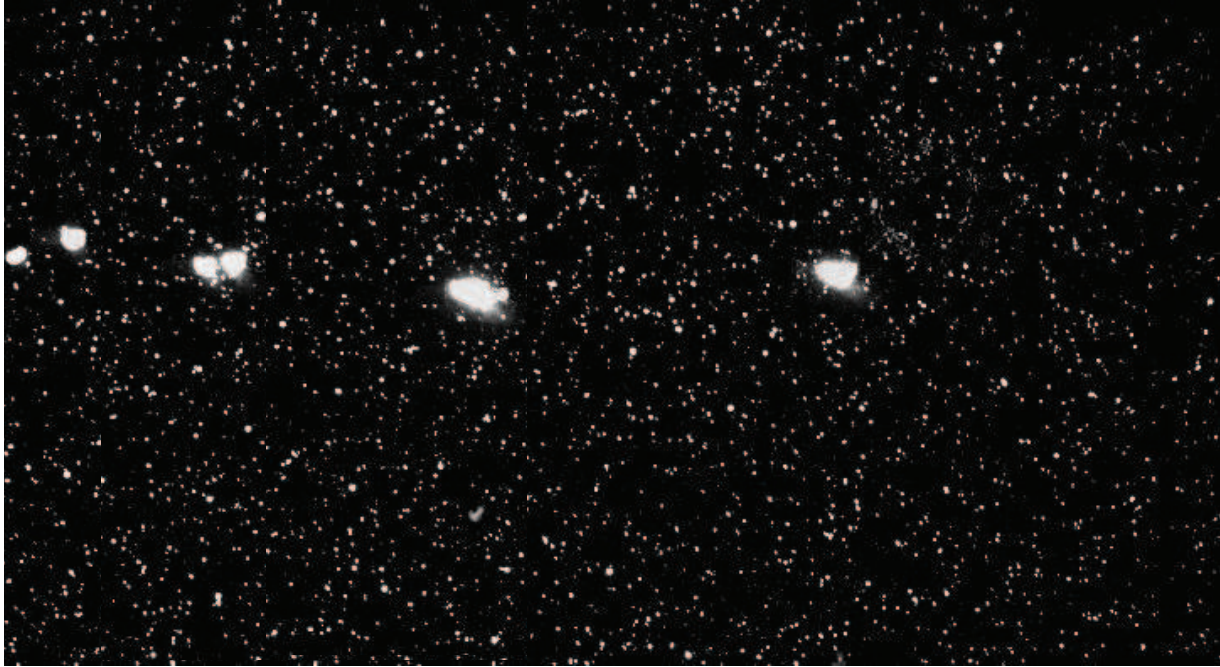


Figure 2.12: An arbitrary breakage event seen from a single camera. Here four exposures are overlaid to make a continuous sequence.

In canonical form, an ellipse is centered at $(0,0)$ and non rotational relative to principal axis. But in practise, an aggregate is subject to dynamic translation and rotation with respect to the laboratory coordinate. If the coefficient of the term xy in equation (2.5) is non zero then an ellipse is associated with a tilt. By systematic substitution, the tilt of the ellipse is removed and the orientation angle is extracted such that

$$\theta = \frac{1}{2} \text{atan}\left(\frac{b}{c-a}\right) \quad (2.6)$$

Using θ , other coefficients in equation (2.5) can be trigonometrically parameterized to reduce the conic representation to the following form

$$\frac{(X - X_0)^2}{a^2} + \frac{(Y - Y_0)^2}{b^2} = 1 \quad (2.7)$$

where (X_0, Y_0) is the center of the ellipse and a, b are the sub axis. This simplified ellipse equation (2.7) is then used to measure the aggregate with non tilted state. The perimeter of the aggregate is determined by border pixels which are connected with at least four other neighboring pixels. As a first approximation, the aggregate is measured with a single ellipse assuming smooth curvilinear periphery. After the fit, the original orientation of the aggregate is obtained back by the following rotation matrix, M

$$M = \begin{bmatrix} \cos(\theta) & -\sin(\theta) \\ \sin(\theta) & \cos(\theta) \end{bmatrix} \quad (2.8)$$

Then the difference between the actual coordinates of the perimeter pixels and the fitted coordinates, δ_k , where k = number of camera, is measured to know the accuracy of the fitting.

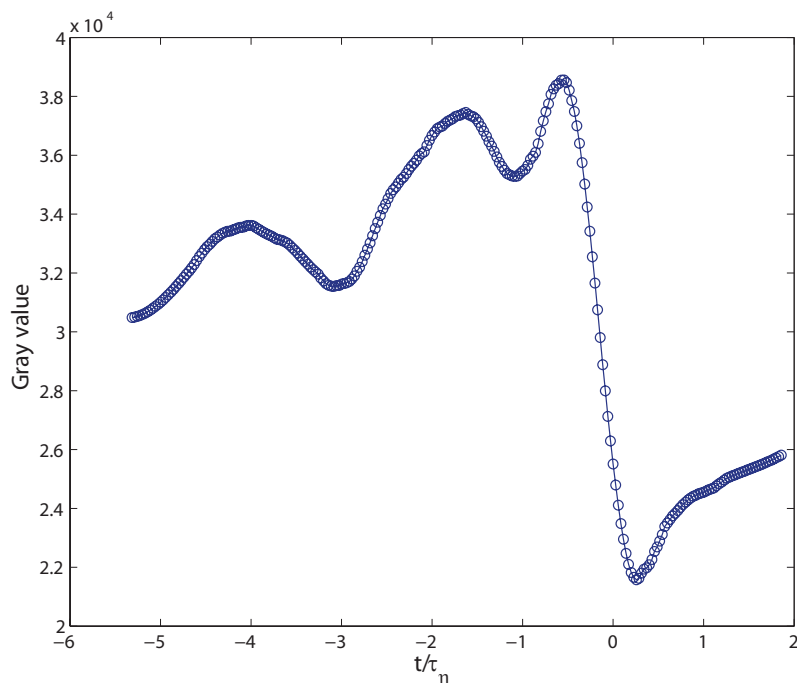


Figure 2.13: Change in gray value over time is a measure of the segmentation of an image blob. Here a breakage event is detected as the gray value drops drastically. Here the time axis is normalized by the Kolmogorov time scale and the breakage instance is pinned at zero.



Figure 2.14: Ellipse fitting for different aggregate shapes.

$$\delta_k = \sum_{i=1}^n \left\| \frac{x_i^2}{a^2} + \frac{y_i^2}{b^2} - 1 \right\| \quad (2.9)$$

On the other hand, because of the irregular boundary, an aggregate shape can deviate from the ideal elliptic shape. In this case, fitting a single ellipse might either underestimate or overestimate the actual shape (see Fig. 2.15 and Fig. 2.16). To make the estimate robust, a combination of two ellipses rather than a single one is used to measure the intricate shape of the aggregate, if necessary. This approach to accommodate two ellipses onto an aggregate starts estimating ellipses simultaneously from both ends of the transverse diameter as illustrated in Fig. 2.17. With respect to the local maxima of the boundary coordinates, an arbitrary number of nine points, four flanked on either side of the vertex are chosen to fit an ellipse. The remaining boundary coordinates are then used to fit an ellipse from the border

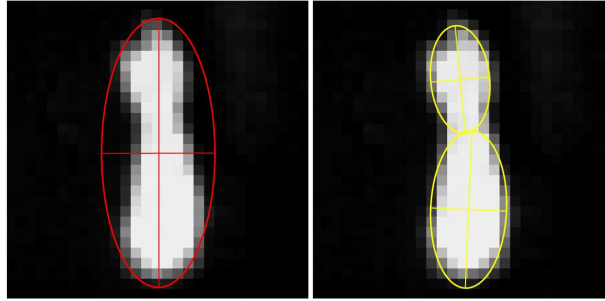


Figure 2.15: Aggregate area is overestimated while measured with a single ellipse (left). Two ellipse fitting appropriately determines the actual shape (right).

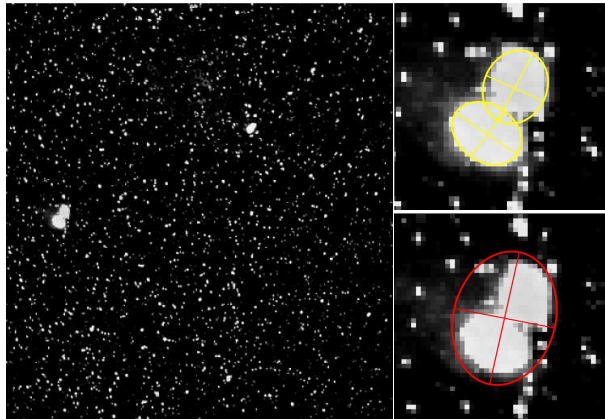


Figure 2.16: Two ellipses (top right) are more accurate than a single one (bottom right) for describing an aggregate in turbulent flow few moments before the break up.

coordinates of local minima of the tilted aggregate. The chosen boundary coordinates to fit the ellipses from both ends are mutually exclusive, i.e., as more coordinates are included to fit from the vertex, less points remain available from the other end of the transverse axis. At the end, a set of ellipses sweeps across the entire aggregate. The best pair of ellipses from all possible combination is selected based on the minimum deviation from the ideal fit employing all four camera images.

$$\Delta_k = \sum_{i=9}^n \left\| \frac{x_i^2}{\alpha^2} + \frac{y_i^2}{\beta^2} - 1 \right\| + \sum_{i=9}^{n-9} \left\| \frac{x_i^2}{\alpha'^2} + \frac{y_i^2}{\beta'^2} - 1 \right\| \quad (2.10)$$

This pair of ellipses is further examined in order to justify the necessity to approximate an aggregate shape by two ellipses. Basically two strict geometric constrains are used for the validation procedure. If $\delta\ell$ refers to the center to center distance between the two ellipses and α, α' are the two conjugate major axis then,

$$\delta\ell > \frac{1}{2} \max(\alpha', \alpha)$$

and

$$\Delta_k < \delta_k$$

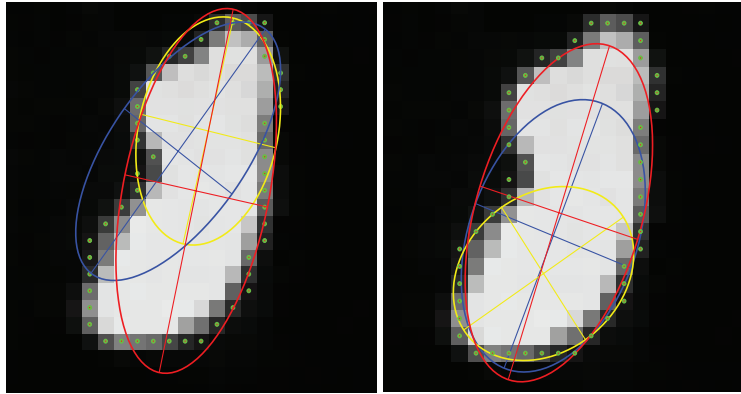


Figure 2.17: A set of ellipses are drawn using different number of boundary pixel coordinate from both ends of an aggregate in order to produce a pair for the best estimation.

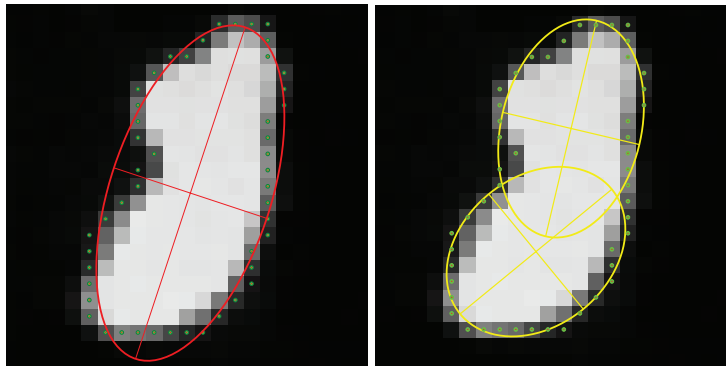


Figure 2.18: Comparison of an aggregate shape by one ellipse (left) and two ellipse (right). Here, in this, case, two ellipse are considered to be unnecessarily redundant according to preset geometric constraints.

are the necessary conditions to measure an aggregate by two ellipse. Explicitly, these two inequality conditions dictates the separation distance between the ellipses by a margin larger than the maximum of the major axis. In Fig. 2.15, this condition is satisfied and the aggregate shape is measured by two ellipses whereas for the aggregate shown in Fig. 2.18, the "two ellipse" approach is discouraged as error from pair fitting is larger than the single ellipse estimation, i.e., $\Delta_k > \delta_k$.

The major and minor axis of an ellipse, represent the characteristic length scales of an aggregate in pixel dimension. The 3D investigation domain has been mapped in order to convert the pixel scale into metric dimensions. A large set of 3D world coordinates (± 0.5 mm positions) covering the illuminated volume are projected onto the 2D-image space and the change in pixel position with respect to the spatial variation is checked. With this mapping, we can readily measure how large the aggregates are in 3D-world coordinates, i.e., the cartesian position of the aggregate is fed into the map to know the corresponding pixel dimension which is used as a local scale to convert the major and minor axis of the aggregate.

2.7 Aggregate in turbulence

Finally in this section we study the aggregate itself. The sizes of the aggregates used in the experiment are not exactly mono disperse, they rather have a distribution with standard deviation, $\sigma = 0.5$ mm and mean $\langle d_p \rangle \simeq 1$ mm. Therefore, when normalized by the smallest length scale of the turbulent carrier flow, the Kolmogorov length scale, $\eta = 0.3$ mm in our turbulent flow experiment, we have a size range $d_p/\eta \in [1, 4]$. It is noteworthy to mention that, statistically, the majority of the aggregate sizes has a size that is comparable or larger than the smallest length scale. Because of the size exceeding η , aggregates in our experiment can be affected by inertia and may deviate from that of the neutrally buoyant tracer particles used as flow markers. In this section we investigate whether the aggregates exhibit any inertial signature and consequently this is an effect of their finite size on the carrier flow. The material density of the aggregates, $\rho_p=1.06$ kg/m³ almost matches with the specific density of the carrier fluid (deionized water), $\rho_f= 1.0$ kg/m³, i.e., $\rho_p/\rho_f \approx 1$. We inject a single aggregate into the flow once at a time. Therefore, the role of the density gradient and finite size effect can be neglected as neither any global modulation of the turbulent structure due to concentration of the aggregate nor any change in rheological property of the fluid is expected. We shall systematically explore in the following how the above mentioned list of parameters shed light on the character of the large particles. At this point we would like to mention two necessary points. First, the morphology and size of the aggregates used in axysymmetric extensional flow and homogeneous isotropic turbulence are almost non differentiable. Hence, we consider the answer to the question of whether the aggregates behave passive or not to the flow, originally posed for aggregates in turbulent flow, also holds true for laminar flow. Second and importantly, the scope of the experiment in turbulent flow did not allow to produce an independent statistical analysis for quantitative conclusions on the dynamics of the aggregates. Therefore, our analysis in this particular section will be clearly biased towards exploiting the results from a list of researchers in an attempt to bridge between the deficit in statistics and our understanding on the aggregates' dynamics as well as its coupling with that of the flow.

The Stokes number, St , which is commonly used to estimate how perfectly a tracer particle follows the flow, is defined as

$$St = \frac{\tau_v}{\tau_\eta} \quad (2.11)$$

where τ_v is the particle response time to the flow, in this classical definition it is the viscous relaxation time of the particle defined as

$$\tau_v = \frac{1}{18} \left(\frac{\rho_p}{\rho_f} \right) \frac{d_p^2}{\nu} \quad (2.12)$$

and τ_η is the Kolmogorov time scale, the smallest time scale in turbulent flow.

$$\tau_\eta = \sqrt{\frac{\nu}{\epsilon}} \quad (2.13)$$

Therefore the ratio for the Stokes number unfolds as

$$St = \frac{1}{18} \left(\frac{\rho_p}{\rho_f} \right) \frac{d_p^2 \epsilon^{\frac{1}{2}}}{\nu^{\frac{3}{2}}} = \frac{1}{18} \frac{\rho_p}{\rho_f} \left(\frac{d_p}{\eta} \right)^2 \quad (2.14)$$

where

$$\eta = \left(\frac{\nu^3}{\epsilon} \right)^{\frac{1}{4}} \quad (2.15)$$

where d_p is the particle size, η is the Kolmogorov length, ρ_p and ρ_f are the specific densities of the particle and fluid respectively, ϵ is the rate of energy dissipation per unit mass and ν is the kinematic viscosity of the fluid. In principal, the Stokes number reflects the dynamic behavior of the particle relative to the carrier flow dynamics. If $St \ll 1$, the particle is considered to be passive with respect to the flow and follows the fluid motion reliably. If $St \gg 1$ then the particle dynamics departs strongly from the flow, i.e., inertial particles are insensitive to the flow and follow their own trajectories. The relevant time scales defining the conventional Stokes number are valid for point particle approximation, i.e., the limiting size of the particle is smaller than the smallest spatial scale of the flow η at which the velocity gradients are smooth and particles are able to feel the spatial and temporal changes in the flow structure. On the other hand, particles larger than η are assumed to be affected by inertia and deviate from the fluid particle dynamics. To address the finite size effect on the advected particles in turbulence i.e., for $d_p > \eta$, as in the case of aggregates, both the flow and particle time scales need to be revised appropriately in order to know if the aggregates can be legitimately thought to be passive when considering the Stokes number as a control parameter. We revisit Xu et al. [133] and Schmitt et al. [107] to obtain the modified definition of the Stokes number that accounts for the finite size particle as

$$St_p \equiv \frac{\tau_p}{\tau_d} = \frac{1}{18} \zeta \left(\frac{\rho_p}{\rho_f} \right) \left(\frac{d_p}{\eta} \right)^{\frac{4}{3}} \quad (2.16)$$

$$\zeta = \frac{1}{1 + 0.01315 Re_p^n} \quad (2.17)$$

Here the exponent n is also a function of the particle Reynolds number Re_p as $n = 0.82 - 0.05 \log_{10} Re_p$. In the limit of vanishing particle Reynolds number, i.e., $Re_p \rightarrow 0$ for size $d_p < \eta$, the viscous relaxation time τ_v is an appropriate choice for the particle response time. But for $d_p > \eta$, aggregates as the relevant example, Re_p ($Re_p \equiv u' d_p / \nu$) takes a finite value and therefore St_p incorporates a finite size particle Reynolds number correction coefficient, ζ (see Xu et al. [133]). In addition it is conjectured that particles with size $d_p > \eta$ act as a spatial filter to the turbulent flow for scales smaller than d_p and therefore, finite size particles should not feel the small scale gradients. Due to this reason, the Kolmogorov time, τ_η , is replaced by the eddy turn over time at particle scale as

$$\tau_d \equiv \left(\frac{d_p^2}{\epsilon} \right)^{\frac{1}{3}} \quad (2.18)$$

We compute the Stokes number of the tracer particle (tracer particle size, $\phi = 100 \mu m$) using (2.14) and then compare the aggregate Stokes number with velocity fluctuation, $u' = 0.03 m/s$ and $\nu = 10^{-6} m^2/s$ using both the conventional (2.14) and modified definition (2.16). We found the Stokes number for the tracer particles is $\mathcal{O}(10^{-4})$ where as the Stokes number for aggregates lies at 1% and 3% using the conventional and the modified definitions respectively. Therefore, the density effect is expected to be negligible.

In the context of very large particles with a size approaching the integral scale of the flow, i.e., $d_p / \eta \rightarrow \mathcal{L}$, the Lagrangian velocity increments [103] revealed that even large particles exhibit the intermittency signature over a wide range of time scale, an obvious indication that they also experience strong acceleration

events similar to small particles. The acceleration variance, $\langle a_p^2 \rangle$, of the large particle is a measure of how intensely they feel the strong turbulent event. Among others, the systematic investigations by Xu et al. [133] and Qureshi et al. [103] revealed that the tails of the acceleration PDF of the large particles get narrower with growing particle size. That means, the acceleration variance decreases with increasing particle dimension or in other words the insensitivity to strong events grows with larger particles. Qualitatively, the pressure gradient causing the particle motion is averaged over the larger space with the larger particle size. This impact of the finite size on acceleration reflects the fact that large particles filter the drastic turbulent events which is attributed to a longer particle reaction time to the flow. Based on the scaling between acceleration variance and size in the inertial range, i.e., $\langle a_p^2 \rangle$ decreases with $(d_p/\eta)^{-2/3}$. Qureshi et al. [103] drew a demarcation on size beyond which the attenuation of $\langle a_p^2 \rangle$ is pronounced. Finite size effects start to set in at about $5 < d_p/\eta < 15$. An independent study from Xu et al. [133] showed that it starts at about $d_p/\eta > 7$. In essence, the critical size of the large particle behaving like the tracers is $d_p/\eta \simeq 5$ (see, e.g., Qureshi et al. [103], Brown et al. [22] and Volk et al. [129]). This is also supported by the results from an optical investigation by Voth et al. [130] in fully developed turbulence showing that $\langle a_p^2 \rangle$ for the size $d_p/\eta \leq 5$ scales correctly in the viscous range following the Heisenberg-Yaglom law [92], i.e., $\langle a_p^2 \rangle \sim \eta^{-2/3}$. Since the upper bound of the aggregate size in our experiment is $\sim 5\eta$, above mentioned arguments suggest that the aggregate dynamics can be expected to be similar to that of flow tracers and even our biggest aggregates should not dampen the small scale features, i.e., they should be still reactive to violent events of the flow.

Arguments based on Stokes number and acceleration statistics discussed above showed clear evidence that the aggregates used in our experiment can be equivalently treated as small tracer particles. We proceed further to know whether the standard equation of motion valid for infinitesimally small particles is interchangeable for finite size aggregates or to which extent the equation should be refined by addressing the finite size issue in order to make it functional for the aggregates. The interaction between the carrier fluid and a transported particles is important considering the fact that the nonlinear dynamics of energy transfer among the spectrum of spatial scales is reversibly coupled with the finite size particle which results in the modification of the small scale gradients due to the particle inertial response to the fluid acceleration. The Maxey- Riley- Gatignol equation [89, 38] is an exact derivation governing the particle motion in an unsteady incompressible fluid based on the fundamental assumption restricting the particle size to be small, i.e., computationally it is assumed to be a point particle and hence does not perturb the flow, in the limit of vanishing particle Reynolds number, $Re_p \rightarrow 0$ and initial particle slip velocity, $|\mathbf{u} - \mathbf{v}| \rightarrow 0$. Following Babiano et al. [4], we recall the basic equation of motion originally derived by Maxey- Riley- Gatignol [89, 38]

$$\begin{aligned} \rho_p \frac{d\mathbf{v}}{dt} = & \underbrace{\rho_f \frac{D\mathbf{u}}{Dt}}_{\text{Fluid acceleration}} + \underbrace{(\rho_p - \rho_f) \mathbf{g}}_{\text{Buoyancy}} - \underbrace{\frac{9\nu\rho_f}{2a^2} \left(\mathbf{v} - \mathbf{u} - \frac{a^2}{6} \nabla^2 \mathbf{u} \right)}_{\text{Stoke's drag}} - \underbrace{\frac{\rho_f}{2} \left(\frac{d\mathbf{v}}{dt} - \frac{D}{Dt} \left[\mathbf{u} + \frac{a^2}{10} \nabla^2 \mathbf{u} \right] \right)}_{\text{Added mass}} \\ & - \underbrace{\frac{9\rho_f}{2a} \sqrt{\frac{\nu}{\pi}} \int_0^t \frac{1}{\sqrt{t-\zeta}} \frac{d}{d\zeta} \left(\mathbf{v} - \mathbf{u} - \frac{a^2}{6} \nabla^2 \mathbf{u} \right) d\zeta}_{\text{Basset-Boussinesq history force}} \end{aligned} \quad (2.19)$$

where ρ_p and ρ_f denote the particle and fluid densities respectively, ν is the kinematic viscosity of the fluid, a is the radius of the particle, \mathbf{u} and \mathbf{v} are the fluid and particle velocities respectively, $D\mathbf{u}/Dt$ is the Lagrangian acceleration of the fluid and \mathbf{g} refers to the gravitational acceleration. The terms in $a^2 \nabla^2 \mathbf{u}$ is the Faxén correction [35] explained in the following.

The net hydrodynamic force exerted on a particle by equation (2.19) can be decomposed into several contributions as labeled along the equation namely, fluid acceleration due to the combined effect of pressure gradient and viscous force, buoyancy due to the displaced fluid mass by the particle itself, drag force which is a function of the particle slip velocity, added mass as a result of the inertia added to the system induced by the acceleration of the fluid volume in the vicinity of the particle which is proportional to the difference between the Lagrangian acceleration of the fluid and acceleration of the particle and the last term stated in the equation, Basset history force taking into account the cumulative viscous memory effect. While equation (2.19), valid for infinitesimally small particles which are one way coupled to the carrier flow, is adequate to describe the dynamics of small and heavy particles [123], deriving a deterministic formulation for the particle motion is much more complicated when the size of the particle exceeds the dissipative scale of the flow, $d_p > \eta$ [3, 70, 69]. For finite Re_p , as in the case of the aggregates, non linear flow dynamics in the proximity of the aggregate can no longer be neglected as studied in details by Michaelides et al. [91]. The point particle approximation is violated since the aggregate size is larger than η . Moreover, density matching between the aggregate and fluid phase does not allow to simplify the equation (2.19) by excluding some terms such as pressure drag, Basset force or the effect of added mass. Therefore, besides the validity of equation (2.19) itself to estimate the dynamics of aggregate motion, recognizing the governing force terms and their necessary modification or neglecting the sub dominant force in the context of aggregate motion is non trivial.

A recent study by Zimmermann et al. [139, 140] reported a comprehensive analysis resolving the full motion of a large particle in intense turbulence with a particular emphasis on rotational intermittency and turbulence induced lift experienced by a finite size particle. Higher order dynamics between shear and vorticity at finite Re_p is attributed to the difficulty to determine the lift force. Investigation of the lift force acting on a bubble by Magnaudet et al. [83] also provides an approximate expression equally justified for the large particle in turbulent flow. The Basset history term needs to be refined as well as since Stokes flow assumption does not include the inertial response of the particle to the carrier fluid and propagation of the vorticity in the wake of the particle. However, Auton et al. [3] derived a complete solution for the added mass which is valid for any Re_p .

Among all other terms involved in the equation (2.19), Stokes drag received the most attention as the key term as reflected from the research by Bagchi et al. [9, 10], Burton et al. [23] and Zeng et al. [138]. An approach forwarded by Babiano et al. [4] and later on followed by Calzavarini et al. [25, 24] considers only three terms as the key quantities, namely, fluid acceleration, Stokes drag and added mass. It is crucial if the spatial velocity derivative or pressure gradient is subject to vary at the particle scale as in that case flow dynamics close to the particle which actively contributes to the added mass and stokes drag would yield incorrect estimates. Faxén's law, a corrective measure to Stokes' law takes into account the non linear flow dynamics at the particle scale when $d_p > \eta$. To address the size effect, the Faxén correction for the Stokes' drag performs the spatial averaging of the inhomogeneous local velocity field over the surface of the particle as

$$f_D = 6\pi \left(\frac{d_p}{2} \right) \mu_f \left(\frac{\int_{s_p} \mathbf{u}(\mathbf{x}) dS}{\int_{s_p}} - \mathbf{v} \right) \quad (2.20)$$

Moreover, Gatignol [38] emphasized the importance of the Faxén correction for the inertial effect acting on the particle, i.e., Lagrangian acceleration and added mass, by the volume average of the local flow field at particle scale. Finally, considering Lagrangian acceleration, Stokes drag and added mass as the active terms in the equation (2.19) and incorporating the Faxén corrections at $Re_p \rightarrow 0$, Calzavarini et al.

[25] proposed a first order refinement of the equation (2.19) as

$$\frac{d\mathbf{v}}{dt} = \frac{3\rho_f}{\rho_f + 2\rho_p} \left(\left\langle \frac{D\mathbf{u}}{dt} \right\rangle_{v_p} + \frac{3\nu}{r^2} (\langle \mathbf{u} \rangle_{s_p} - \mathbf{v}) \right) \quad (2.21)$$

On the basis of order of magnitude estimate, Faxén corrections are valid for $r \geq \eta\sqrt{Re_\lambda}$ [25]. Therefore, given the scope of our experiment, $\langle r \rangle \simeq 0.6$ mm, $\eta = 0.3$ mm and $Re_\lambda \sim 70$, Faxén corrections are negligible. Therefore, based on the arguments above we conclude that the aggregates used in our experiments are non inertial and their finite size does not affect the flow field.

Chapter 3

Results

This chapter contains the results of this experimental thesis. Here we compile all the relevant findings from the breakup experiments and explain them in detail. As we shall go through, the architecture of the chapter is as follows:

For the aggregate breakage in axisymmetric extensional flow, the analysis of the flow field is described in § 1. We begin with the breakup investigation by focusing on a few exemplary events. The reason why we look into some specific breakage events first is to obtain a raw impression on how we should proceed to set up the necessary analysis frame work for the entire set of breakage phenomena leading to the statistical conclusion presented in § 2. We organize our understanding derived from the experimental outcome and § 3 holds the conclusion. This will eventually facilitate to make a constructive comparison with the breakup results from the turbulent flow

We maintain the similar order of the description pattern formed for orifice experiment in the case of aggregate breakage in turbulent flow. In § 4 we study the characteristic features of the homogeneous quasi isotropic turbulent flow into which the aggregates are introduced. In this section we also interpret in brief the core idea of how the coarse grained velocity gradient tensor is computed. Starting with the representative breakup event analysis, § 5 explains the results of the breakup with § 6 containing the key findings. In § 7 we compare the breakup mechanism of aggregates in laminar and turbulent flow where we try to construct an overall understanding of the breakup mechanism which is central to this experimental effort.

3.1 Flow field analysis: Orifice

Experiments on aggregate breakage were carried out in an axisymmetric extensional flow. Since the flow field is laminar and stationary, it was not necessary to measure the velocity gradient and aggregate breakup simultaneously. Moreover, due to the difficult experimental conditions (wall bounded small observation domain and difficult optical access) it was preferred to measure the flow field and breakup phenomena separately. We obtained $\sim \mathcal{O}(100)$ breakage events in laminar and stationary flow condition in the orifice and analyze the break up mechanism based on the previously measured velocity field.

For the current experiment, the field of view extended from ~ 4.5 mm upstream of the orifice to approximately 15 mm downstream of the channel entrance. The length of the channel is 20 mm, which means we did not include the entire channel inside the field of view. There are two reasons that dictate the choice. First, a steep increment in velocity due to abrupt contraction in flow cross section is expected to trigger the breakup around the orifice entrance and we are primarily interested in capturing the events particularly at that specific location. Second, considering the possibility that either a fragment might undergo further breakup deep inside the channel, i.e., a cascade of breakage or even an aggregate itself surviving from the anticipated zone of breakage, the field of view should ideally extend all along the channel length. But in practise, finding an optimal focus for every part of the domain is a non trivial technical issue. To avoid the compromise on focus that could have an adverse effect on particle detection, we had to strip off a length of ~ 5 mm from the end of the channel and this exclusion did not prove essential in terms of detecting breakage. Fig. 3.1 shows an ensemble of the tracer trajectories together with the channel geometry from different viewing angles. The green and red dots refer to the beginning and end

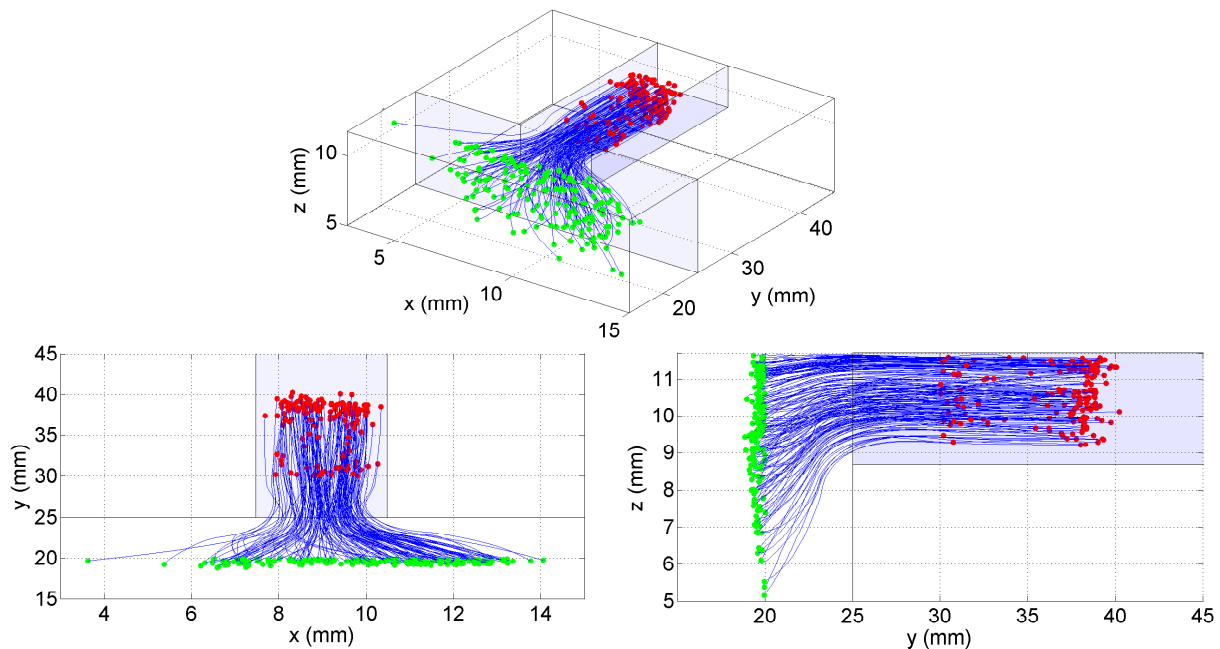


Figure 3.1: A set of flow trajectories from the stationary flow in the orifice. The selection of these trajectories are conditioned such as to pass the linear distance of ~ 5 mm across the orifice entrance which is located at 25 mm downstream. The beginning and the end of a trajectory are marked with green and red circles respectively.

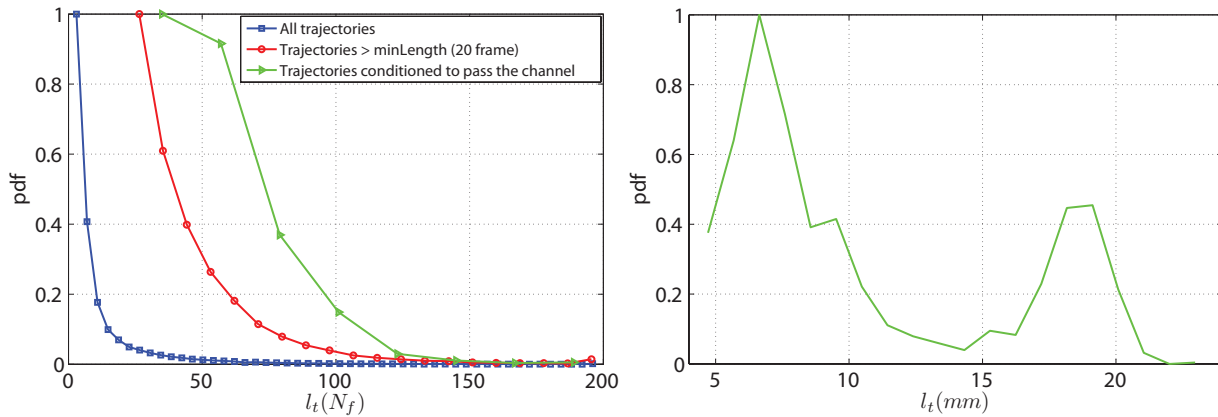


Figure 3.2: Pdf of the trajectory length in the orifice experiments. (left) Trajectories are measured in number of frames they are tracked and an exponential decay in finding the longer tracks is observed. Trajectories conditioned to pass the channel are also shown on the right with the trajectory lengths in mm. The second peak is due to finite size of the domain, i.e. there is a cut off when particles leave the field of view.

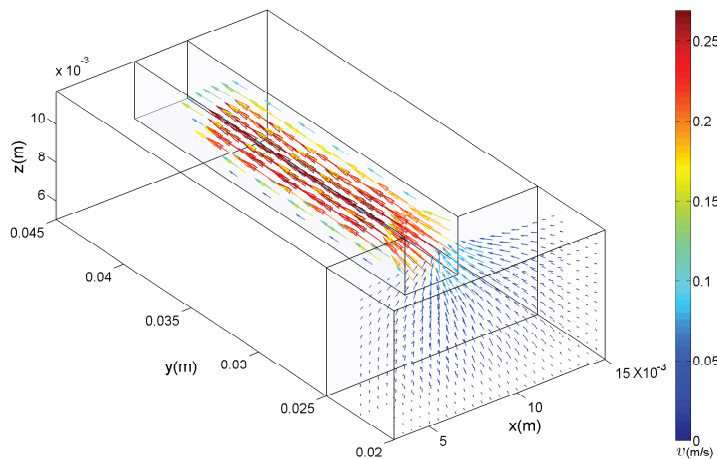


Figure 3.3: Velocity vectors labeled by magnitude in orifice showing the stationary flow. From ~ 3 mm upstream of the orifice to the entrance, the velocity grows almost an order of magnitude due to the abrupt contraction in flow regime.

of a trajectory, respectively.

The orifice entrance is located at $y = 24.5$ mm upstream with respect to the origin of the laboratory coordinate. The set of trajectories shown in Fig. 3.1 sets off ~ 5 mm prior to the channel and is tracked over a length of ~ 15 mm. However, there are numerous shorter trajectories. Only trajectories longer than ten frames are taken into account for the calculation of the velocity gradient. Fig. 3.2 shows the probability density function of the trajectories for the whole data, for trajectories longer than 20 frames and for trajectories that cross the orifice entrance. It is clear that the length of the trajectories, ℓ_t , increases with decreasing population. There is an order of magnitude increase in trajectory length when the length threshold is doubled from ten frames to twenty as indicated by the blue and red curves respectively. The

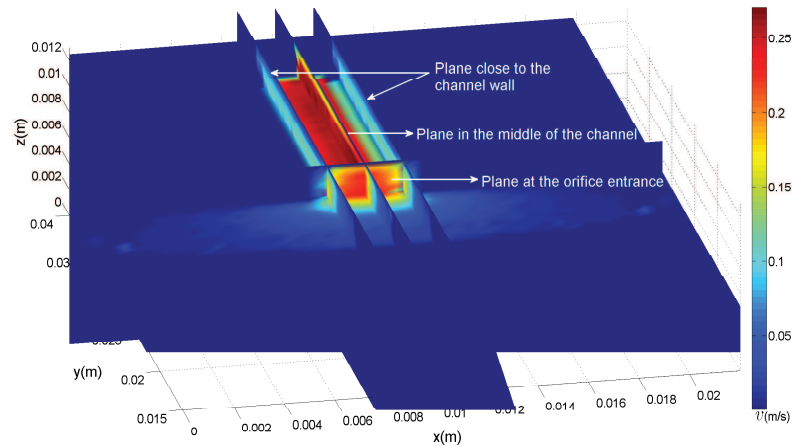


Figure 3.4: Velocity magnitude shown in three different locations, i.e., close to the channel walls and along the center line of the flow. There exists a high velocity gradient between the wall and the middle of the orifice within a distance of 1.5 mm.

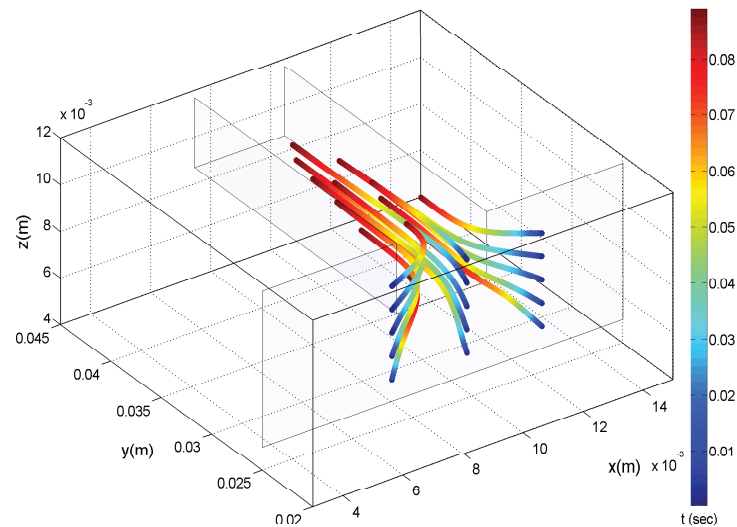


Figure 3.5: A set of trajectories starting from different locations in the flow field labeled with the time they require to flow through the orifice. From the beginning of the tracking of an aggregate it takes ~ 40 milliseconds to reach the orifice.

distribution is bimodal (see Fig. 3.2 (right)) and conditioned such that the trajectories should be spanned across the orifice entrance by a spatial margin of the orifice width (3 mm) on either side. Most of the trajectories can not be tracked beyond $\sim 30\text{mm}$ downstream (i.e., $\sim 5\text{mm}$ behind the orifice entrance). A decrease of the number of trajectories with length is typical for this kind of experiments (see e.g., [74]) and is attributed to the combined effect of ambiguity in detection, solid boundary of the investigation domain somewhat blocking the stereo angle of the cameras, out of focus problem, fluctuation of the illumination intensity and unequal scattering intensity of the tracer particles. The field of view ends at $\sim 40\text{mm}$ downstream. There are some trajectories that could be tracked up to the end of the observation

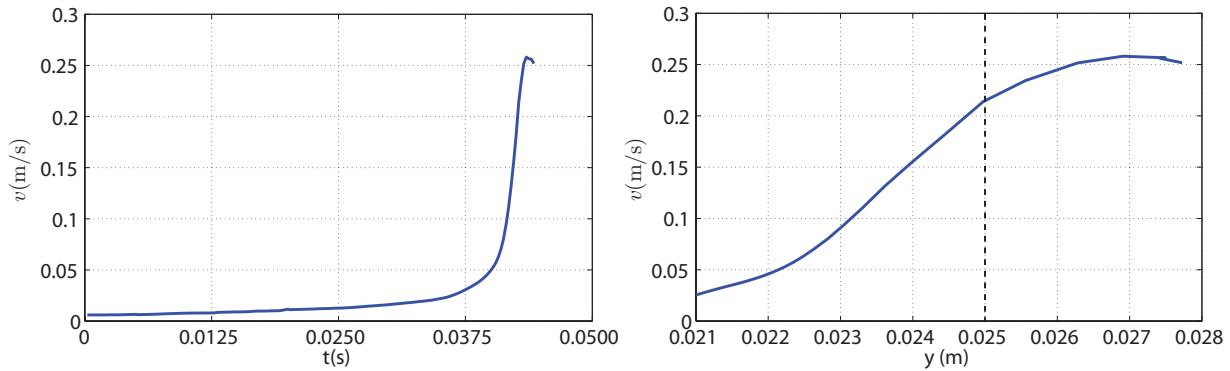


Figure 3.6: Ensemble average of the velocity over time and stream wise direction. It takes about 40 milliseconds for the velocity to grow almost an order of magnitude across the observation window, but in fact it takes ~ 1 millisecond to attain the largest velocity increment close to the orifice (left). The figure on the right shows the monotonic increase of the velocity over the stream wise distance.

domain. This particular set of trajectories is responsible for the bimodal distribution.

The Lagrangian measurements of the velocity are interpolated onto a uniform Eulerian grid of $\Delta \ell = 0.5 \text{ mm}$ spacing and the spatial derivative $\frac{\partial u_i}{\partial x_j}$ is obtained from the grid. In an axisymmetric converging flow generated by a sudden contraction, a sharp increase in velocity is observed close to the constricted regime. Fig. 3.3 shows the velocity magnitude along the streamlines. With a volumetric flow rate of 88 ml/min, the velocity grows from about $v = 4 \text{ mm/sec}$ in the chamber to approximately $v = 25 \text{ cm/sec}$ in the channel. Fig. 3.4 illustrates the velocity magnitude distribution in different cross sections, e.g., at the near wall region inside the orifice, in the middle of the orifice and in front of the orifice entrance. An equal magnitude in velocity, $v \cong 10 \text{ cm/sec}$, close to both walls of the channel quantitatively proves the axisymmetry of the flow pattern. Relative to the flow direction, crossing between the longitudinal plane through the mid section of the channel and an orthogonal plane placed exactly at the channel opening shows the spatial extent of the maximum velocity that starts from $\sim 1 \text{ mm}$ in front of the orifice position and extends to the limit of observation domain, i.e., $\sim 15 \text{ mm}$ downstream from the orifice. However, comparing the velocity in the near wall region with the velocity inside it, we found that within a millimeter range in span wise direction, the velocity increases by a factor three. This high velocity gradient causes large shear and is responsible for a shear driven breakup of aggregates passing close by the channel boundary. For an order of magnitude increase in velocity, it takes merely 40 milliseconds over a distance of $\sim 4 \text{ mm}$ upstream from the orifice as can be seen from the ensemble average of the velocity (see Fig. 3.6).

The initial motivation was to investigate the aggregate breakage in a purely elongational flow generated by an abrupt contraction in flow regime. During the recording we observed some aggregates are broken as well when they were passing close to the wall. Therefore, breakage due to elongation and shear took place in the orifice set up. Away from the wall, near the center line of the orifice, the velocity profile of the uniaxial extensional flow in eigen frame can be defined as

$$\mathbf{v} = \begin{bmatrix} v_1 \\ v_2 \\ v_3 \end{bmatrix} = \begin{bmatrix} \dot{\gamma}(t)e_1 \\ -\frac{\dot{\gamma}(t)}{2}e_2 \\ -\frac{\dot{\gamma}(t)}{2}e_3 \end{bmatrix} \quad (3.1)$$

Here in equation (3.1), $\dot{\gamma}(t)$ and e_i refer to the rate of stretching and the directions of the eigen frame of the velocity gradient tensor respectively where a strong stretching is exerted along the e_1 direction while the aggregates are squeezed across the $e_2 - e_3$ plane. On the other hand a simple shear flow is unidirectional, i.e.,

$$\mathbf{v} = \begin{bmatrix} v_1 \\ v_2 \\ v_3 \end{bmatrix} = \begin{bmatrix} \frac{\sqrt{2}}{2} e_1 \\ 0 \\ \frac{\sqrt{2}}{2} e_3 \end{bmatrix} \quad (3.2)$$

Any flow can be constructed as the superposition of purely elongational and purely rotational flow [72]. Compared to the simple shear flow, an elongational flow delivers a more pronounced effect to the distortion of aggregates as there exists no vanishing velocity component, i.e., aggregates are exposed to the variable velocity around the surface as they are transported along a straining flow stream line. Therefore, aggregates experience strong acceleration whereas the pure shear, in absence of acceleration, execute a torque on the aggregates which is obviously less effective to induce breakage. Hence stretching of an aggregate which could lead to the disintegration ceases in the vicinity of the walls where the rotational effect of the shear is as strong as the strain. This is almost an ubiquitous phenomenon for the objects like polymer chain tumbling and folding in shear flow. But the fractal aggregates used in this experiments are seen to be ruptured along the solid boundary, not as a mere form of surface erosion but as a discrete separation into parts.

To study the structure of the velocity field, we take a closer look at the measured velocity gradient, A_{ij}

$$A_{ij} = \frac{\partial u_i}{\partial x_j} \quad (3.3)$$

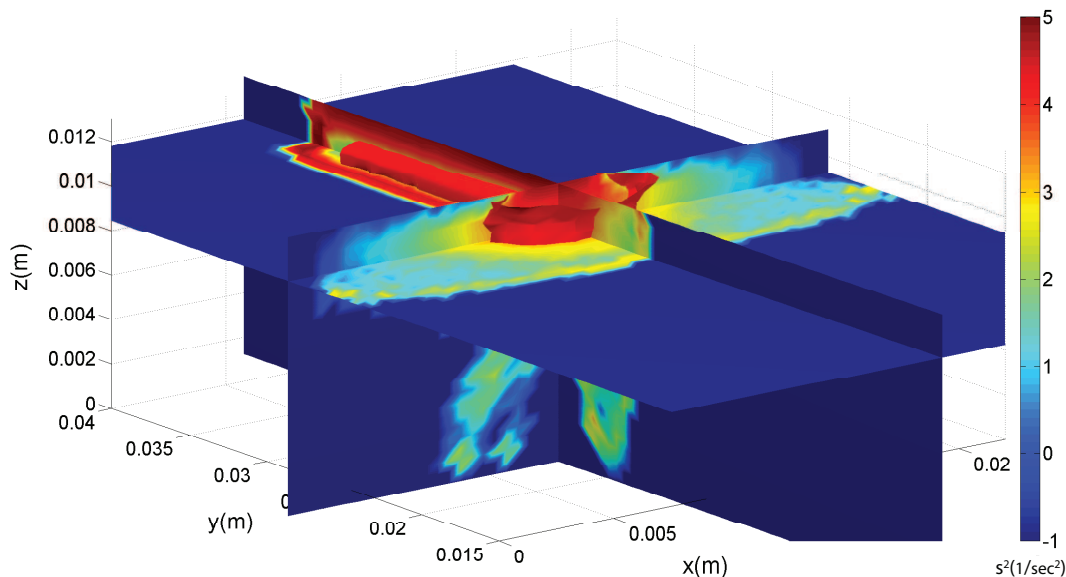


Figure 3.7: s^2 (1/sec²) contour on \log_{10} scale. An isosurface of the maximum strain is labeled in red that spans from the front of the orifice and exists inside the channel close to the wall. This isosurface of the maximum s^2 provides a qualitative impression for the most probable location for the breakup.

A_{ij} is a second rank tensor, i.e., it consists of nine components in three dimensions. The velocity gradient A_{ij} can be split into symmetric and skew symmetric parts as

$$A_{ij} = S_{ij} + R_{ij} \quad (3.4)$$

where

$$S_{ij} = \frac{1}{2} \left(\frac{\partial u_i}{\partial x_j} + \frac{\partial u_j}{\partial x_i} \right) = \frac{1}{2} (A_{ij} + A_{ji}) \quad (3.5)$$

$$R_{ij} = \frac{1}{2} \left(\frac{\partial u_i}{\partial x_j} - \frac{\partial u_j}{\partial x_i} \right) = \frac{1}{2} (A_{ij} - A_{ji}) \quad (3.6)$$

The symmetric part of A_{ij} represents the rate of strain tensor, s_{ij} whereas the anti symmetric part represents the rate of rotation tensor, R_{ij} . Since the velocity field is divergence free for incompressible flow, i.e., $\nabla \cdot \mathbf{v} = 0$, the trace of s_{ij} sums up to zero, $\sum \Lambda_i = 0$. Here, the Λ_i 's refer to the eigen values of s_{ij} and the corresponding mutually perpendicular eigen vectors λ_i determine the principal axis of s_{ij} . By convention, Λ_1 represents the most stretching eigen value and is always positive, i.e., $\{\Lambda_1 \in \mathbb{R} | \Lambda_1 > 0\}$ and Λ_3 is the most compressive one and is always negative, i.e., $\{\Lambda_3 \in \mathbb{R} | \Lambda_3 < 0\}$. The intermediate eigen value, Λ_2 can be either compressive or extensional.

Along a principal direction, for $\Lambda_1 > 0$, a fluid blob is subjected to the stronger extension and for $\Lambda_3 < 0$ it feels the stronger compression. The intermediate eigen value Λ_2 can exert either extensional or compressive force in the third direction. The rotation tensor R_{ij} defines the vorticity vector as $\omega = \nabla \times \mathbf{v}$ that describes the rate of rotation of a fluid element. In the region of axisymmetric extensional flow in the orifice $\nabla \times \mathbf{v} = \mathbf{0}$, i.e., the flow is irrotational and hence only the strain can be responsible for the breakage of aggregates.

We take a closer look at the measured rate of strain, $s^2 = s_{ij}s_{ij} = \sum \Lambda_i^2$ shown in Fig. 3.7, where the color bar is in the logarithmic scale. From the figure it is evident that the contraction is characterized by an increase of s^2 over several orders of magnitude. More precisely, in the chamber s^2 is on the order of $0.1-1 \text{ sec}^{-2}$ and reaches the values on the order of 10^4 sec^{-2} in the center of the orifice. The isosurface marked in red renders the maximum strain which appears close to the orifice entrance and extends inside the orifice embracing the channel boundary. Therefore, at the orifice, both the contraction and the wall shear give similar contributions to the total stress. Beyond the orifice and deep inside the narrow channel, as the velocity profile quickly converges to the laminar profile of a rectangular duct, the contribution of the boundaries will be dominating.

We gain further insight into the flow field through the eigen analysis of s_{ij} . Fig. 3.8 shows the principal directions of s_{ij} , i.e., the three eigen vectors within the investigation domain. The most extensional eigen vector is colored in red, the most compressive one is in blue and the intermediate one is in green. While the role played by λ_1 and λ_3 is straight forward regarding the type of the stress they apply on the aggregate, we focus on λ_2 that can be both extensional and compressive. The probability density function of the Λ_i 's, i.e., the magnitudes of the eigen values (see Fig. 3.8 right) shows that intermediate eigen vector is mostly compressive in nature. It is instructive of the fact that a fluid element approaching the orifice will be deformed due to the combined stress exerted by all three principal components of s_{ij} which we can confirm by looking at the presence of all the three eigen vectors of the strain tensor prior to the orifice entrance. It is noteworthy to mention that, the intermediate eigen vector, λ_2 also takes part in compression together with the conventionally compressive λ_3 approximately 3 mm upstream of the orifice as seen from the eigen vector map from Fig. 3.8. Before reaching the channel, the flow is in fact almost two dimensional, i.e., there is an approximate "radial" symmetry and $\Lambda_2 \sim \Lambda_3$, i.e., the intermediate

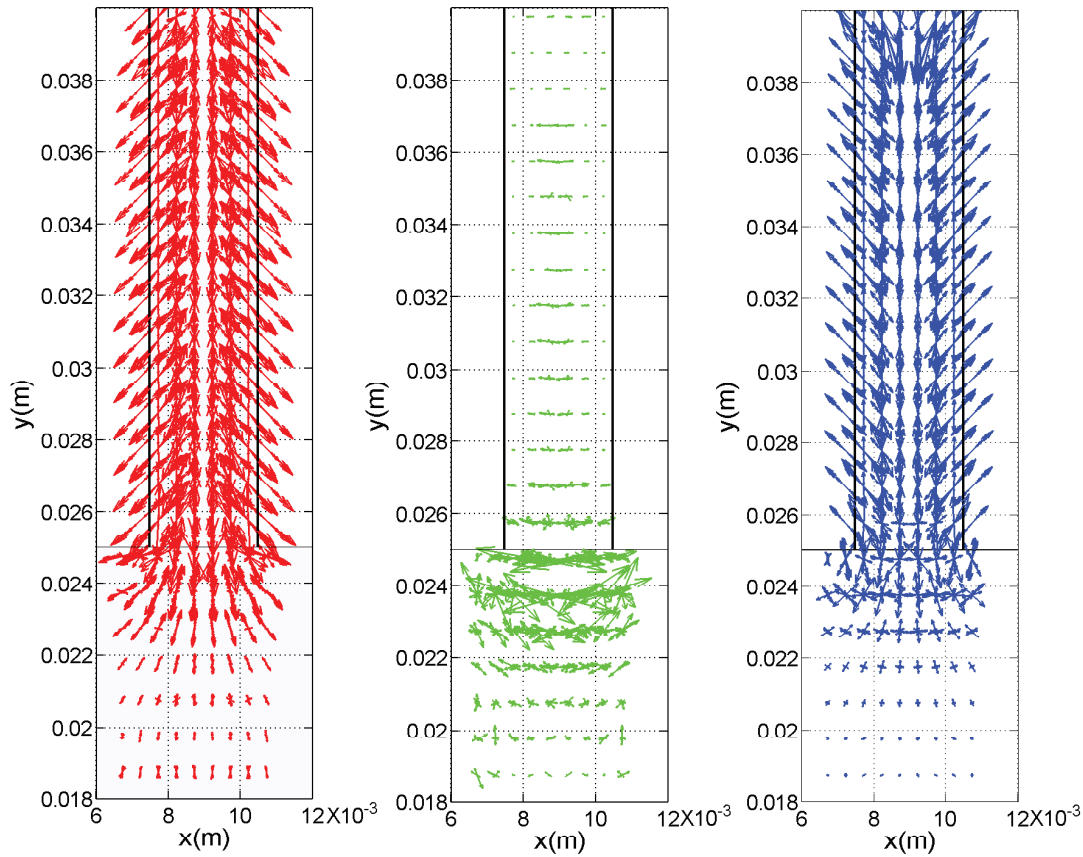


Figure 3.8: The most extensional, intermediate and the most compressive eigen vector of the rate of strain tensor s_{ij} , i.e., λ_1 (red), λ_2 (green) and λ_3 (blue) respectively multiplied with their corresponding eigen values Λ_i in stream wise view. In front of the orifice, the intermediate eigen vector (green) has a considerable effect and comparing with the most compressive one (blue), it can be noticed that $\Lambda_2 \sim \Lambda_3$.

and the compressive eigen vectors are nearly indistinguishable. When looking along the stream wise direction of the flow, as in Fig. 3.9 (left) where the most extensional and compressive eigen vectors are illustrated bidirectionally, it becomes distinctively clear that uniaxial straining exists near the center line of the converging flow, away from the surrounding walls of the chamber and channel. The vertical line marks the position of the orifice and the height of the channel spans from 9-12 mm. Thereafter, deep inside the channel, Λ_2 becomes vanishingly small which leaves Λ_1 and Λ_3 in balance. Close to the wall inside the channel and near the chamber boundary located at 25 mm downstream, extensional and compressive stress align themselves at 45° with respect to the wall. This is characteristic of the pure shear similar to plain Couette flow. To further supplement our observation, we take a close look at the iso surfaces of λ_i 's. On the basis of an empirical threshold, the ratios $|\frac{\Lambda_2}{\Lambda_1}|$ and $|\frac{\Lambda_2}{\Lambda_3}|$ produce the iso surfaces of Λ_1 (red surface) and Λ_3 (blue surface) respectively, shown in Fig. 3.10. We notice that, the iso surfaces of the most extensional and compressive eigen vectors almost embrace each other close to the wall inside the orifice which reconfirms the presence of simple shear inside the channel. Therefore, the aggregates passing close to the boundary are expected to be sheared rather than elongated.

In short, in this first paragraph 3.1, we characterized the axisymmetric extensional flow field generated in

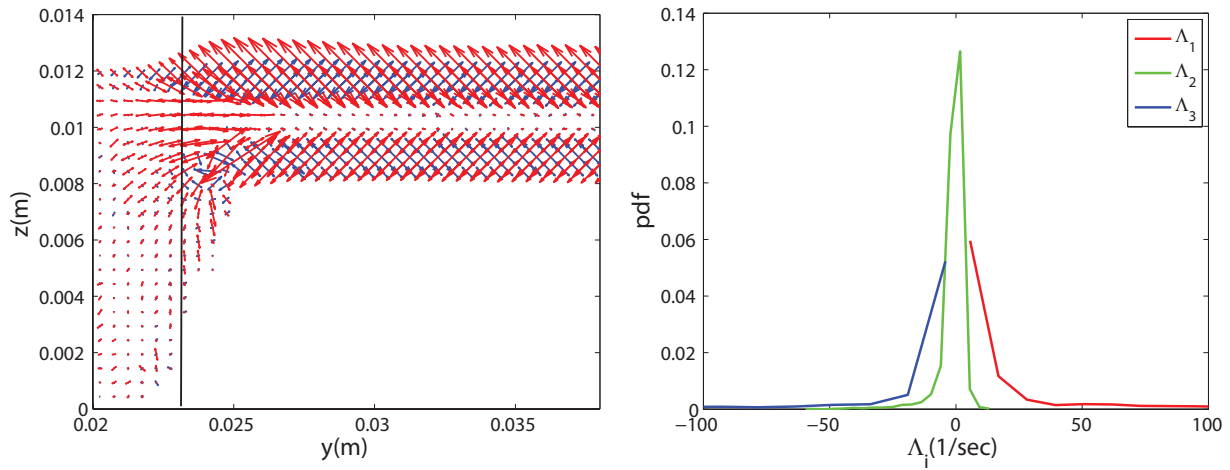


Figure 3.9: Orientation of the most extensional and compressive eigen vector of the rate of strain tensor, i.e., λ_1 (red) and λ_3 (blue) respectively along the stream wise direction (left) and the pdf of their magnitudes, Λ_i (right).

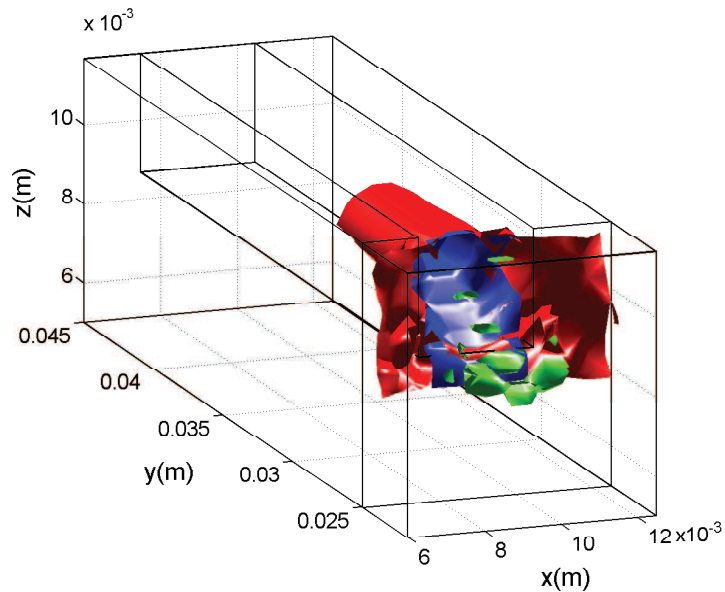


Figure 3.10: Iso surfaces of the eigen values Λ_i of the rate of strain tensor s_{ij} in the orifice. Red, green and blue refer to the most extensional, intermediate and the most compressive eigen value iso surface respectively. Iso surfaces of Λ_1 and Λ_3 nearly co exist inside channel.

the orifice setup and confirmed that 1) strain, s^2 responsible for the breakup of the aggregates increases monotonically as the flow converges towards the orifice which gives an impression of the most probable location for the breakage, 2) eigen analysis of s_{ij} shows the region of uniaxial straining in front of the orifice and simple shear inside the orifice. We shall see in the next section 3.2 how aggregates are broken when introduced into the orifice setup.

3.2 Breakage analysis in orifice

3.2.1 Example analysis

Brownian motion driven aggregation produces a range of different size aggregates. Not all of the aggregates are worth investigating with respect to the breakage mechanism. In this experiment, we consciously discarded those aggregates whose size is larger than the width of the orifice (see Fig. 3.11) as they mostly undergo rigid body elastic deformation and resist breakup.

On the other hand, some breakage events from the aggregate size range below the channel width, 3 mm, are hard to account for due to the difficulty to definitely detect the detached parts as fragments. Fig. 3.12 shows few examples where the breakup is inconclusive from a visual and technical detection point of view and hence not considered for the analysis. Therefore, filtered by the aggregate's initial size and the pattern of breakage, we select the events which provide a certain number of distinguishable fragments shown in Fig. 3.13 and Fig. 3.14 as the standard reference events. Here the breakup as it happened during the experiment, is recreated in 2D by compiling four different time instances which illustrate the course of the event. In Fig. 3.13, an aggregate breaks into two fragments whose Lagrangian tracks are shown in Fig. 3.15 (left) and in Fig. 3.14 an aggregate is subjected to successive segmentation whose Lagrangian tracks are seen in Fig. 3.15 (right). The blue trajectory refers to the parent and the red ones are the fragment tracks. In situations where an aggregate might undergo continuous fragmentation producing multiple pieces almost instantaneously, we limit the choice to select events based on a maximum of four pieces of fragments (see Fig. 3.14) above which breakup resembles a thread of apparently detached parts which are hard to judge as distinct fragment entities.

Both the exemplary breakage events illustrated in Fig. 3.13 and Fig. 3.14 take place ~ 1 mm in front of the orifice where $s^2(1/sec^2)$ is maximum. The initial size of those two aggregates are comparable, i.e., $\sim \mathcal{O}(1mm)$. When s^2 is measured along the trajectories, we found that the position at where they broke, are superior in the magnitude of the strain responsible for the breakup (see Fig. 3.16). The only, but not the least, differentiable feature between these two breakup events is the mode of breakage. Composed of same primary particles, aggregates of equal size can be disintegrated into the different number of parts although the critical s^2 for both is identical. A crude consensus can be developed on this phenomenology that, apart from the size and s^2 , inhomogeneous mechanical strength could also determine the onset of

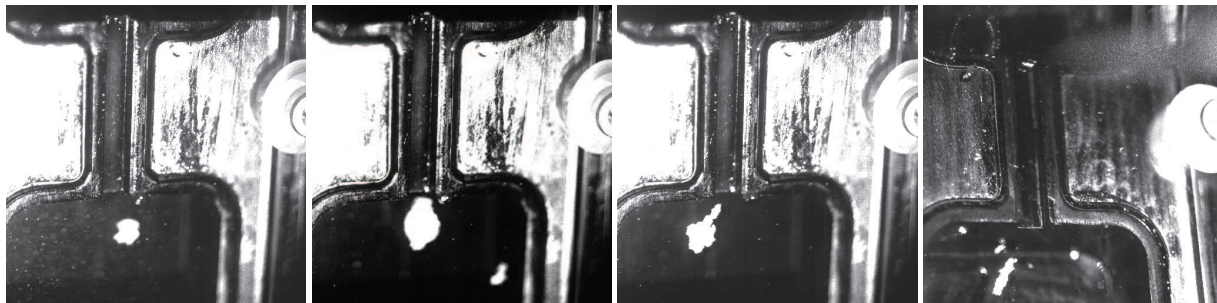


Figure 3.11: Aggregates of size larger than the orifice width are not considered for analysis. Some aggregates could grow as large as the orifice width of 3 mm or larger than that. Those aggregates are observed to be only elongated as long as the orifice length without breaking and hence do not qualify for the analysis.



Figure 3.12: Ambiguous breakage events. The images are processed to remove unnecessary reflection around the aggregates for the purpose of appropriate detection. Breakups are ambiguous in the sense that fragments seem to be connected by thin parts rather than visibly separated from each other.

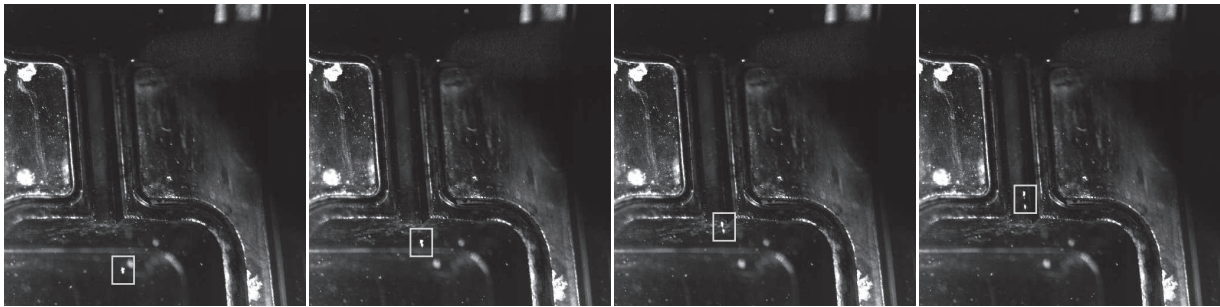


Figure 3.13: An aggregate breaks into two parts is shown in four different snapshots of a sequence in the orifice

breakup as well as the number of produced fragments. Looking at the breakage event in Fig. 3.14, one could realize that diffusion limited aggregates exhibit irreversible deformation. Another standalone point can be noticed from this material property. Elastic behavior of the aggregates implies an amorphous structure capable to reassemble internally and helping to resist the break up (see Fig. 3.12 (left)) as opposed to instantaneous crack propagation in a rigid body along the plane experiencing the critical s^2 .

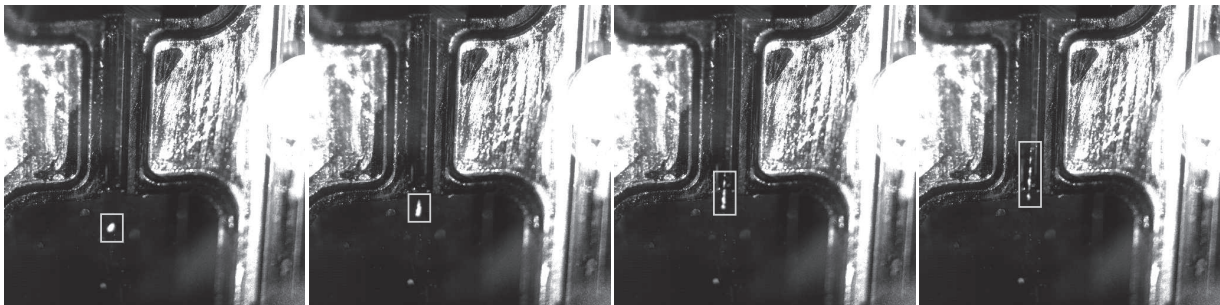


Figure 3.14: An aggregate breaks into four parts is shown in four different snapshots of a sequence in the orifice

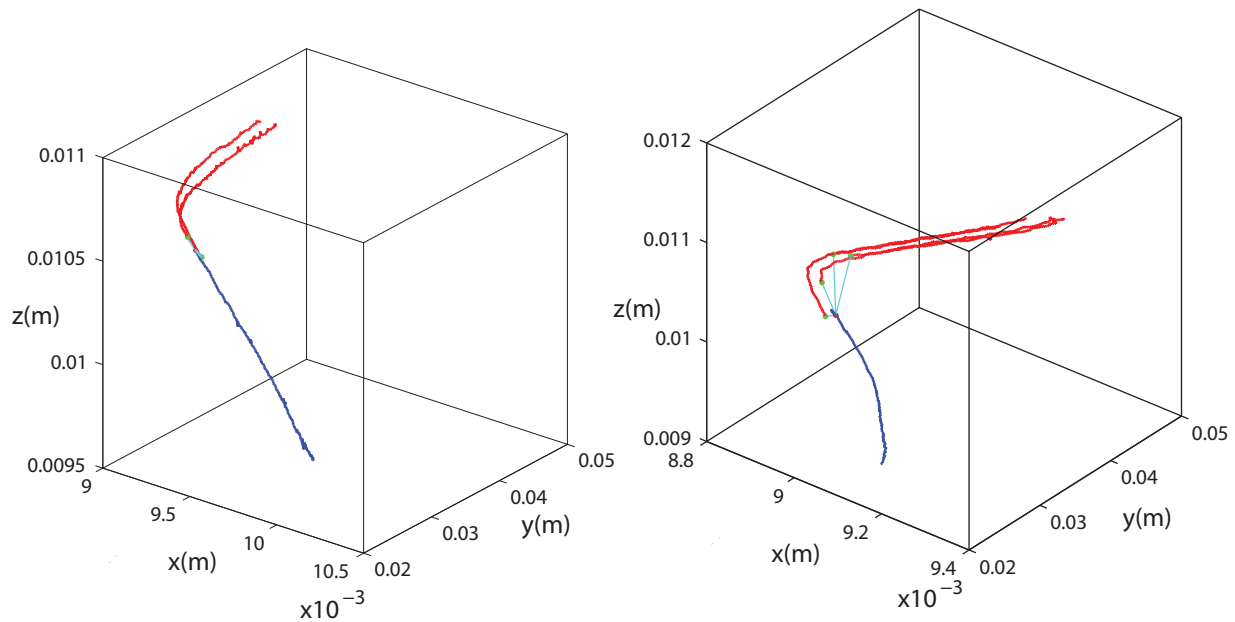


Figure 3.15: Trajectories from breakage events. (left) one breaks into two and (right) one breaks into four parts. The trajectories in blue and red refer to the aggregate and fragment trajectories. Both the events take place ~ 1 mm upstream of the orifice and the fragment trajectories run in parallel to the channel. Connection lines are drawn in order to identify the fragments with the corresponding aggregate (cyan) considering the situation when several breakup occurs within the same observation time.

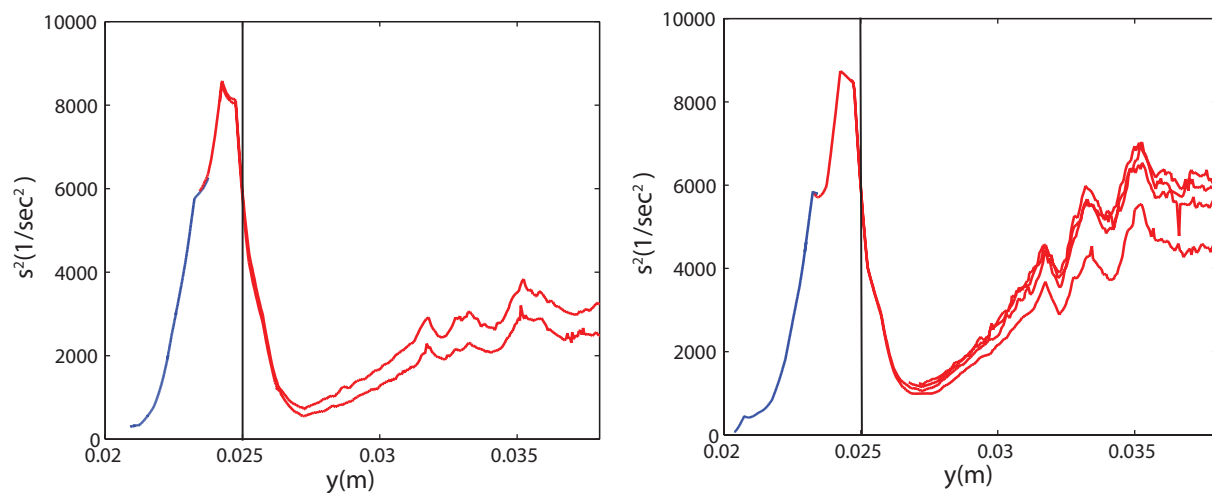


Figure 3.16: $s^2(1/sec^2)$ along the trajectories (aggregate trajectory is in blue and fragments are in red) in downstream direction. (left) One aggregate breaks into two and (right) the other one breaks into four parts and both the events take place in front the orifice approximately at the same strain magnitude. Location of the orifice entrance is indicated by the black vertical line

3.2.2 Statistical analysis

Now, we focus on the statistical results derived from all of the breakage events, order of $\mathcal{O}(100)$. In principle, we will detect the locations of the breakage, measure the strain responsible for the breakage, analyze the dominant contribution between uniaxial straining and simple shear to breakage and eventually verify the scaling law between aggregate size and strain at breakage.

In Fig. 3.17 and Fig. 3.18 we show the breakage location with the respective strain rate, $\sqrt{s^2}$. Most of the breakage take place in front of the orifice entrance where the strain is maximum. Fig. 3.19 (left) shows quantitatively that ~ 1 mm on either side of the orifice entrance which is located at 25 mm downstream, is the most probable flow domain for the breakup in converging flow at an average strain of $s^2 \sim 10^4(1/sec^2)$ (right). Some aggregates passing close to the top of the channel experience the maximum strain rate, i.e., $\sqrt{s^2} \sim 200(1/sec)$. From Fig. 3.4, comparing the velocity of the near wall region of the orifice with the velocity inside it, we found that within a millimeter range in spanwise distance, the velocity is increased by a factor of five. This high velocity gradient causes an immense shear leading to the breakup.

We look at the ratio of the intermediate and the most compressive eigen values of s_{ij} , i.e., $|\frac{\Lambda_2}{\Lambda_3}|$ to understand the contribution of shear and uniaxial stretching in the breakup process. In Fig. 3.20 and Fig. 3.21 we illustrate the breakage locations with the corresponding $|\frac{\Lambda_2}{\Lambda_3}|$. Due to incompressibility of the fluid, the trace of the rate of strain tensor s_{ij} is vanishing, i.e., $\sum \Lambda_i = 0$. If the intermediate eigenvalue Λ_2 grows close to the most compressive one Λ_3 , i.e., $|\frac{\Lambda_2}{\Lambda_3}| \rightarrow 1$ then we come up with the relation $|\Lambda_2| \sim |\Lambda_3| \simeq \frac{1}{2}|\Lambda_1|$ which implies uniaxial stretching. On the other hand, if Λ_2 is negligible compared to Λ_3 , i.e., $|\frac{\Lambda_2}{\Lambda_3}| \rightarrow 0$ then $|\Lambda_1| \sim |\Lambda_3|$ which means stretching and compression equate each other leading to the simple shear effect. Therefore, we look at the ratio of the intermediate and the most compressive eigen values of s_{ij} , i.e., $|\frac{\Lambda_2}{\Lambda_3}|$ to understand the contribution of uniaxial stretching and shear in the breakup process. In Fig. 3.20 and Fig. 3.21 we illustrate the breakage locations the in orifice in different views and show the ratio $|\frac{\Lambda_2}{\Lambda_3}|$ at those breakage spots. We found that $|\frac{\Lambda_2}{\Lambda_3}| \geq 0.5$ flanked on either side of the orifice entrance within a span of ~ 1 mm as Fig. 3.23 also shows how $|\frac{\Lambda_2}{\Lambda_3}|$ computed at the breakage

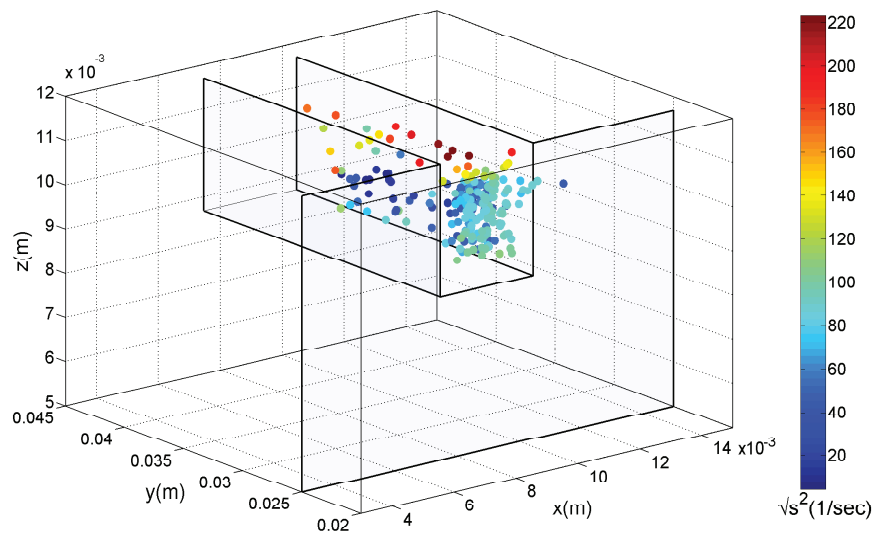


Figure 3.17: Breakage locations (isometric view) inside the flow domain labeled with the strain rate $\sqrt{s^2}$.

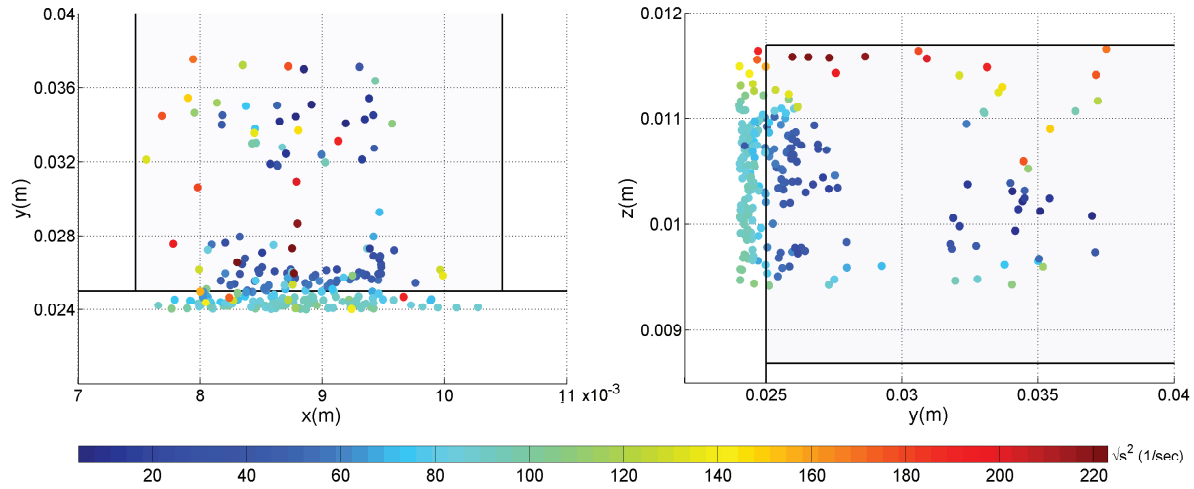


Figure 3.18: Breakage locations from the top (left) and stream wise view (right) labeled with the strain rate $\sqrt{s^2}$.

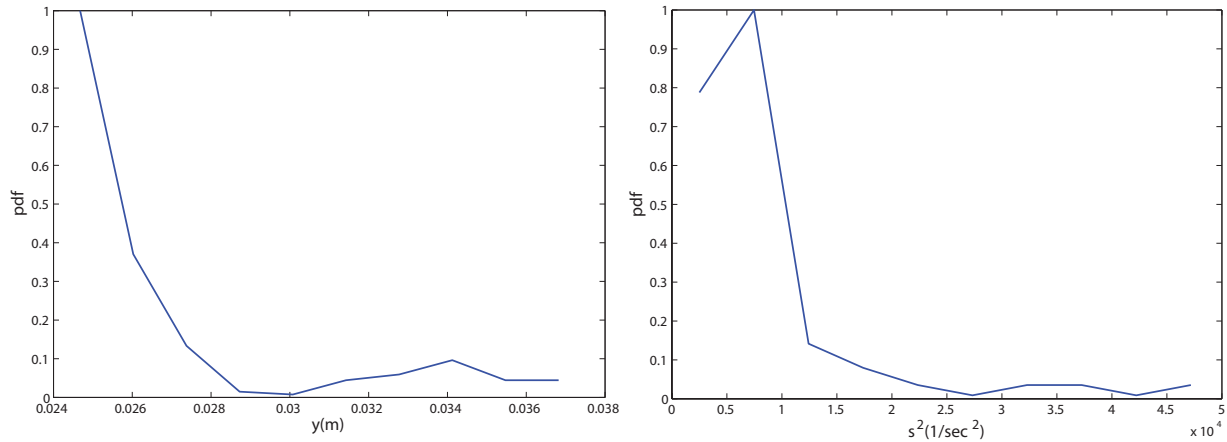


Figure 3.19: Probability density function of the breakage location (left) along the stream wise direction and the corresponding strain s^2 responsible for breakage (right).

location changes along the downstream. The position of the channel is marked by the black vertical line. This means, at those particular locations aggregates broke due to uniaxial stretching. Here we reconfirm our understanding while attributing breakup due to elongation preferably in front of the orifice by recalling the Fig. 3.8 in 3.1 in which we see that $\Lambda_2 \sim \Lambda_3$ in front of the orifice. Beyond the orifice entrance, we also found a few breakage events deep inside the channel. From Fig. 3.21 we observe that most of the events take place near the bottom and the top of the channel. At those breakage locations, the intermediate eigen vector almost diminishes as we see $|\frac{\Lambda_2}{\Lambda_3}| \simeq 0$. Hence we attribute simple shear for those breakage events.

After identifying the breakup based on elongation and simple shear, we try to understand why most of the aggregates break due to uniaxial straining and a few of them break due to simple shear considering the fact that all of them are made of the same constituent particles following a specific aggregation procedure and have comparable size. Besides this, the aggregates which are broken inside the channel raise

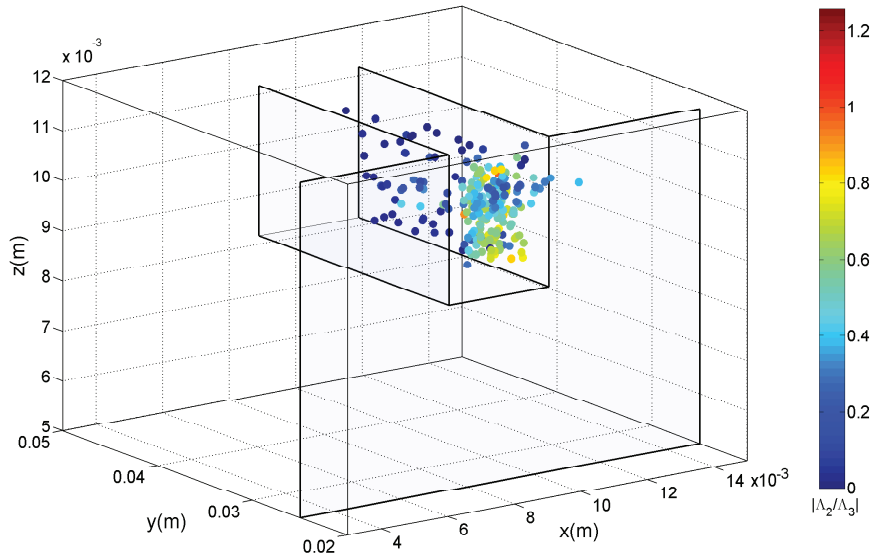


Figure 3.20: Breakage locations (isometric view) inside the flow domain labeled with the ratio of the intermediate and the most compressive eigen value $|\Lambda_2/\Lambda_3|$ of the rate of strain tensor.

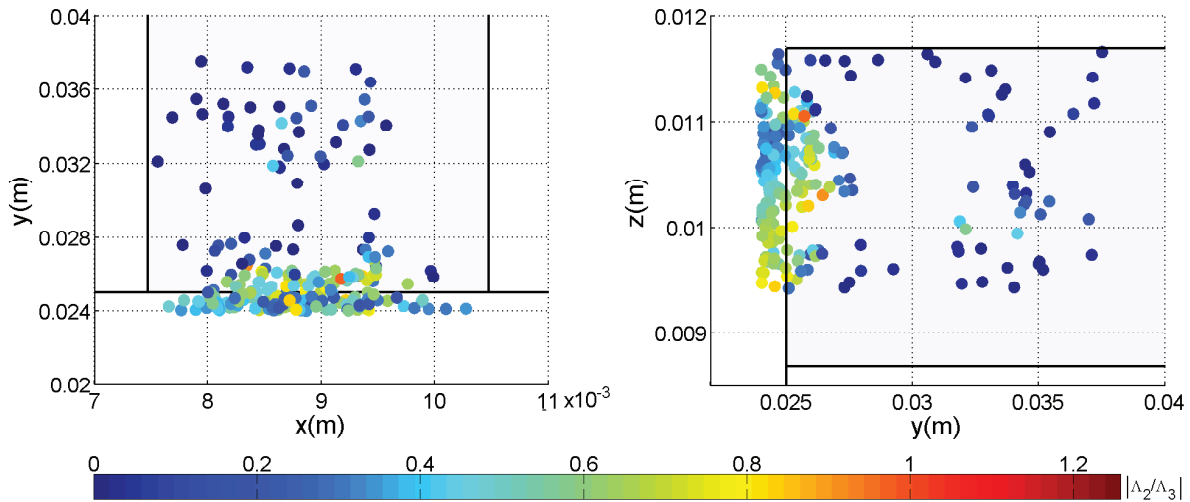


Figure 3.21: Breakage locations from the top (left) and stream wise view (right) inside the flow domain labeled with the ratio of the intermediate and the most compressive eigen value $|\Lambda_2/\Lambda_3|$ of the rate of strain tensor

another question of how those aggregates managed to resist breakup while crossing the orifice entrance where strain is maximum. To answer these questions we argue on the strength of the aggregates and the pattern of the breakage.

The strength of an aggregate is not a function of its size. Therefore aggregates belonging to the same size distribution could have variable mechanical strength. More than size, we consider physical morphology of the aggregates to be of importance to gain a better insight about the strength. The parameter fractal

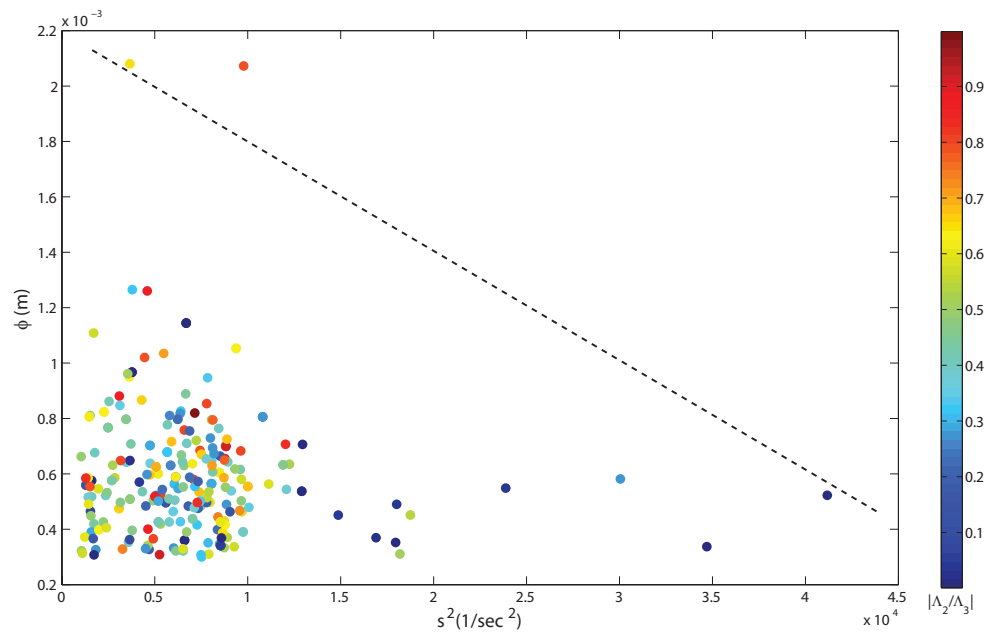


Figure 3.22: Dependency of the aggregate size ϕ on the critical strain. Besides the initial size of the aggregates as a function of the critical strain at the breakage locations, breakup due to elongation and simple shear is also identified through the ratio of the intermediate to the most compressive eigen values of the rate of strain tensor, i.e., $|\frac{\Lambda_2}{\Lambda_3}|$.

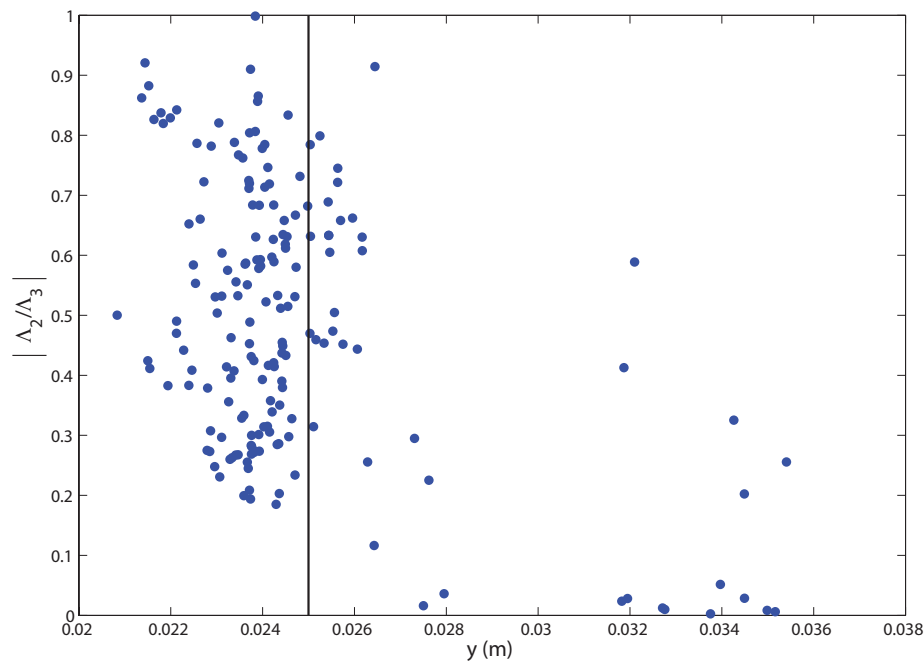


Figure 3.23: The ratio of the intermediate and the most compressive eigen value $|\frac{\Lambda_2}{\Lambda_3}|$ at the point of breakage where the breakage locations are shown in stream wise direction. The majority of the breakup takes place ~ 3 mm in front of the orifice due to the elongation, i.e., $|\frac{\Lambda_2}{\Lambda_3}| \geq 0.5$ and fewer events due to simple shear, i.e., $|\frac{\Lambda_2}{\Lambda_3}| \rightarrow 0$, are observed inside the orifice.

dimension can estimate the morphology of the aggregate. Unlike the topological dimension, the fractal dimension can take any value between one and three including the fractions as the name suggests. Lower fractal dimension refers to more open structure and weaker aggregates whereas higher fractal dimension indicates compact aggregates and therefore stronger structures. It is worth to mention that, we measured the so called population fractal dimension, d_f , of the aggregates used in our experiments which is $d_f \simeq 1.88$. That means, on an average the aggregates are nearly two dimensional objects with open structure (e.g. see Fig. 2.5). But the population fractal dimension does not represent an individual aggregate's morphology. Therefore, there might be some aggregates with relatively higher fractal dimension and hence stronger so that could survive the maximum strain zone in front of the orifice.

The way an aggregate breaks, mentioned earlier as the pattern of breakage, could also explain why we observe some breakage events inside the orifice. We refer to Fig. 3.14 to infer that an aggregate, when it undergoes breakage, experiences finite deformation which in turn indicates that as opposed to a rigid object they are elastic to some extent. This elastic property of the aggregates could lead to two possible phenomena. First, the aggregates being stretched prior to the orifice entrance could be advected unbroken to some distance downstream and then break apart in the region of simple shear. Second, a stretched aggregate can possibly undergo successive breakup. In that case, a fragment keeps breaking further in downstream inside the channel. In these particular phenomena, i.e., an aggregate breaks in the regime of simple shear as an aftermath of being elongated due to uniaxial stretching starting form in front of the orifice such that it can not sustain the structural failure or continuous fragmentation running down the channel, are the basic reasons of observing the breakup beyond ~ 5 mm from the orifice entrance. Hence we conclude that, breakup due to simple shear can not be decoupled from the initial effect of uniaxial straining in our experiment in orifice, i.e., obviously an aggregate can not escape elongation to be broken only due to simple shear.

Next we investigate the effect of aggregate size on breakup. In Fig. 3.22 we plot the initial size of the aggregate as a function of the strain at breakage. In addition, we also embed $|\frac{\Lambda_2}{\Lambda_3}|$ in the same figure to understand the size dependency of breakup due to elongation and shear. The size of the aggregates in the orifice experiment is about one millimeter. We found that, the strain required to break the aggregates increases with decreasing size. But with decreasing size the strain needed to break the aggregates does not increase linearly. We notice that, aggregates of a size in the range $\phi|\phi \in [0.3, 0.7]$ mm break at variable s^2 . That means the strength of an aggregate seem to be rather independent of its size and that explains why an aggregate of a certain size breaks at variable strain. While looking at the effect of size on the breakup due to elongation and shear, we found that almost all the aggregates are prone to be broken by uniaxial straining since for every size $|\frac{\Lambda_2}{\Lambda_3}| \geq 0.5$. Therefore, Brownian motion driven fractal aggregates are broken mainly due to elongation irrespective of the size in the range $\phi|\phi \in [0.3, 1.5]$ mm. Based on our understanding regarding aggregate size and the strain responsible for breakup, we find a so called "envelope" from Fig. 3.22 (marked by dashed line). By "envelope" we essentially define a region in $\phi - s^2$ space which distinctly shows the inverse relation between size, ϕ and the strain, s^2 .

There exists an established power law scaling between the steady state size of the aggregates and the critical strain. Steady state size of the aggregate refers to the size below which an aggregate would not undergo further fragmentation. Now it is worthwhile to investigate how consistent our prediction is with respect to the well known power law scaling. Based on the theoretical prediction of the power law behavior proposed by Zaccone et al. [136], we use the experimental result obtained from small angle light scattering (SALS) by Soos et al. [46]. The initial fractal dimension of the aggregate used in a small

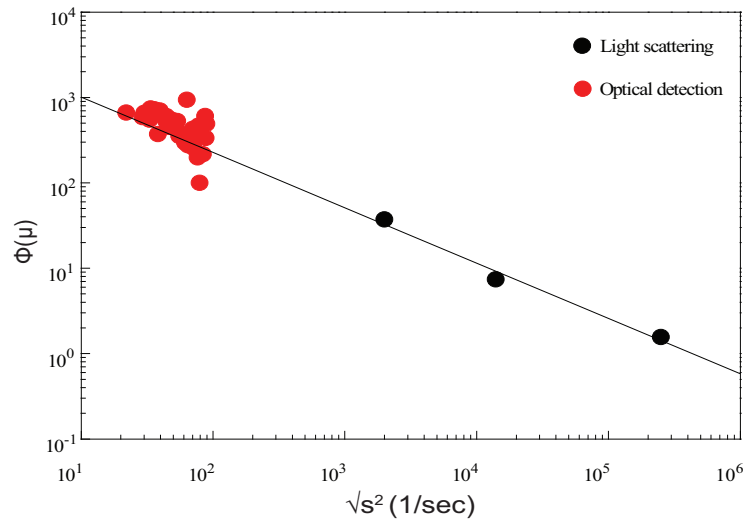


Figure 3.24: Evidence of the scaling law behavior between the size and strain is reflected as the measured data set from 3D-PTV (red) falls on the scaling results obtained from small angle light scattering (SALS) measurements.

angle light scattering experiment is approximately the same as for the aggregates used in our orifice experiment. Fig. 3.24 shows the size of the aggregate, ϕ and strain rate, $\sqrt{s^2}$ in logarithmic scale. In Fig. 3.24 we present the result of aggregate breakup in converging flow by Soos et al. [46] representing the power law scaling (black line) and append our result (red filled circles) therein to see whether the data set collapses on the scaling behavior. We observe that our measurements relating the size and strain rate do not exactly align with the line describing the scaling but rather appear to be seemingly scattered. We explain this slight discrepancy on the basis of two arguments. First, we considered the initial size of the aggregates and not the steady state fragment size as used by Soos et al. [46].

Experimental conditions do not favor to measure the authentic strain rate at which the fragments reach their steady state. In order to attain the steady state size in our current setup, the broken parts need to be reintroduced into the channel time and over again following an optimum recirculation route where the fragments might keep breaking and reach the steady state well before they actually should. On the other hand, from a technical point of view, the fast camera at full spatial resolution with an imaging frequency of 4 kHz (the temporal resolution we used during orifice experiment) can record up to ~ 3 seconds. Therefore, continuous recording over a long time is not feasible. These are the basic reasons why we used the initial size of the aggregates rather than the steady state size.

Second and most importantly, *we measured the instantaneous strain rate experimentally at the location of breakage*. Light scattering technique is capable of measuring the size of an object but not the flow field. Soos et al. [46] analyzed the flow field numerically (for the detailed description of the method see e.g., [46]). To be specific, they measured the mean steady state size of the fragments and the maximum strain rate of the flow field that produced that size. This shows the clear difference between the analysis approaches. We measure the size of the individual aggregate, not the mean initial size and the corresponding strain rate at the breakage which does not necessarily have to be always the maximum. Moreover, from Fig. 3.24 we notice that, the scaling from 3D-PTV data is concentrated within

a range of an order of magnitude in ϕ and $\sqrt{s^2}$ whereas the reference power law scaling consists of the steady state size and strain rate ranging over approximately four orders of magnitude both in ϕ and $\sqrt{s^2}$. Despite these differences, the results of aggregate breakage as observed by 3D-PTV shows significant agreement with the power law scaling between size and strain rate which is mutually complementary for both the techniques.

3.3 Concluding remark: Breakup in orifice

The synopsis of the results from the breakup of fractal aggregates in axisymmetric extensional flow generated by an orifice, i.e., a sudden contraction in the flow regime, follows as :

- Our observation domain starts ~ 4 mm upstream from the orifice entrance. It takes less than 40 milliseconds for the velocity to be increased by an order of magnitude, i.e., from ~ 2 mm/sec to ~ 30 cm/sec over this distance.
- Maximum strain, $s^2 \sim \mathcal{O}(10^4)$ ($1/sec^2$) appears to exist from ~ 2 mm in front of the orifice from which one can predict the probable breakage locations.
- From the eigen vector map of the rate of strain tensor we see that, uniaxial straining exists before the orifice and beyond the orifice close to the channel wall simple shear dominates.
- Detected breakage locations suggest that most of the aggregates break in front of the orifice where the strain is maximum.
- By measuring the ratio of the intermediate eigen value, which we found compressive in nature, to the most compressive eigen value of the rate of strain tensor we found that the majority of the breakup events takes place due to axisymmetric straining.
- By measuring the initial size of the aggregates and the strain rate responsible for the breakage, we come up with a nice agreement with the well known power law scaling.

3.4 Flow field analysis : Homogeneous quasi isotropic turbulence

In this section we present the core idea of how the coarse grained velocity gradient tensor $\frac{\partial \bar{u}_i}{\partial x_j}$ is computed. We explain the necessary statistical checks and verifications of the measured data using kinematic relations. Then we show some important properties of $\frac{\partial \bar{u}_i}{\partial x_j}$ that will establish the validity of the coarse grained measurement of a random velocity field. We end this section by characterizing the flow employed to break the aggregates.

Fig. 3.25 gives a qualitative impression of the trajectories which are $\sim 9\eta$ long, i.e., they are tracked over 0.8 seconds. The trajectories are encoded with the Lagrangian acceleration. The probability distribution of the lengths of the those Lagrangian trajectories shows an exponential decay (see Fig. 3.26). The statistics include all the trajectories, a portion of which is shorter than the Kolmogorov length η contributing to the lower value of the mean trajectory length and the mean trajectory length is i.e., $\langle l_t \rangle \sim 2\eta$.

The structure of the quasi homogeneous isotropic turbulent flow is investigated by studying the coarse grained velocity gradient tensor $\frac{\partial \bar{u}_i}{\partial x_j}$ which is computed by differentiating the convoluted velocity field using the approximation of Lüthi et al. [73].

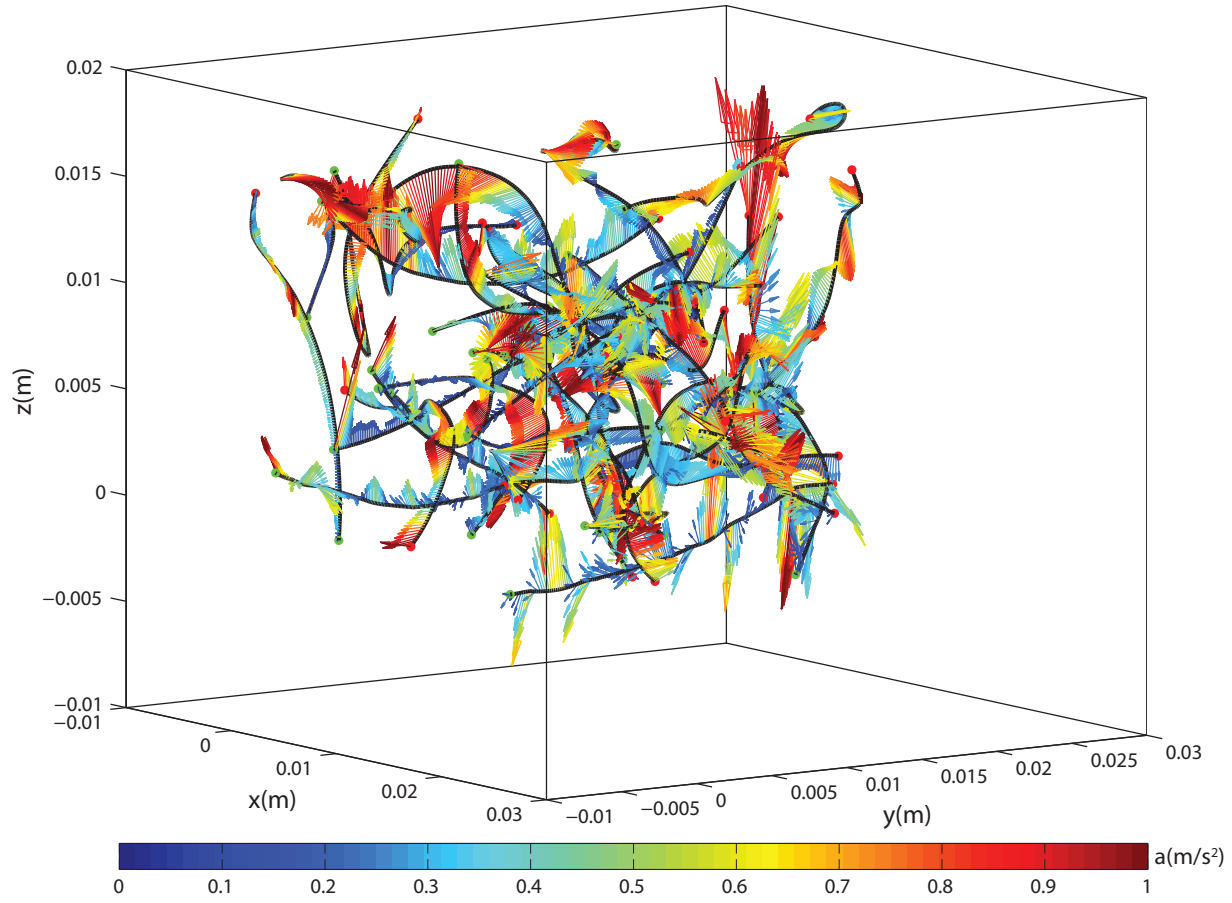


Figure 3.25: Trajectories in homogeneous isotropic turbulence at $Re_\lambda = 90$. The selected trajectories which are $\sim 9\eta$ long are color coded by the acceleration and tracked over ~ 0.8 sec.

$$\tilde{A}_{ij}(\mathbf{x}) \approx \frac{20}{(n-1)\Delta^2} \sum_{x' \in B_\Delta(x)} \left(u_i(\mathbf{x}') - \frac{1}{n} \sum_{x'' \in B_\Delta(x)} u_i(\mathbf{x}'') \right) \quad (3.7)$$

A random velocity field $\mathbf{u}(\mathbf{x})$ is convoluted by using a *blurring filter* ρ_Δ which is continuous like a Gaussian filter and has compact support like a top-hat filter (see e.g., [73]) to the coarse grained velocity field $\tilde{\mathbf{u}}(\mathbf{x})$ as

$$\tilde{\mathbf{u}}(\mathbf{x}) = \int d^3\mathbf{x}' \rho_\Delta(\mathbf{x} - \mathbf{x}') \mathbf{u}(\mathbf{x}') \quad (3.8)$$

In equation (3.7), Δ defines the filtering scale for the convolution. For homogeneous isotropic turbulence, B_Δ is essentially a sphere and n refers to the number of available data points contained within B_Δ centered at \mathbf{x} . 3D-PTV measures the velocity at those n seeding particles and not over the volume B_Δ . Therefore the integral \int in equation (3.8) is approximated by the summation \sum to estimate the coarse grained $\tilde{\mathbf{u}}(\mathbf{x})$. This introduces an error in evaluating the velocity derivative tensor $\tilde{A}_{ij}(\mathbf{x})$.

Lüthi et al. [73] removed the trace of \tilde{A}_{ij} as it leads to the best estimate of $\tilde{A}_{ij}(\mathbf{x})$.

$$\frac{\partial \tilde{u}_i}{\partial x_j} = \tilde{A}_{ij} - \gamma \delta_{ij} \tilde{A}_{kk} \quad (3.9)$$

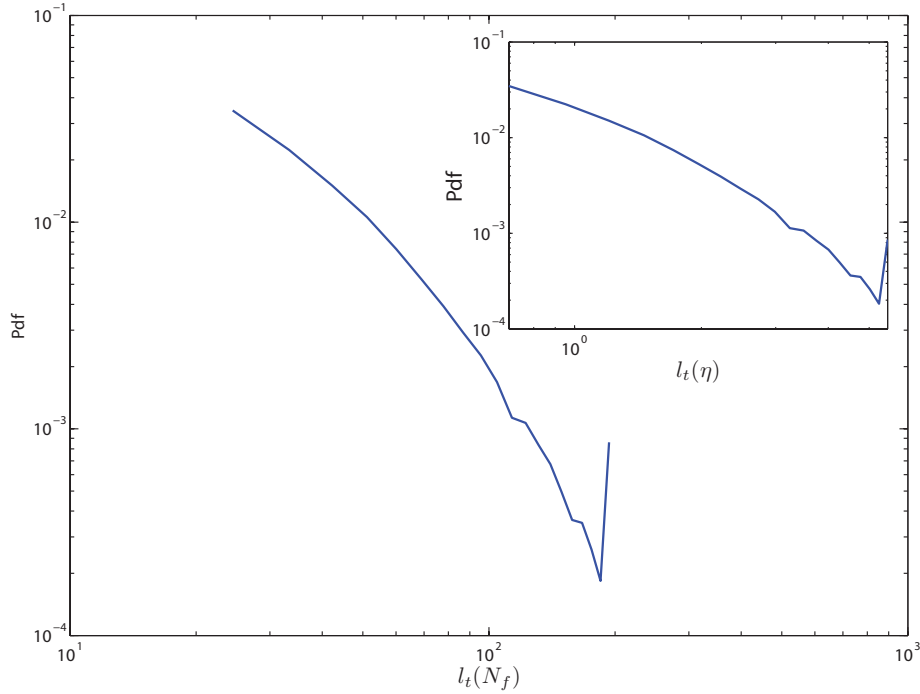


Figure 3.26: Pdf of the length of the trajectories measured in number of frames they are tracked by 3D-PTV, i.e., their temporal longevity and in Kolmogorov length scale η (inset) showing an exponential decay in probability of finding longer tracks.

This central estimate for $\frac{\partial \tilde{u}_i}{\partial x_j}$ has a minimal variance with $\gamma = \frac{1}{3}$. Equations (3.7) and (3.9) are the governing equations to derive coarse grained velocity derivatives, $\frac{\partial \tilde{u}_i}{\partial x_j}$ with $\gamma = \frac{1}{3}$ filtered at scale Δ . The integral accuracy strongly depends on the number of data points, n , within Δ_B which in turn dictates the filtering scale Δ . The lower bound of n is a function of the tracer concentration used in the experiment. Lüthi et al. [73] reported that $n \sim 12$ is the lower working limit for $\frac{\partial \tilde{u}_i}{\partial x_j}$.

Fig. 3.27 (left) shows the probability density of the number of data points contributing to the $\frac{\partial \tilde{u}_i}{\partial x_j}$ around the trajectories of the aggregates. By meeting the practical lower limit of $n \sim 12$, we have the filtering scale $\Delta = 20\eta$. We check the accuracy of the 3D-PTV measurement by looking at two particular kinematic quantities namely divergence of the velocity, i.e., $\nabla \cdot \mathbf{u}$ and the Lagrangian acceleration $\frac{Du_i}{Dt}$. Due to the incompressibility of the working fluid, i.e., water, $Tr[\frac{\partial \tilde{u}_i}{\partial x_j}]$ should be zero at all the measured data points in the ideal case. But in practice measurements are not entirely free of noise and hence $Tr[\frac{\partial \tilde{u}_i}{\partial x_j}] \neq 0$. We exploit this fact to construct the joint distribution among components of the spatial velocity derivative by writing $\nabla \cdot \mathbf{u} = 0$:

$$\frac{\partial u_i}{\partial x_i} = - \left(\frac{\partial u_j}{\partial x_j} + \frac{\partial u_k}{\partial x_k} \right) \quad (3.10)$$

Fig. 3.28 shows the joint pdf of equation (3.10). The distribution of the components of the $Tr[\frac{\partial \tilde{u}_i}{\partial x_j}]$ lie around the diagonal but not strictly along the diagonal which reflects the fact that the correlation coefficients indeed deviate from the ideal value of 1. We found the correlation coefficient for all the components to be ~ 0.9 . As the next check, we use the kinematic expression for the Lagrangian acceleration where we split the derivative into its local and convective parts as

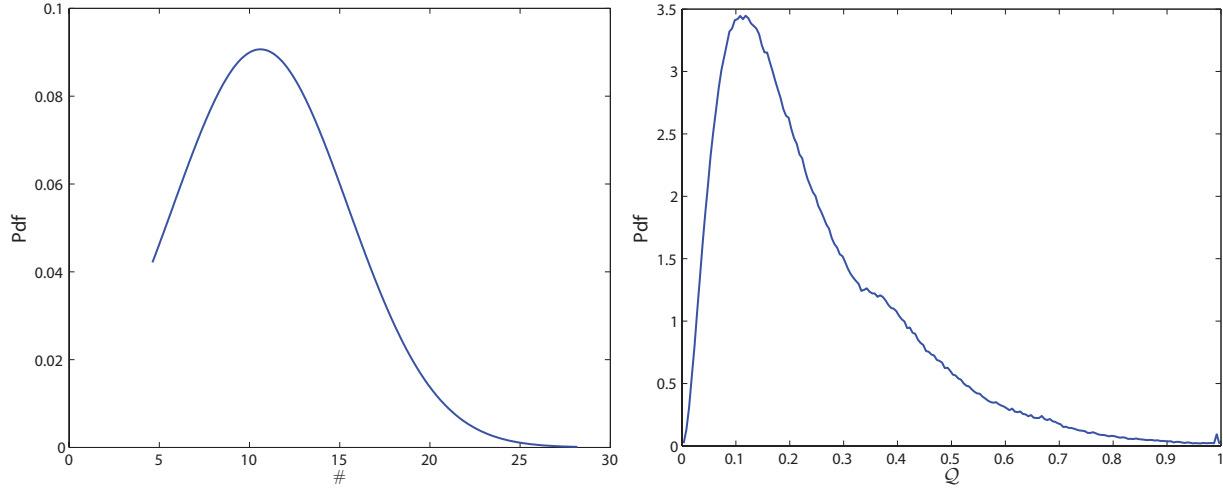


Figure 3.27: Pdf showing the number of data points within B_Δ used for calculating the spatial velocity gradient $\frac{\partial u_i}{\partial x_j}$ (left). Pdf of the quality error (right) Q , which is the weighted sum of the relative divergence and acceleration error revealing that $> 80\%$ of the measured data points stay below ~ 0.25 error margin

$$\frac{D\mathbf{u}_i}{Dt} = \frac{\partial u_i}{\partial t} + u_j \frac{\partial u_i}{\partial x_j} \quad (3.11)$$

3D-PTV is capable of measuring the Lagrangian acceleration $a_i = \frac{Du_i}{Dt}$ as a whole following an arbitrary trajectory but its constituent parts, i.e., the local acceleration, $a_{l,i} = \frac{\partial u_i}{\partial t}$ and the convective acceleration $a_{c,i} = u_j \frac{\partial u_i}{\partial x_j}$ involve the discrete information from the surrounding particles. This makes all the three quantities in the equation (3.11) independent from each other. Therefore, equation (3.11) provides a more robust check for the accuracy of the measurement. Fig. 3.29 shows the joint probability distribution for each component of the Lagrangian acceleration with the subsequent summation of the other two. Like the velocity distribution, the acceleration distribution also lies around the diagonal with correlation coefficients for all the components of ~ 0.87 .

Combination of the above mentioned checks defines another criterion called quality. In principal, quality is the weighted sum of the relative divergence of the velocity gradient and acceleration which we formulate as

$$Q = 0.01 \frac{|\frac{\partial u_1}{\partial x_1} + \frac{\partial u_2}{\partial x_2} + \frac{\partial u_3}{\partial x_3}|}{|\frac{\partial u_1}{\partial x_1}| + |\frac{\partial u_2}{\partial x_2}| + |\frac{\partial u_3}{\partial x_3}|} + 0.99 \frac{1}{3} \sum_{i=3}^3 \frac{|a_i - a_{l,i} - a_{c,i}|}{|a_i| + |a_{l,i}| + |a_{c,i}|} \quad (3.12)$$

The quality parameter Q is made completely biased towards the relative acceleration error by providing 99% weight, as we learned that terms containing the Lagrangian acceleration are independent from each other and give a rigorous estimates of the error. From equation (3.12) it is obvious that the lower the Q the higher is the accuracy of the measured quantity. Fig. 3.27 (left) shows the pdf of the quality from which we conclude that more than 80% of our measured data have quality error less than 0.25 and than $\langle Q \rangle \sim 0.12$. A detailed account of the procedure for determining the accuracy of the 3D-PTV measurements and related verifications are given by Luthi et al. [74].

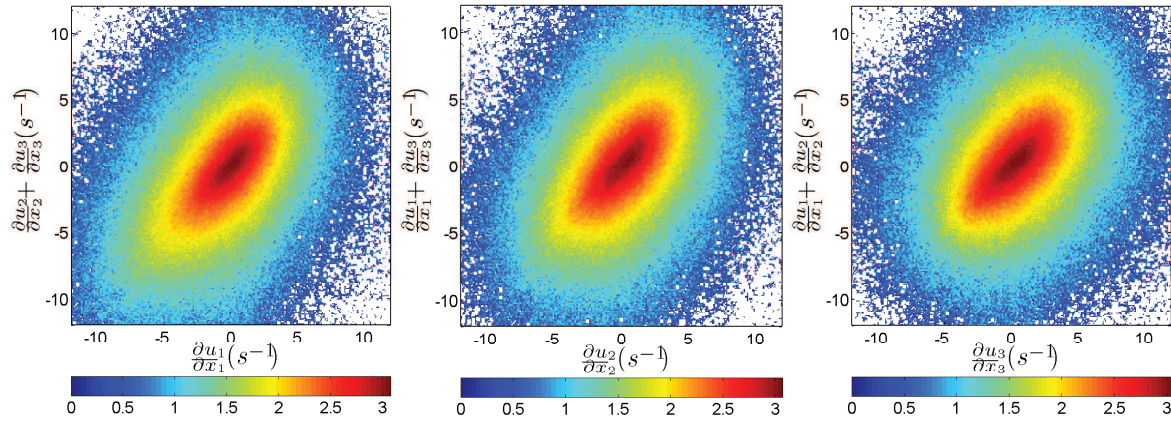


Figure 3.28: The joint pdf of each component of the kinematic relation $\frac{\partial u_i}{\partial x_i} = \frac{\partial u_j}{\partial x_j} + \frac{\partial u_k}{\partial x_k}$ (no \sum over the index i, j, k).

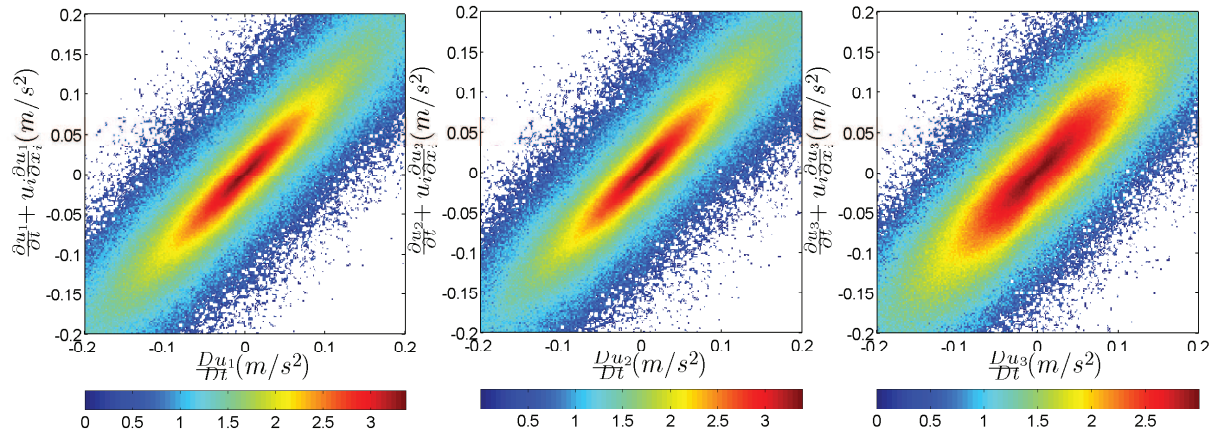


Figure 3.29: The joint pdf of each component of the kinematic relation $\frac{\partial u_i}{\partial t} = \frac{\partial u_i}{\partial t} + u_j \frac{\partial u_i}{\partial x_j}$.

After the systematic statistical checks on the measured data we investigate the behavior of the coarse grained velocity gradient $\frac{\partial \tilde{u}_i}{\partial x_j}$ by looking at several canonical characteristics of the turbulent flow. One of the prominent features in turbulent flow is self amplification. The most important underlying features of the self-amplifying dynamics of the velocity gradients are illustrated in Fig. 3.31. We look into the “structure“ of the symmetric part of the $\frac{\partial \tilde{u}_i}{\partial x_j}$, i.e., s_{ij} through the ratio between the intermediate eigen value Λ_2 and the most compressive one Λ_3 , $\frac{\Lambda_2}{\Lambda_3}$. It has been established by now that in the dissipative range, $\frac{\Lambda_2}{\Lambda_3} \approx 0.14$ for a vast range of Re_λ . (see, e.g., [56, 124, 17]). Borue et al. [18] and Bos et al. [29] reported $\langle \Lambda_2 \rangle > 0$ also in the equilibrium range. This is an obvious indication that, like the small scale gradient in the viscous range, the coarse grained velocity gradient $\frac{\partial \tilde{u}_i}{\partial x_j}$ also experiences self amplification in the inertial range. By measuring the ratio of $\frac{\Lambda_2}{\Lambda_3}$ from 3D-PTV data, we found an excellent agreement as $\frac{\Lambda_2}{\Lambda_3} \approx 0.135$ (see Fig. 3.31 (right)).

In Fig. 3.31 (left) the pdf of the measured alignment between vorticity, ω and the so-called vorticity stretching vector, $W = \omega_i s_{ij}$ along with its positive mean value (black vertical line) are shown. The positiveness of the invariant $\cos(\omega, W)$ explains the occurrence of the vortex stretching when the projection

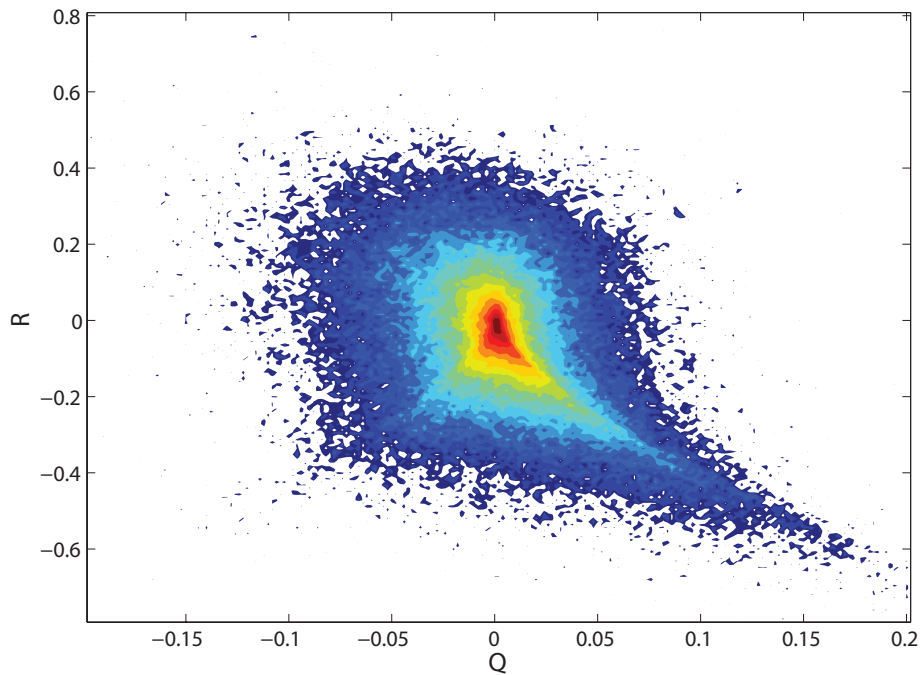


Figure 3.30: Qualitative universal feature of turbulent flow, the joint Pdf of the second and third invariant of the coarse grained velocity gradient $\frac{\partial \bar{u}_i}{\partial x_j}$, Q and R respectively showing the typical tear drop shape.

of the stretching vector, W points to the same direction as of the vorticity vector ω . A strong alignment of W with ω as seen in Fig. 3.31 (left) illustrates the positive mean enstrophy production in support of the strong consensus of the prevalence of the vortex stretching over compression, a characteristic feature in turbulent flow.

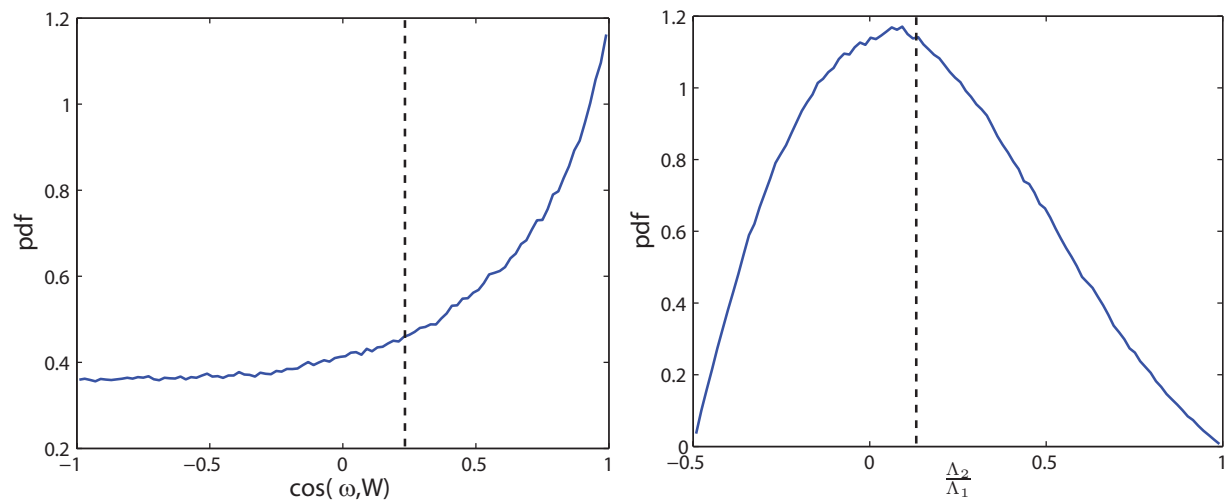


Figure 3.31: Reflection of the self-amplification nature of turbulence; (left) Pdf of the cosine between vorticity ω and the vorticity stretching vector $W = \omega_j s_{ij}$. (right) Pdf of the shape of the coarse grained rate of strain tensor s_{ij} . Vertical dashed lines indicate the respective mean values.

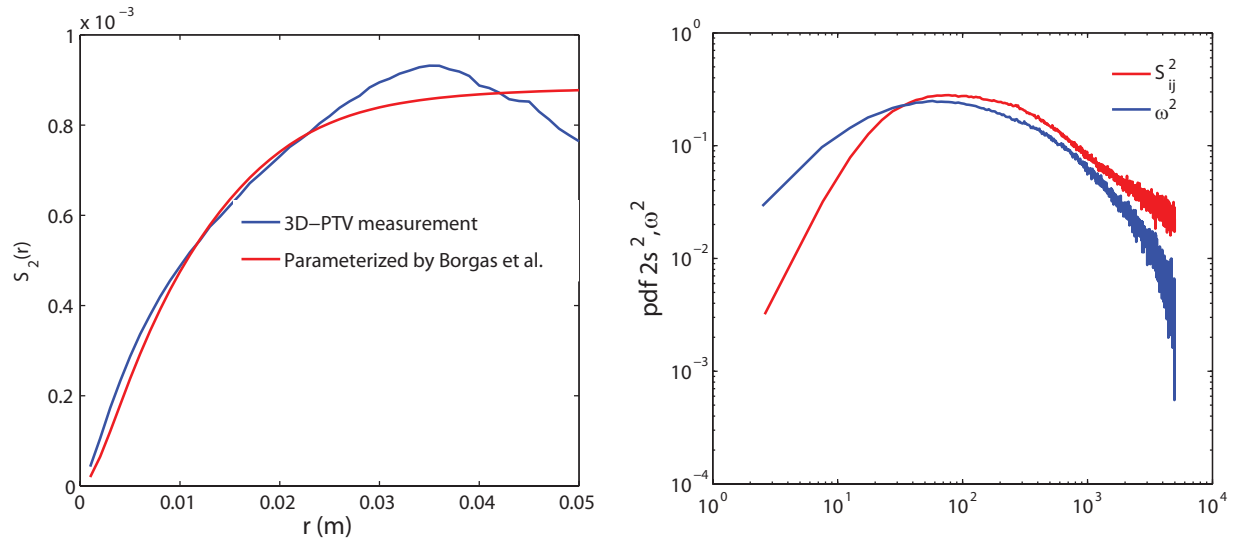


Figure 3.32: Eulerian second order longitudinal velocity structure function $S_2(r)$ measured by 3D-PTV is compared with the parameterized expression derived by Borgas et al. (left). (right) Pdf of the first moment of the coarse grained \tilde{s}_{ij} and $\tilde{\omega}^2$ measured by 3D-PTV.

For turbulent flow characterization it has proven useful to study the so called Q-R plane (e.g. [26]). Q is the second invariant, $Q = \frac{1}{4}(2\omega^2 - 2s^2)$, of the velocity gradient tensor A_{ij} and R is its third invariant, $R = -\frac{1}{3}s_{ij}s_{jk}s_{ki} - \frac{1}{4}\omega_i\omega_j s_{ij}$. In joint pdf plots of Q versus R a qualitatively identical “teardrop” shape (see Fig. 3.30 (left)) for different kinds of turbulent flows was found by a number of investigators. Chacin et al. [27] argue that the shape is a universal characteristic of the small-scale motions of turbulence. Recently, very similar dynamics have also been observed for the coarse grained velocity gradients, see e.g. Luthi et al. [73].

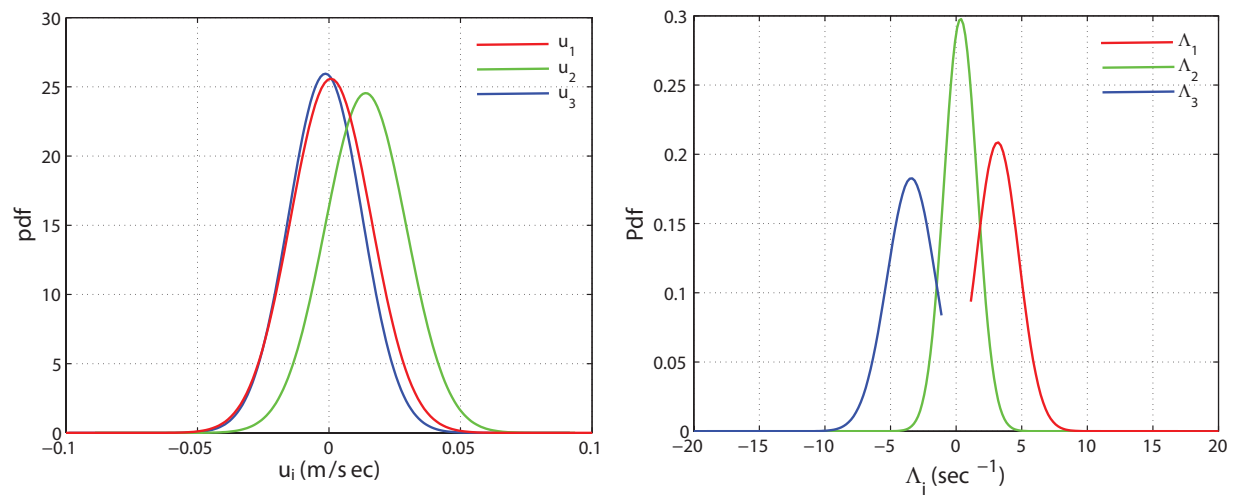


Figure 3.33: Pdfs of the instantaneous velocity components showing that the flow is not exactly isotropic as they do not collapse on to each other (left). Probability distributions of the eigen values of the rate of strain tensor \tilde{s}_{ij} supports the previous finding that $\langle \tilde{\Lambda}_2 \rangle > 0$

Based on the data passing the robust accuracy checks and knowing the behavior of the coarse grained velocity gradient $\frac{\partial u_i}{\partial x_j}$ exhibits the typical turbulent flow character, of the flow field which will be used for the aggregate breakup. The observation volume for the experiment was $(\sim 100\eta)^3$. From Fig. 3.33 we found that the flow is not exactly isotropic as the probability distribution of one velocity component, u_2 , does not merge with the other two components as they collapse on to each other. The PDF of the eigen values Λ_i of the rate of strain tensor \tilde{s}_{ij} shows consistency particularly with the fact discussed above that $\langle \tilde{\Lambda}_2 \rangle > 0$.

The PTV velocity gradient measurements were performed on a scale of $\Delta = 5.5$ mm. The integral scale, \mathcal{L} and the mean rate of dissipation $\langle \epsilon \rangle$, were obtained by fitting the parametrization of [17] (see equation (3.13)) to the measured longitudinal second order velocity structure function $S_2(x) = \langle (\delta v_r)^2 \rangle = \langle (u_\perp(\mathbf{x} + \mathbf{r}) - u_\perp(\mathbf{x}))^2 \rangle$.

$$S_2(r) = 2 \left(1 - \exp \left(- \frac{r}{(15C_k)^{\frac{2}{3}} \eta} \right) \right)^{\frac{4}{3}} \cdot (\epsilon \mathcal{L})^{\frac{2}{3}} \left(\frac{r^4}{\frac{64\mathcal{L}^4}{C_k^6} + r^4} \right)^{\frac{1}{6}} \quad (3.13)$$

From Fig. 3.32 we observe that, the measured scaling between the velocity increment and separation distance follows considerably well the parameterized scaling by Borgas et al. [17]. Luthi et al. [73] derived an analytical formulation to compute the magnitude of the coarse grained s^2 and $\tilde{\omega}^2$ as functions of Δ and $S_2(x)$ as

$$2\langle \tilde{s}^2 \rangle = \langle \tilde{\omega}^2 \rangle = \int_0^\Delta S_2(x) \frac{1800}{\Delta^2} \left(\frac{x}{\Delta} \right)^3 \left(1 - 2 \left(\frac{x}{\Delta} \right)^2 \right) \left(\left(\frac{x}{\Delta} \right)^2 - 1 \right) \frac{dx}{\Delta} \quad (3.14)$$

Here in equation (3.14), S_2 is the Eulerian second order longitudinal velocity structure function which is parameterized by Borgas et al. [17] (see equation (3.13)) as a function of the fluid particle separation r , kinematic viscosity of the fluid ν , energy injection scale of the flow \mathcal{L} , energy dissipation rate ϵ and Kolmogorov constant C_k . Using equation (3.14), the coarse grained mean strain $\langle 2\tilde{s}^2 \rangle$ is estimated to be about 58 sec^{-2} . The Pdfs of the s^2 and ω^2 measured by 3D-PTV and their respective means are shown in Fig. 3.30 (right). We found an excellent agreement between the measured strain from 3D-PTV and the analytical estimate from Luthi et al. [73].

In table 3.1, we present the characteristic flow properties measured by 3D-PTV.

u_{rms}	\mathcal{L}	τ_η	ϵ	Re_λ	η	G	λ	δr_p	$\frac{N_f}{\tau_\eta}$	res.	V
$\left(\frac{m}{sec}\right)$	(mm)	(sec)	$\left(\frac{m^2}{sec^3}\right)$	$(-)$	(mm)	$\left(\frac{1}{sec}\right)$	(m)	(η)	$\left(\frac{frame}{\tau_\eta}\right)$	(η)	(η^3)
0.016	25.12	0.052	3.7×10^{-4}	90	0.228	19	3.3×10^{-3}	10η	13	8η	$(100\eta)^3$

Table 3.1: Flow properties of the turbulent flow

3.5 Breakage analysis in turbulence

3.5.1 Example analysis

We have recorded $\mathcal{O}(100)$ breakage events and for the sake of simplicity limited our choice to a binary breakage pattern, i.e., one aggregate breaks into two parts, for the analysis. Before analyzing the whole set of the breakage events, we randomly select a few single events as prototype examples and investigate the role of the relevant flow dynamics along their Lagrangian trajectories. This intention of the single event analysis is to provide the necessary means on how the rest of the events should be systematically addressed in the remaining part. Fig. 3.34 shows the trajectories of an aggregate breakage (large white patch on the image) as viewed from four cameras in the turbulent flow seeded with tracer particles (white dots). The release point of the parent particle is on the extreme right of every image. Images from the third and fourth camera (in Fig. 3.34, bottom right and left respectively) partly show the aggregate at the time of breakage and the "daughter" fragments which are produced there (shorter separate track). This particular aggregate is tracked over $\sim 20\tau_\eta$ before and after the breakage and $\sim 2\tau_\eta$ beyond its breakage. Fig. 3.35 shows how an aggregate of the size of about 1 mm breaks into almost two equal parts. The aggregate flows from the left to right in the figure.

First we take a look at the evolution of the magnitudes of the components of the velocity gradient tensor, $\frac{\partial u_i}{\partial x_j}$, i.e., strain s^2 and enstrophy ω^2 along the Lagrangian trajectory of the parent. Here we coined the terms "parent" and "children" to essentially indicate the aggregate trajectory until breakage and onwards as well as the fragment respectively. As revealed from the Fig. 3.37 (left), where we show strain along the aggregate trajectory, the selected aggregate experienced the maximum s^2 after $\sim 2\tau_\eta$ after it was introduced into the flow and broken after $\sim 20\tau_\eta$ at s^2 , where $s_b^2 \approx \frac{1}{5}s_{max}^2$. The notation s_b^2 means the strain at breakage. We notice that during the time between s_{max}^2 and s_b^2 there exists a monotonic decrease in the intensity of s^2 up to $\sim 5\tau_\eta$ before the breakage moment and the aggregate goes to pieces shortly after it begins to ascend towards another relative maximum of s^2 , although if not necessarily lies at the inflection point of s^2 .

Our preliminary deduction by looking at the time evolution of s^2 is twofold. First, $s_b^2 \leq s_{max}^2$, i.e., an aggregate can be broken at a strain lower than the maximum strain it experiences any time before the breakup. The second one is the consequence of the first deduction namely the aggregates need to be exposed sufficiently long time to the fluctuating s^2 dynamics. That means an aggregate which can sustain s_{max}^2 exerted on it requires a cumulative s^2 effect, i.e., $\int s^2$ to eventually break. When we analyzed this breakup event in the eigen frame of the rate of strain tensor, we find that Λ_1 , the most extensional eigen value and hence responsible for the stretching, along the trajectories in Fig. 3.39 is slightly larger at the time of breakage than before. The ratio $|\frac{\Lambda_2}{\Lambda_3}|$ along the trajectory of breakage refers to the influence of compressive eigen vector on breakup. In the Fig. 3.39 (right) $|\frac{\Lambda_2}{\Lambda_3}|$ along the parent trajectory exhibits strong variations over a range of $-0.05 < \frac{\Lambda_2}{\Lambda_3} < -0.5$ and reaches $\frac{\Lambda_2}{\Lambda_3} \simeq \frac{1}{2}$ shortly before the breakup. Due to this variations in compressive eigen values of the strain, aggregates experience both uniaxial straining and compression in the $\lambda_2 - \lambda_3$ plane.

That sets up an intriguing question of why and how an aggregate survives s_{max}^2 but breaks apart at relatively lower s^2 . We qualitatively attribute the resilient character of an aggregate to s_{max}^2 to the internal mechanical architecture, i.e., strength of an aggregate and ability to adjust the inner structure. Although 3D-PTV is incapable to probe into the internal structure of the aggregate and therefore the response and rupture of the bonds making up the morphology, we observed quite a visible deformation during the

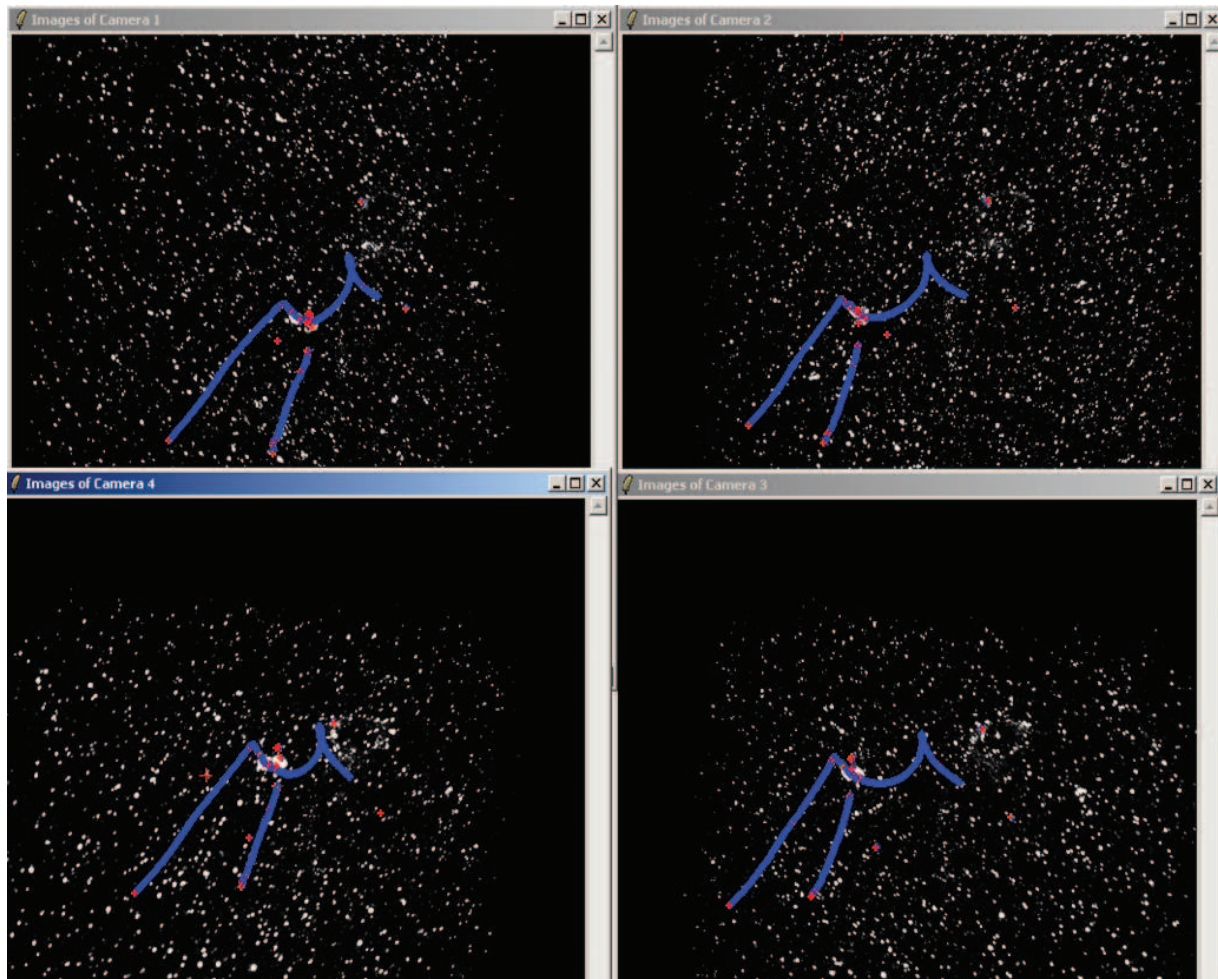


Figure 3.34: Trajectories (in blue) from a breakage event as seen by four cameras. The longer trajectory represents the parent track and the relatively shorter one is the fragment track within the flow field seeded with tracer particles.

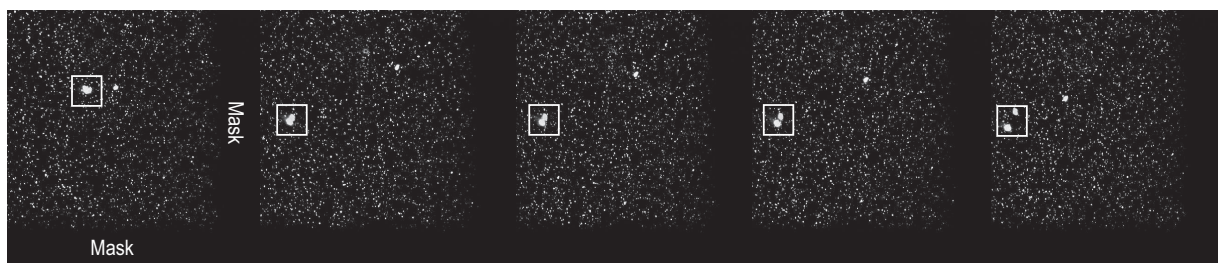


Figure 3.35: An arbitrary breakage event is shown from one camera view in four different time instances. The flow direction is from the left to right. The size of the aggregate is approximately 1 mm that breaks into almost two equal parts after the breakup.

course of the breakage. To illustrate this more clearly we picked up another breakage event where the aggregate exhibits a pronounced structural deformation. Fig. 3.36 illustrates how an aggregate initially looked like a uniform blob (far left) became straightened up almost like a thread like shape (third sequence from the left) and finally disintegrated. From this phenomenon we infer that the aggregates we introduced into the homogeneous quasi isotropic turbulent flow do not preserve their shape and structure but due to their flexibility they can react to the flow by rearranging the internal structure and survive the intensity of s_{max}^2 . Their deformation over the observation time of $\sim 20\tau_\eta$, s^2 continuously acts with varying intensity to the moment when the aggregate can no longer resist to the stress and eventually breaks up.

ω^2 , the enstrophy, is responsible for the rotation of the aggregates relative to the strain eigen frame. Therefore, ω_b^2 makes an aggregate to experience strain along varying direction. Therefore, a low ω_b^2 , where ω_b^2 refers to the enstrophy at the time of breakage, within $[t_0 - \sim 5\tau_\eta]$ (see Fig. 3.37) allows s^2 to dominantly act on the aggregate rather than deflect it from the direction of s^2 . Here t_0 indicates the time at breakage.

3.5.2 Statistical analysis

Bringing along this conjecture, now we proceed to examine the effect of s^2 and ω^2 for the whole set of recorded breakage events. We found our observation completely phenomenological while studying s^2 and ω^2 along the Lagrangian trajectories for all of the breakup events in the sense that there exists no defining trend of the instantaneous s^2 or ω^2 at breakage responsible for the break up. Also the Lagrangian history of s^2 as well as ω^2 towards the breakage point is unique from event to event i.e., they fluctuate wildly without showing pattern and that is why instead of a single Lagrangian configuration of s^2 and ω^2 for the breakup, we categorize the events into three different sub groups on the basis of s^2 history.

In the first group we classify those breakage events that take place at $\frac{Ds^2}{Dt} > 0$. Irrespective of the global or local maxima of s^2 , denoted as $s_{max,g}^2$ or $s_{max,\ell}^2$ respectively, we found a set of events occurring while ascending the valley of $s_{max,g}^2$ or $s_{max,\ell}^2$ signal over different times starting from the time of injection into the flow. Fig. 3.40 shows such of these events. We found that the aggregates were not subjected to the high s^2 along the way to the breakup and $\omega^2 \leq s^2$. Around $[t_0 - 5\tau_\eta]$ when s^2 tends to attain a peak value of s^2 , enstrophy seems to be relatively dampened in most of the cases as ω^2 declines towards s_b^2

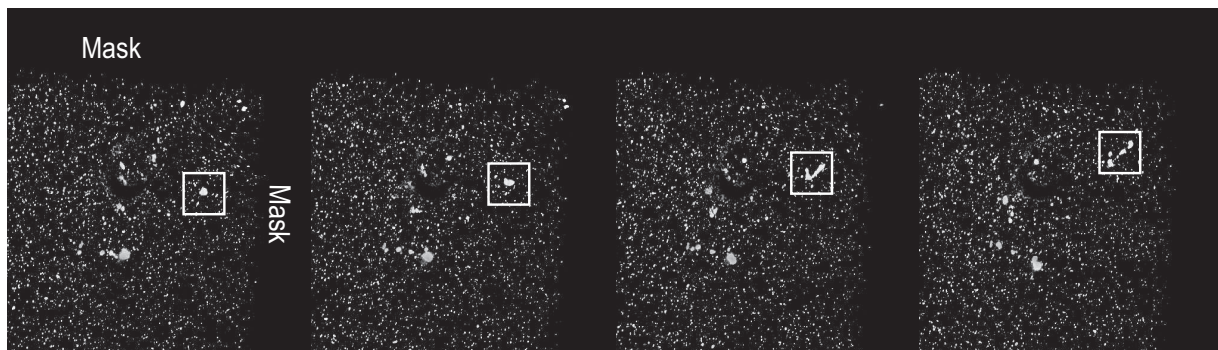


Figure 3.36: Deformation of an aggregate on the way to breakup captured in four different time instances. In this example an aggregate undergoes significant stretching seen in the third sequence from the left before it breaks apart into several pieces. This is illustrating of the fact that the aggregates posses elastic properties.

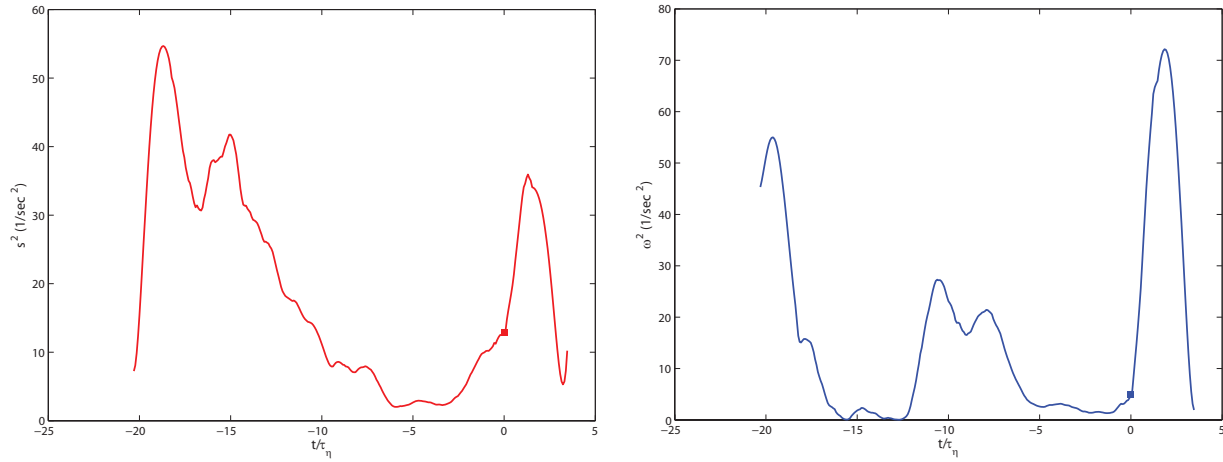


Figure 3.37: s^2 (left) and ω^2 (right) along the trajectories as a function of time normalized by Kolmogorov time scale τ_η . The time at which the aggregate breaks apart is pinned at 0 on the time axis.

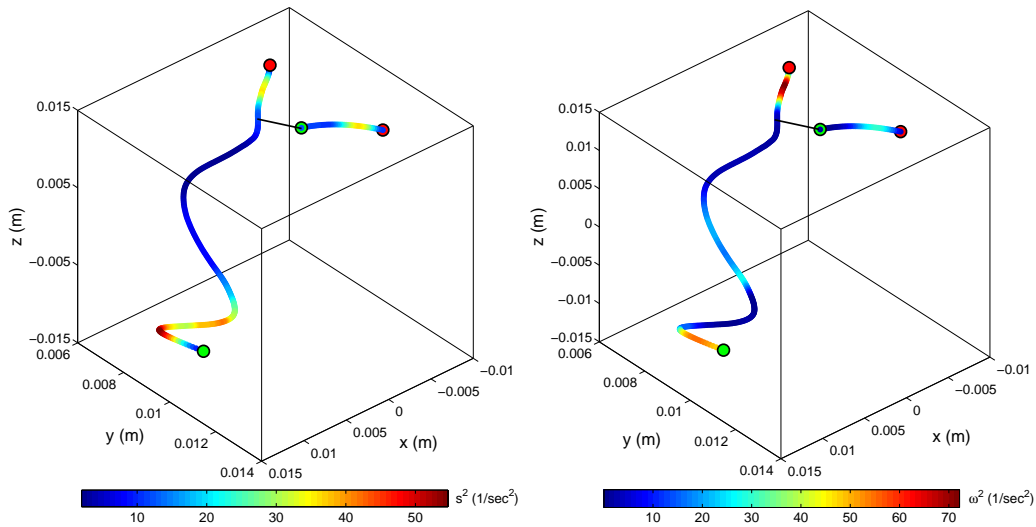


Figure 3.38: s^2 (left) and ω^2 (right) along the trajectory of the parent and fragment (shorter track) of an arbitrary breakage event. Green and red circles refer to the beginning and the end point of a trajectory respectively. The line from the beginning of the fragment track to the parent track refers to the separation vector, i.e., the direction along which the fragment has been separated at the time of breakage.

such that $\omega^2 \leq 10(1/sec^2)$. However, this class of breakup events does not show a unique s_b^2 but rather a range $s_b^2 \in [5, 40](1/sec^2)$.

In the second category we select the breakup events taking place when an aggregate can withstand $s_{max,g}^2$ and break during $\frac{Ds^2}{Dt} < 0$ that seems to be a relaxation phase.. We notice a marked difference between s_b^2 and ω_b^2 at the point of breakage (see Fig. 3.41). There are situations where the difference $[s_b^2 - \omega_b^2]$ is rather small but aggregates are exposed to either strong fluctuation of s^2 and ω^2 (see Fig. 3.42) or sometimes a smooth descent in s^2 and ω^2 towards breakup (see Fig. 3.43). We understand that

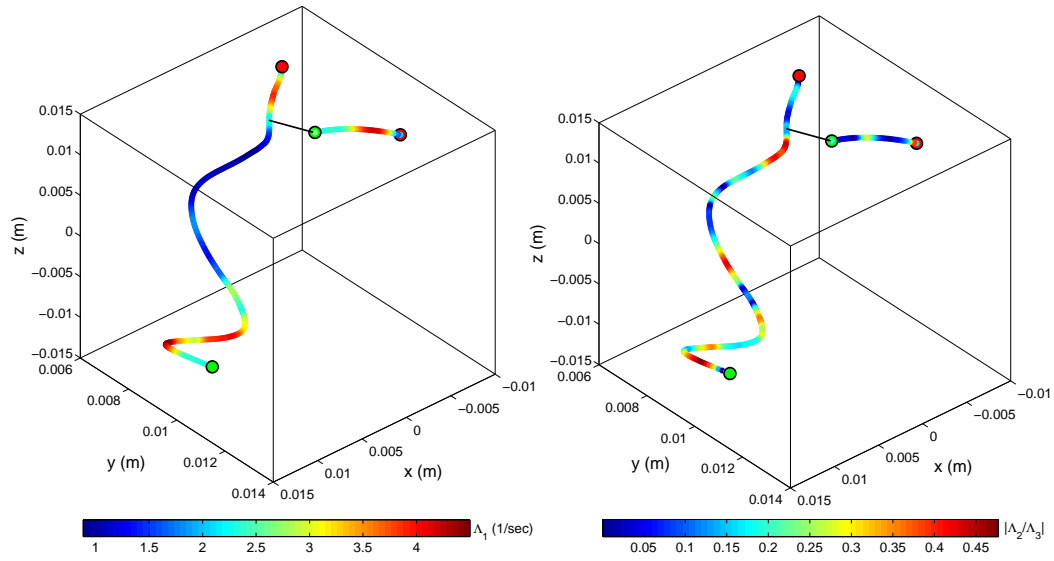


Figure 3.39: The most extensional eigen value Λ_1 of s^2 along the parent and children trajectory (left). In this particular example of the breakage event, the aggregate is subjected to higher stretching at the time of breakage. The ratio $|\frac{\Lambda_2}{\Lambda_3}| \simeq \frac{1}{2}$ (right) shortly before the breakage indicates that the aggregate also experienced compression along the plane of $\lambda_2 - \lambda_3$.

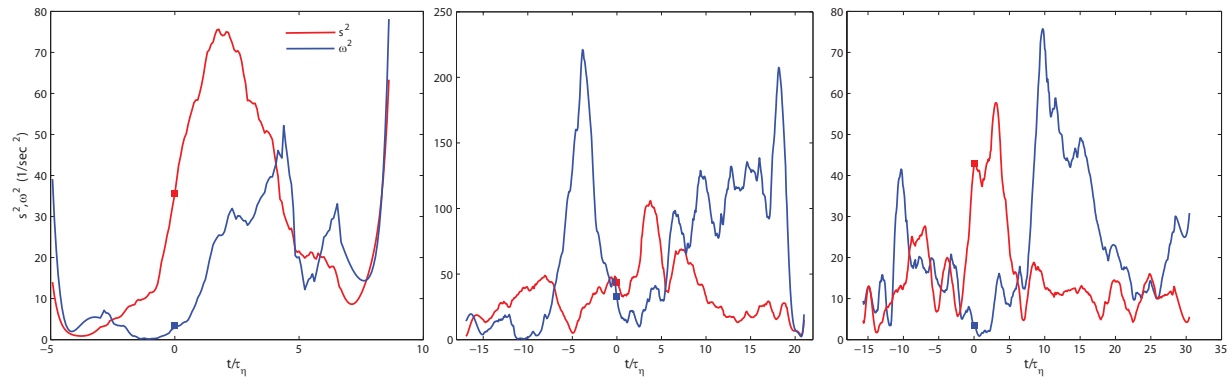


Figure 3.40: Three breakage events taking place at $s_b^2 \rightarrow s_{max,g}^2$ or $s_{max,\ell}^2$. This category of breakage is selected based on s_b^2 approaching to the peak value of the measured s^2 (red) together with the associated ω^2 (blue). The time when breakage takes place is pinned in 0 on the time axis normalized by Kolmogorov time scale τ_η .

an aggregate experiences s^2 over $\sim 15\tau_\eta$ on an average and experiences substantial damage during this time before the effect of ω^2 starts to act upon the aggregate. From Fig. 3.41, Fig. 3.42 and Fig. 3.43 we notice that for some breakage events $s^2 \geq \omega^2$ at the time of breakage. Enstrophy is believed not to be responsible for the breakage. By looking at time series of the strain and enstrophy together, we infer that higher ω^2 close to the time of breakage might induce torsional deformation in addition to strain driven structural damage.

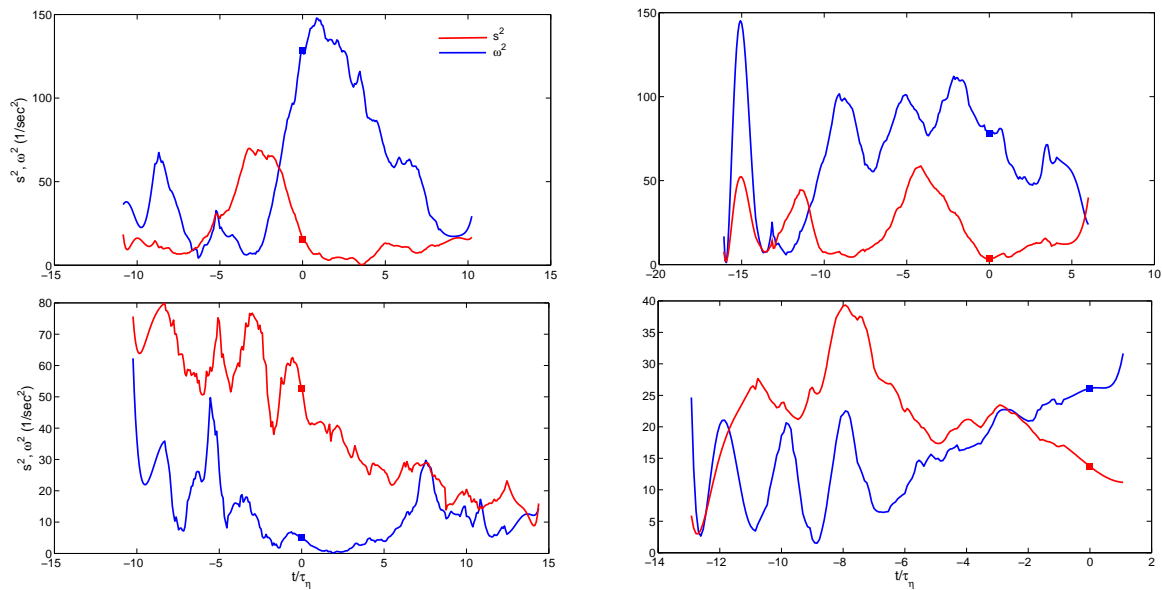


Figure 3.41: Few examples of breakage events where the local estimates of s^2 and ω^2 at the point of breakage differs by a large margin.

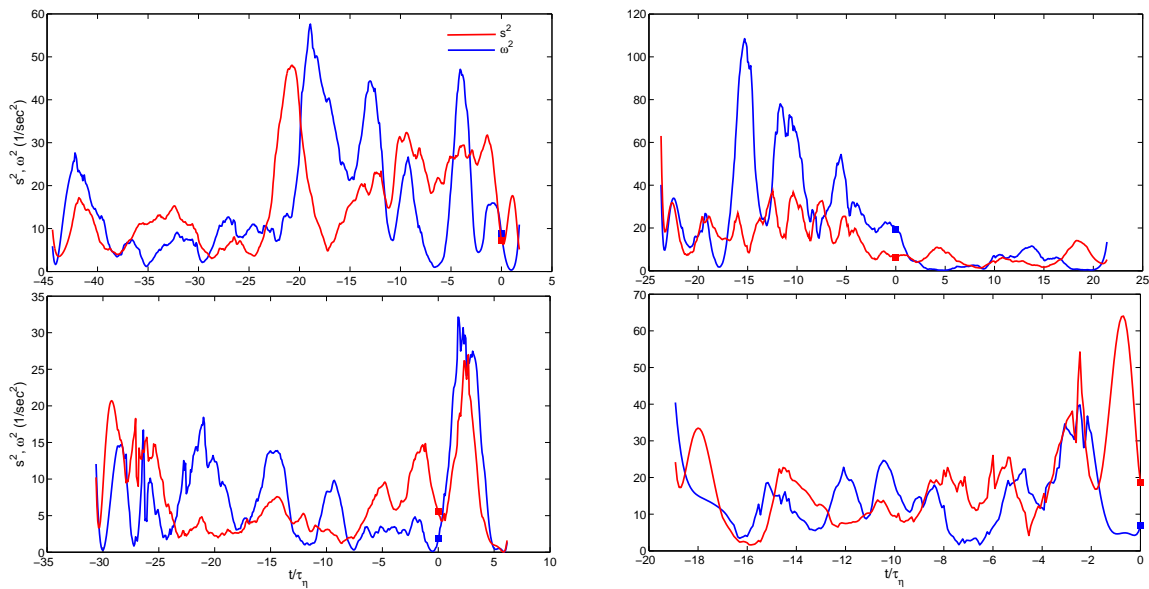


Figure 3.42: Breakage events where s^2 and ω^2 tend to equate each other at the breakage moment after surpassing their respective peak values. Prior to the breakage, the fluctuation frequency of s^2 and ω^2 are quite high.

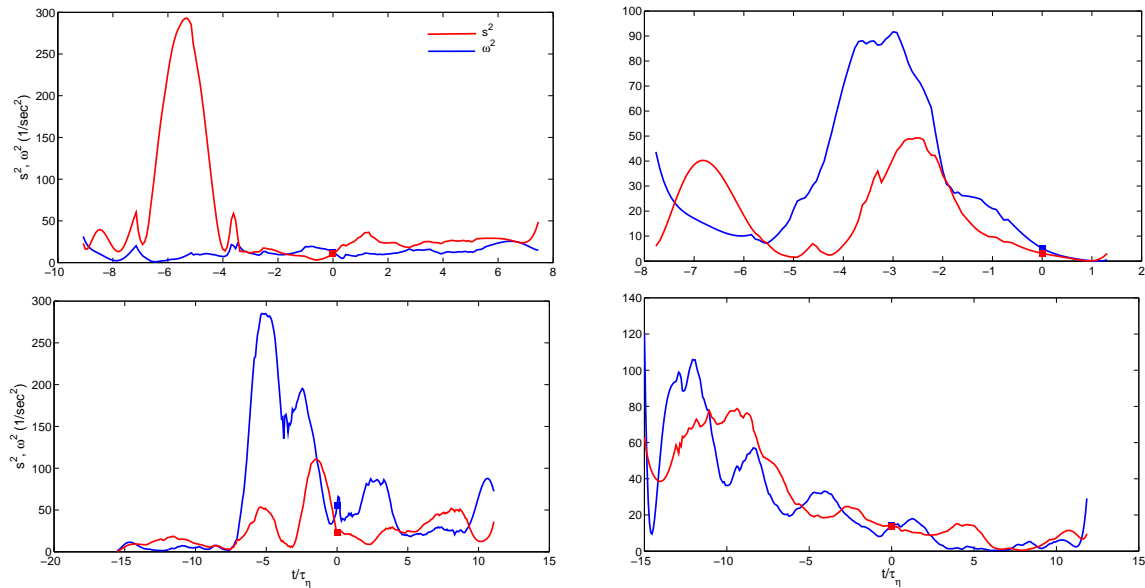


Figure 3.43: Aggregates survive the global maxima of s^2 and ω^2 where the evolution of s^2 and ω^2 are rather smooth and thereafter break at almost equally low s^2 and ω^2 .

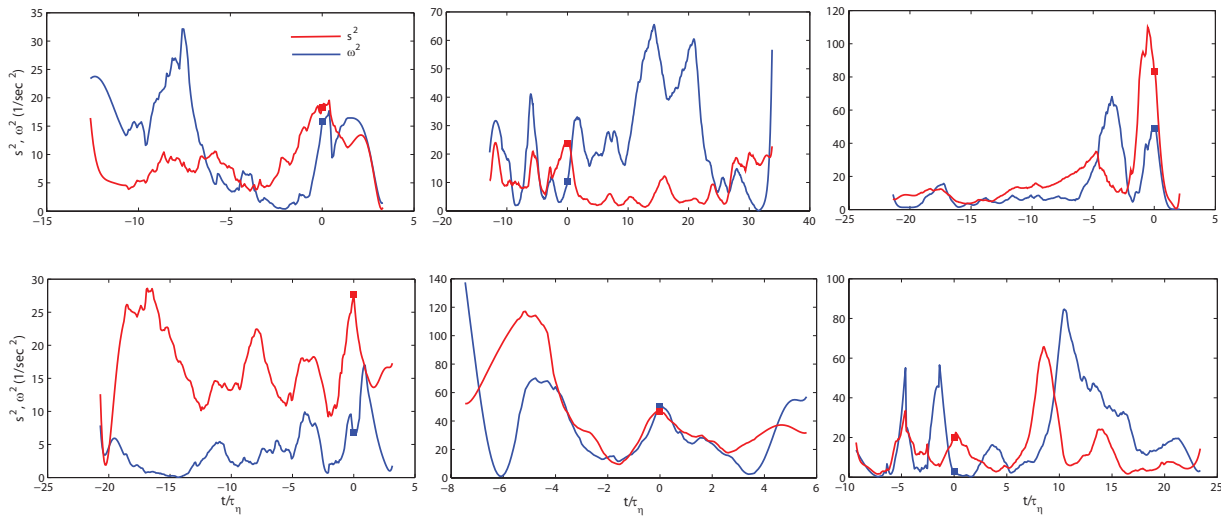


Figure 3.44: Breakup events taking place at a relative or absolute maxima of s^2 .

In the third category, we considered breakups occurring at $\frac{Ds^2}{Dt} \simeq 0$ (see Fig. 3.44). Again the behavior of ω^2 is quite inconclusive compared to s^2 evolution in the limit of break up point. Although at t_0 , s_b^2 attains a global or local maximum of s^2 , it takes approximately the same time for the aggregates to be broken, i.e., the average time scale is $\sim 15\tau_\eta$. Although the aggregates break up at $s_{max,g}^2$ or $s_{max,\ell}^2$, very often they survive a high intensity point in the s^2 signal before the breakage. Why and how an aggregate can endure higher s^2 than s_b^2 remains an open question. As a possible explanation we think of their mechanical inhomogeneity inside the aggregate may play an effective role, i.e., many bonds inside the aggregate structure are already broken while few are still holding out the aggregate. Addressing the axis

along which an aggregate undergoes breakage to be perpendicular to the initial separation vector, we project the rate of strain tensor along the separation vector, \mathbf{r} between the parent and the children. The motive is to investigate if s^2 persistently acts along the presumably weakest axis of the aggregate. We obtain $s_{rr} = \mathbf{r}s_{ij}\mathbf{r}^T$ where s_{rr} denotes the strain along \mathbf{r} .

After careful investigation for every breakage event we found the temporal evolution of s_{rr} is similar to that of s_{ij} for almost every cases of breakup. We consider the time evolution of s_{rr} taking the tilting of the particle into account but found no critical behavior. Fig. 3.45 shows a set of examples where strain in the direction of the axis of breakage, i.e., the axis along which the aggregate breaks into two parts, varies over time. This implies that the breakage axis may not always be the weakest axis inside the aggregate as it can sustain higher strain along that axis before breakage.

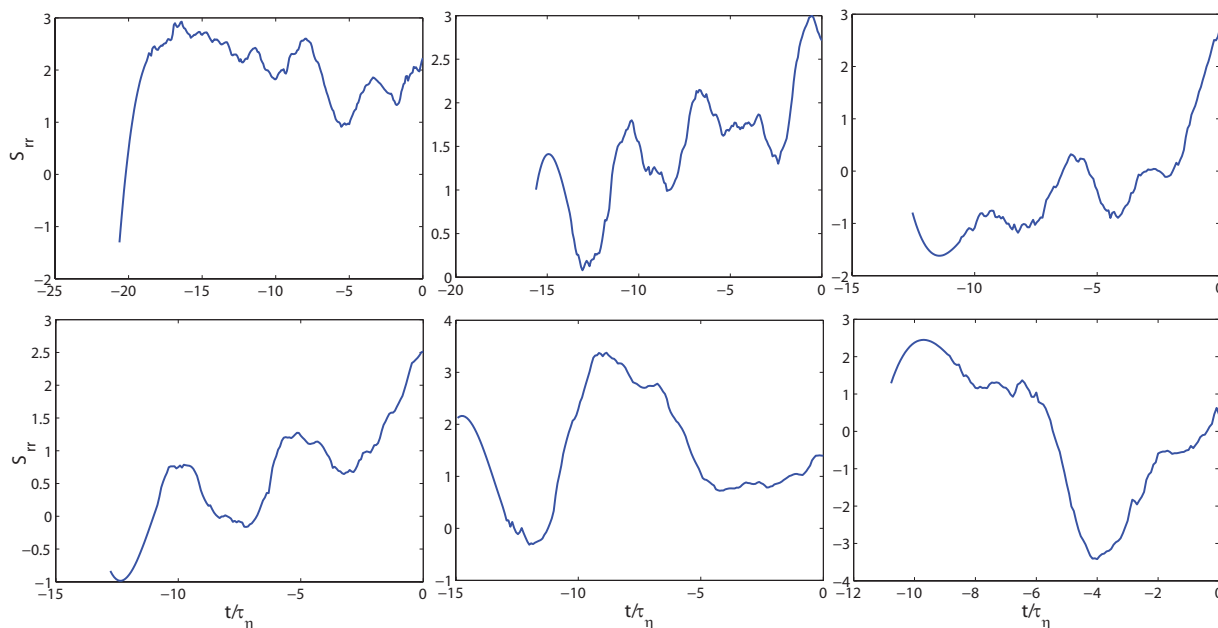


Figure 3.45: Orientation of the aggregate with respect to the separation vector \mathbf{r} , with the strain eigen frame λ_i of arbitrarily chosen breakage events.

3.5.3 Alignments with the principal strain and deformation

Since the Lagrangian history of s^2 and ω^2 clearly appears to be relevant for the breakage, in the following we investigate the orientation history of the aggregate with respect to the eigen frame of the rate of strain tensor.

It is interesting to investigate in which spatial direction a fragment gets detached from the original aggregate at the time it breaks. It would serve as an instantaneous measure of the locally predominant effect of the rate of strain tensor on breakup in the strain eigen frame. With that purpose we measure $\cos(\lambda_i, \mathbf{r})$, i.e., the alignment between the eigen frame of strain and the separation vector \mathbf{r} between the children and the parent. Fig. 3.46 illustrates how λ_1 (red) and λ_2 (green) orient themselves along the parent (blue) and children (yellow) trajectory and Fig. 3.47 shows the orientation of λ_3 , the most compressive eigen vector of strain of the particular breakup event illustrated in Fig. 3.35. In this breakup example we

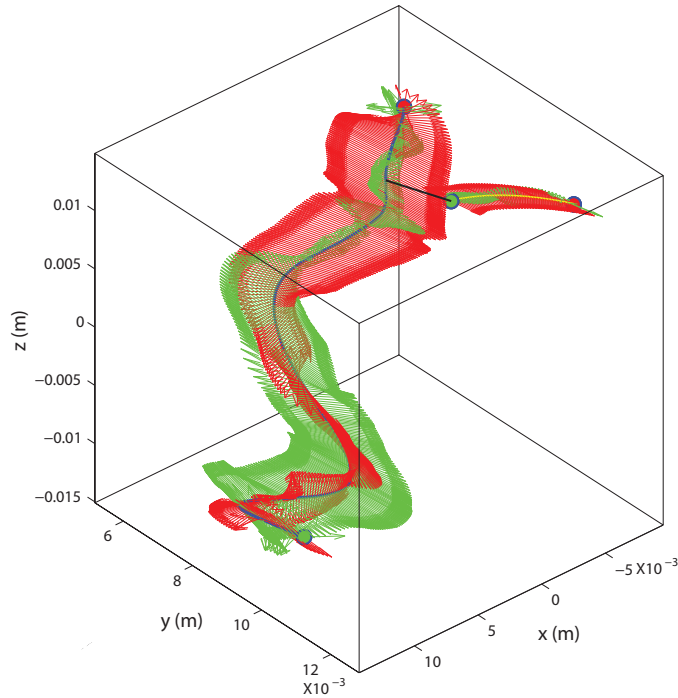


Figure 3.46: Mutual orientation of the most extensional (red) and intermediate eigen (green) vector of s_{ij} along the parent (blue) and children trajectory (yellow).

notice that the separation vector (black) is preferentially aligned with λ_1 (red), the most extensional eigen vector at the time of breakage. Since λ_i and \mathbf{r} are orthogonal to each other naturally $\mathbf{r} \perp \lambda_3$, which is visible from Fig. 3.47. This means the aggregate, as it breaks, is directionally guided towards the most stretching eigen direction.

We find that for all the breakage events two particles separate mostly in the direction of λ_1 , i.e., along the direction where the aggregates experience the largest stretching, which can be observed from the probability density function of the alignment $\cos(\mathbf{r}, \lambda_{1,2})$ at $t=0$ in Fig. 3.48. In order to know for how long the aggregates have been aligned with λ_1 , we track the aggregate back in time by projecting the separation vector \mathbf{r} onto the strain eigen frame λ_i . Fig. 3.49 shows the aggregate orientation in λ_i frame based on arbitrarily selected breakage events. It can be conjectured that although the direction in which an aggregate is broken is preferentially λ_1 but the alignment $\cos(\lambda_1, \mathbf{r})$ is not always persistent to the most stretching eigen direction of s_{ij} . This reflects the fact that the aggregates do not immediately respond to the ever evolving λ_i all along the Lagrangian trajectory but only with a finite retardation. The time scale for which the aggregate remains aligned with λ_1 prior to the breakage is about $\sim 2 - 4\tau_\eta$.

Therefore, after studying breakage events individually by looking at the competition dynamics of s^2 and ω^2 we found neither a critical s_b^2 nor a common and characteristic time scale of orientation of the aggregate relative to λ_i . Although we found that at the time of breakage an aggregate becomes separated from the fragment in the direction of λ_1 which is indicative of the fact that breakup occurs due to the most extensional strain, this does not explain the cumulative effect of the velocity gradient $\frac{\partial u_i}{\partial x_j}$ acting along the aggregate over time.

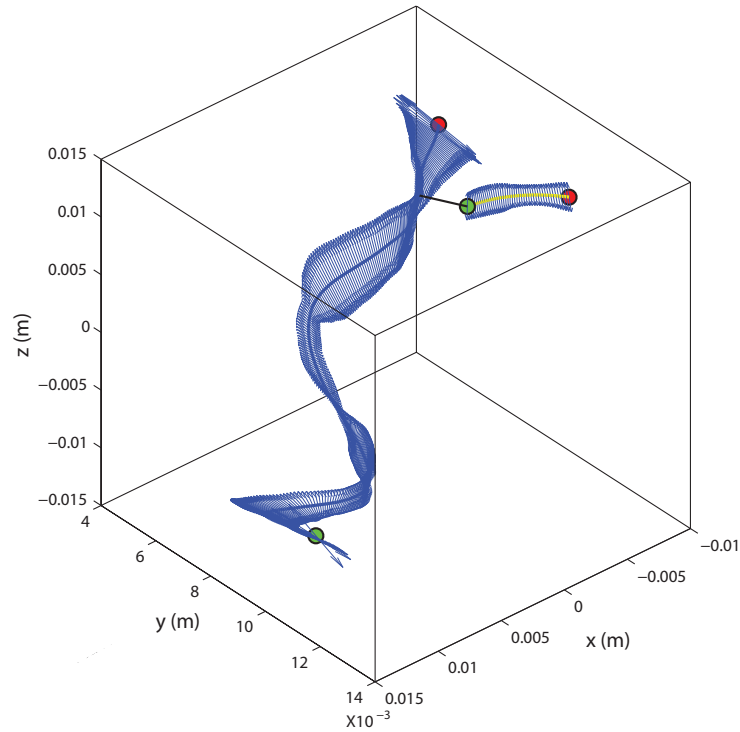


Figure 3.47: The most compressive eigen vector of s_{ij} along the parent and children trajectory.

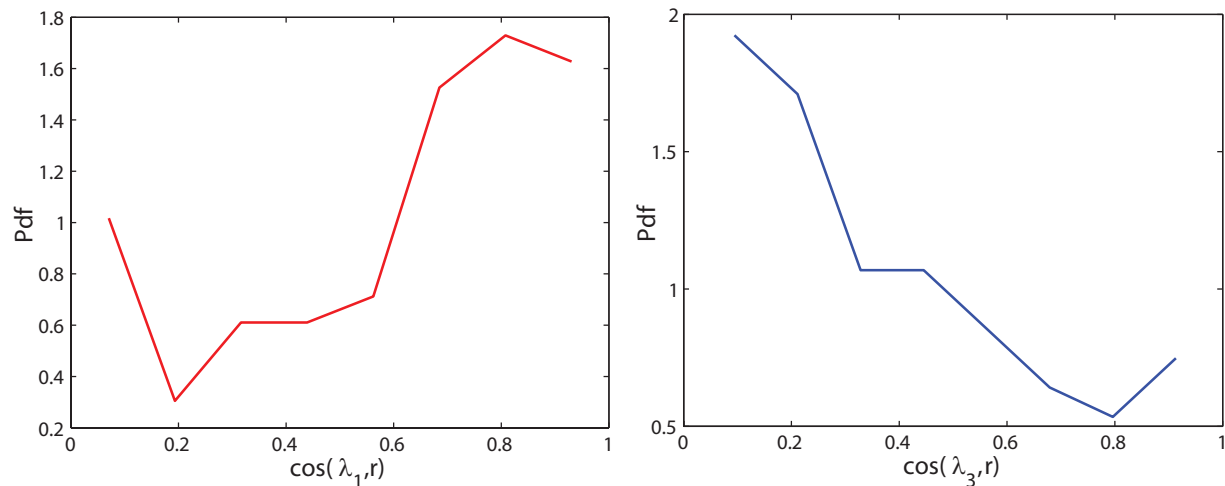


Figure 3.48: Probability density function of the alignment between the separation vector (between the parent and the child at breakage) and eigen direction of the rate of strain tensor shows that r is predominantly aligned with λ_1 , i.e., direction of the most extensional eigen direction of strain .

3.5.4 Integrated deformation analysis

In pursuit of the key role played by $\frac{\partial u_i}{\partial x_j}$ on an aggregate, we analyze the deformation of a fluid volume approximating it as a passive material fluid blob along the trajectory which is expected to shed light on how an aggregate is being volumetrically shaped and distorted in time until it breaks apart. In essence,

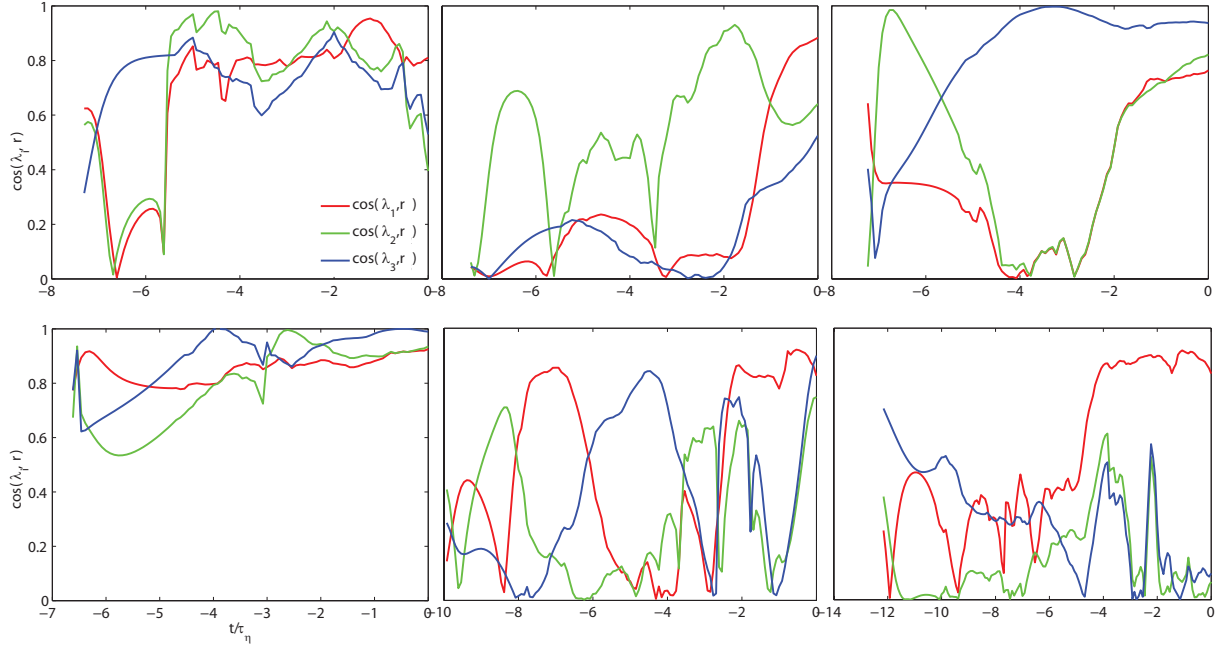


Figure 3.49: Projection of the rate of strain tensor along the separation vector \mathbf{r} between the parent and fragment. The time axis has been normalized by the Kolmogorov time and the time when breakage takes place is pinned at 0. There exists no critical strain along the breakage axis considering the rotation of the aggregate.

we want to know if there exists a critical cumulative deformation Θ_{Cr} above which an aggregate is likely to break which is in fact the result of the integral deformation over a certain length of history in time. We follow Girimaji and Pope [39] to obtain the definition of the Cauchy-Green tensor \mathbb{W} ,

$$\mathbb{W} = \mathbf{B}\mathbf{B}^T \quad (3.15)$$

Here \mathbf{B} is the deformation tensor expressed as $\frac{d}{dt}\mathbf{B} = \mathbf{h}(t) \cdot \mathbf{B}(t)$ and $\mathbf{h}(t) = \left(\frac{\partial u_i}{\partial x_j}\right)_t$ with the initial condition $\mathbf{B}(0) = \mathbf{I}$, \mathbf{I} being the identity matrix. The eigen values of the Cauchy-Green tensor, w_i , where $w_1 \geq w_2 \geq w_3$ represent the three dimensional measure of the fluid blob as $(w_1)^{\frac{1}{2}} : (w_2)^{\frac{1}{2}} : (w_3)^{\frac{1}{2}}$ representing the axis lengths of the approximating deformation ellipsoid. Initially, at $\tau_\eta = 0$, the w_i 's are 1 meaning that the fluid parcel is a sphere. By convention, the eigen vectors of \mathbb{W} , namely, \mathbf{w}_1 and \mathbf{w}_3 refer to the most stretching and compressive direction respectively. The extent of deformation can be estimated by the w_i 's which evolve as $\sqrt{w_i}$. Since volume is a conserved property hence at any time the relationship $w_1 \cdot w_2 \cdot w_3 = 1$ or equivalently $\sum \langle \ln(w_i) \rangle = 0$ holds true for a unit volume.

Since \mathbb{W} is a measure of the integrated history of deformation, the crucial question is what should be the appropriate time integration window over which one should account for the deformation of an aggregate.

As an appropriate unit, we choose the Batchelor time, $\tau_B = \left(\frac{\Delta_0^2}{\epsilon}\right)^{\frac{1}{3}}$, the characteristic time scale over which two fluid particles remember their initial separation i.e., two fluid particles separated by the scale Δ_0 remain in the same eddy of the scale Δ as the standard time window for the integration of \mathbf{B} . After several iterations in search for the appropriate integration time scale, we found a pre factor of $2\tau_B$ which yields to the strongest signal in our alignment statistics and thus suits best for the the integration purpose.

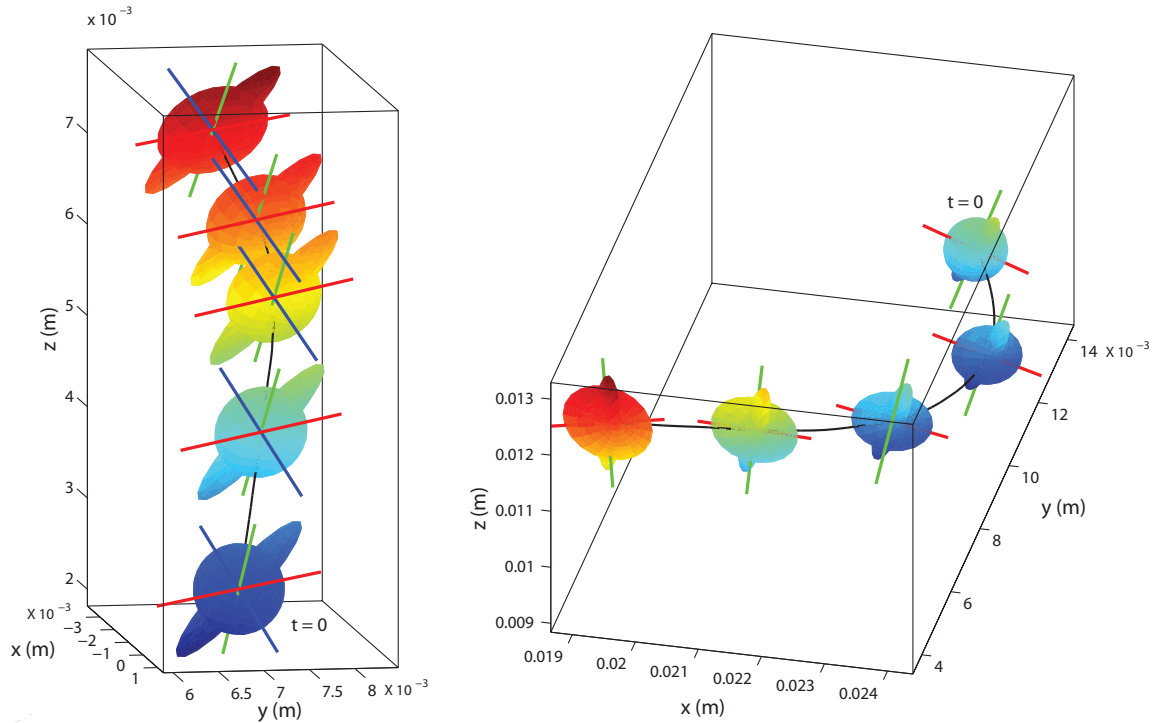


Figure 3.50: An aggregate volume which is a sphere at $t=0$ is seen deformed by the velocity gradient $\frac{\partial u_i}{\partial x_j}$ until the breakage point. Due to the integrated deformation the final shape of the aggregate becomes an ellipse in this particular example of breakage. The embedded axis represents the eigen direction of the Cauchy-Green tensor, i.e., \mathbf{w}_i . Red, green and blue lines denote \mathbf{w}_1 , \mathbf{w}_2 , \mathbf{w}_3 respectively and the 2D ellipse placed inside the volume indicates the plane along which the fragment detaches from the parent. The aggregate shown on the left is seen to be elongated along \mathbf{w}_1 (red) and \mathbf{w}_2 direction. The direction along which the parent and the children get separated (embedded 2D ellipse) aligns approximately with \mathbf{w}_1 . The aggregate shown in the right is seen to be elongated only along the \mathbf{w}_1 direction whereas the separation plane is strongly aligned with \mathbf{w}_2 .

Fig. 3.50 illustrates in two examples how a fluid volume, which was initially a sphere, becomes deformed to an elliptic shape along the Lagrangian trajectory on the way to breakage. Besides the history of the deformation, the evolution of \mathbb{W}_i is also visible as the eigen vectors, i.e., \mathbf{w}_1 , \mathbf{w}_2 , \mathbf{w}_3 are shown in red, green and blue respectively. In addition, the direction along which the fragment is detached from the original aggregate body is shown by an elongated ellipse across the volume. In one event in Fig. 3.50 (right) we find that the aggregate is stretched not only along \mathbf{w}_1 but also almost equally strong in the direction of \mathbf{w}_2 and eventually breaks apart along \mathbf{w}_2 confirmed by its preferred alignment with the separation plane. On the other hand, from the event shown in Fig. 3.50 (left) we observe the aggregate stretched only in \mathbf{w}_1 and approximately aligned with the separation plane. Fig. 3.52 shows an ensemble of how \mathbf{r} is aligned with these two stretching directions \mathbf{w}_1 and \mathbf{w}_2 in time and the way they mutually prevail over each other.

In Fig. 3.51, we show how the alignment of the most extensional and compressive eigen vector of the Cauchy-Green tensor with the separation vector between the fragments evolves integrating over different Batchelor time scales. We choose two Batchelor time scales as an appropriate integration window as for

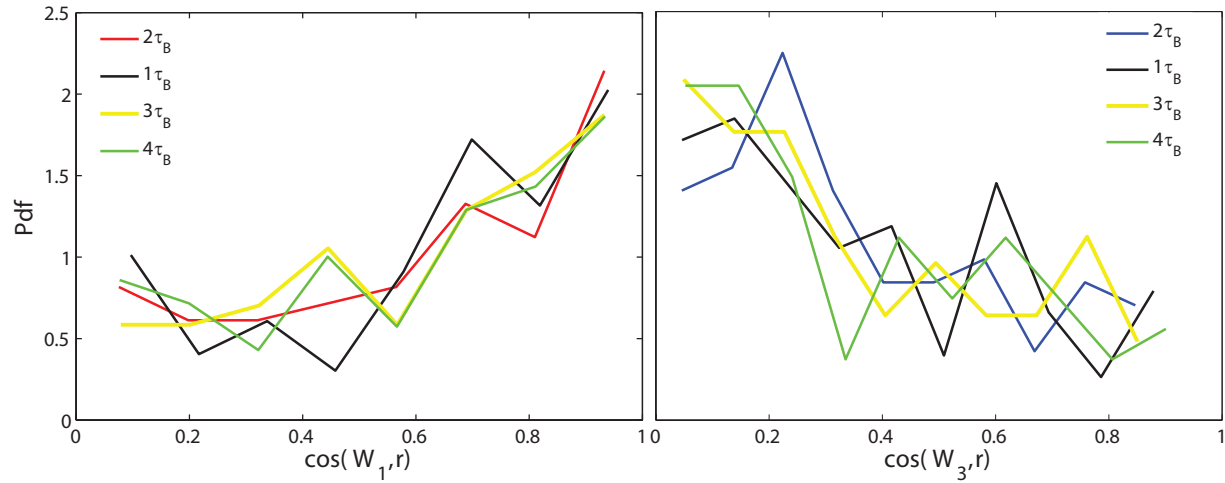


Figure 3.51: Pdf of the alignment of the most extensive and compressive eigen vectors of Cauchy-Green tensor with the separation direction between the fragments. The deformation of the fluid volume is integrated using different Batchelor time scale.

this time scale we found comparatively better alignment and this time scale allows us to take almost all the experiments into account for the analysis. Integrating over two Batchelor time scales requires longer aggregate trajectories which become scarce.

Fig. 3.53 shows the probability distribution function of the alignment of the separation direction \mathbf{r} with the most stretching and compressive eigen direction of the Cauchy-Green deformation tensor. From Fig. 3.53 it is clear that the separation direction \mathbf{r} is strongly aligned with the most stretching (left) and anti aligned with the most compressive (right) eigen direction of the Cauchy-Green deformation tensor. This reflects the fact that the aggregates are mostly broken due to the integrated deformation in the direction of \mathbf{w}_1 despite of the stretching nature of w_2 .

To comprehend the "look" of the deformed volume, the "shape" of S_{ij} or \mathbb{W} expressed as the ratio of $\frac{\Lambda_2}{\Lambda_1}$ and $\frac{\ln(w_2)}{\ln(w_1)}$ respectively is used. In different limits of values such as $\frac{\Lambda_2}{\Lambda_1} \in \mathbb{R}$ and $\frac{\ln(w_2)}{\ln(w_1)} \in \mathbb{R}$, the volume of the deformed aggregate would resemble the shape of the so called "pancake" or "cigar". Describing the situation qualitatively, one could imagine the "pancake" shape of an aggregate when both $\ln(w_2)$ and $\ln(w_1)$ are active on the aggregate which will result in a minimum w_3 . Hence whenever an aggregate will be subjected to bidirectional stretching and minimum compression the "disc" like shape results which is synonymously referred to as "pancake". By contrast, when w_2 takes the minimum value, then the shape will lead to a "cigar" shape, i.e., unidirectional stretching by w_1 and strong compression by w_3 .

The ratios $\frac{\Lambda_2}{\Lambda_1}$ and $\frac{\ln(w_2)}{\ln(w_1)}$ from Fig. 3.54 do not show any defining indication for any of the shapes discussed above. We attribute the narrow range of the aggregate size to this inconclusive picture of the deformed shape.

Likewise we found no clear relation between the strain at breakage s_b and the size of the aggregate. Fig. 3.55 shows the size dependency on the strain required to break the aggregates. The aggregates of almost same size, i.e., 1 mm are broken by the strain varying approximately two order of magnitude. From the scaling between the size and strain as shown in Fig. 3.24, we observe that smaller aggregates require higher strain to be broken and vice versa. But in the case of breakage in homogeneous quasi isotropic turbulence we notice that smaller aggregates may not always need higher strain to be broken.

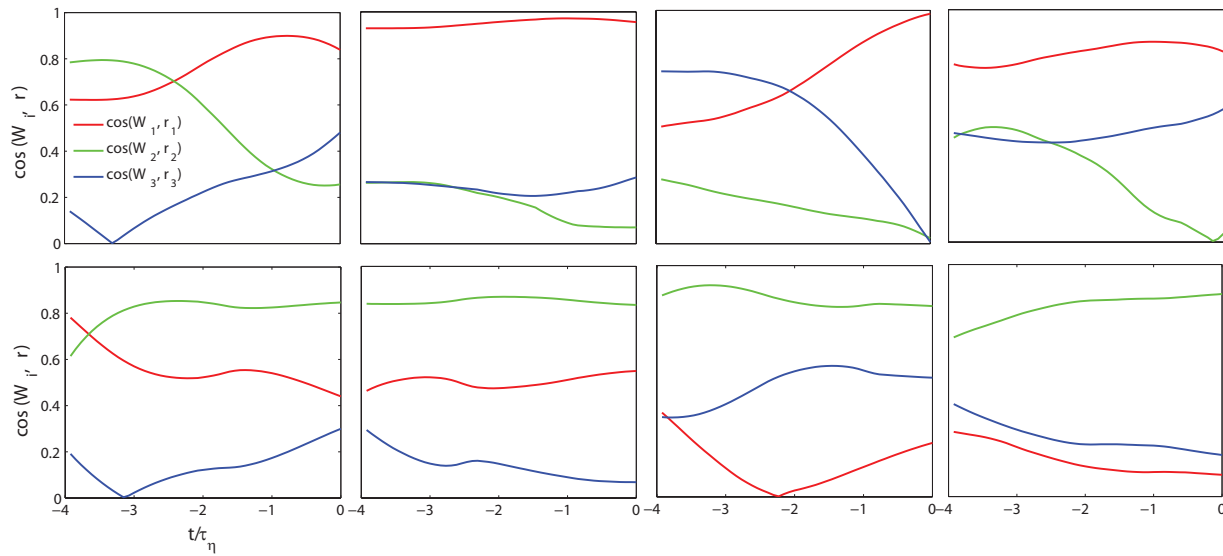


Figure 3.52: Orientation of the separation vector \mathbf{r} relative to \mathbb{W} over $2T_B$. Figures in the top row shows for some breakage events the aggregate remains consistently aligned with \mathbf{w}_1 whereas figures in the bottom row reveals that stretching in \mathbf{w}_2 can dominate over \mathbf{w}_1 and hence the aggregate is aligned and stretched along \mathbf{w}_2 .

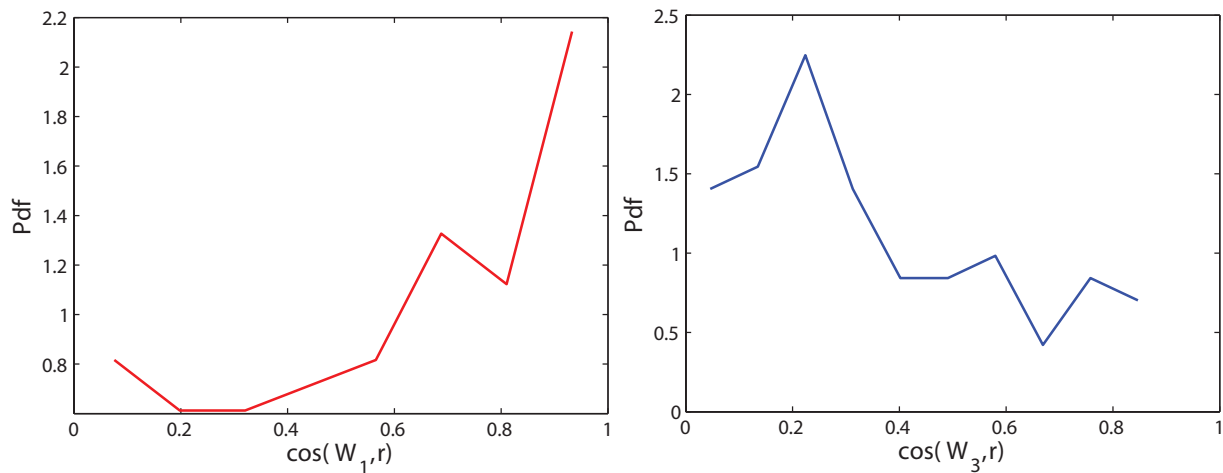


Figure 3.53: Probability density function of the separation vector and Cauchy-Green eigen vector suggests that separation takes place mostly in the direction where stretching is maximum.

We attribute this to the fluctuating strain that an aggregate experiences until breakup. Referring to the Fig. 3.43, we infer that the smaller aggregates which are broken at relatively low strain might have experienced higher strain before the breakup causing enough structural damage and eventually needed a lower strain at the time of breakage. This is the reason why we found no explicit scaling between the size of the aggregates and strain at breakage. From Fig. 3.55 we rather conclude that there exists an envelope in the s^2 limit of $\mathcal{O}(100)(1/sec^2)$ with corresponding size limit on $\mathcal{O}(1)mm$. In this Fig. 3.55 the color bar represents the ratio of the intermediate to most compressive (left) and the most extensive to compressive eigen values (right) of the rate of strain. The effect of stretching and compression on the size

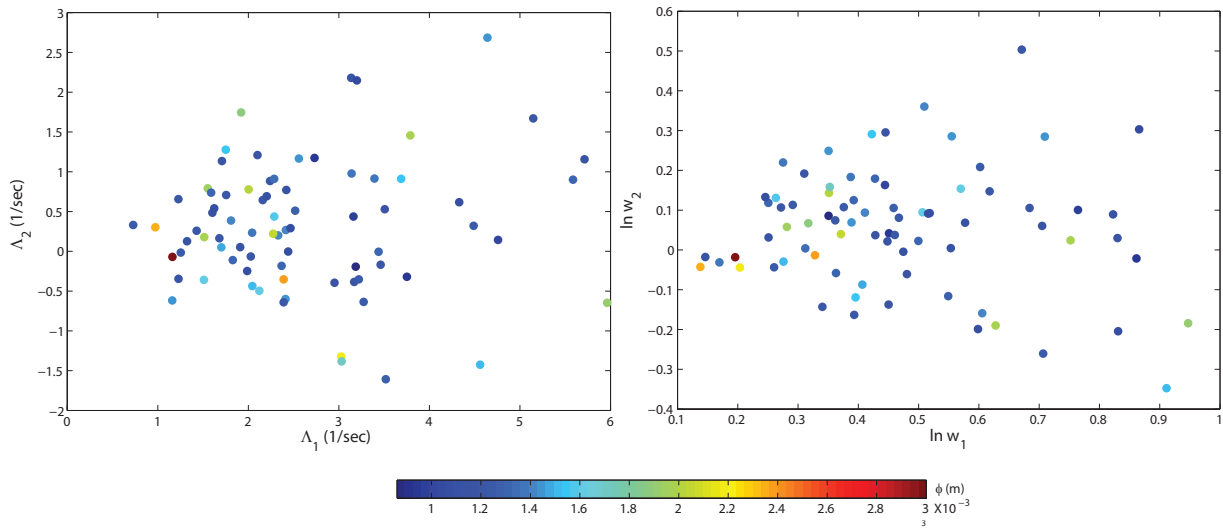


Figure 3.54: Joint pdf of Λ_1 and Λ_2 (left), an instantaneous measure at breakage and (right) joint pdf of $\ln(w_1)$ and $\ln(w_2)$, an integrated measure over $2\tau_B$ from the breakage to estimate the "shape" of the deformed volume.

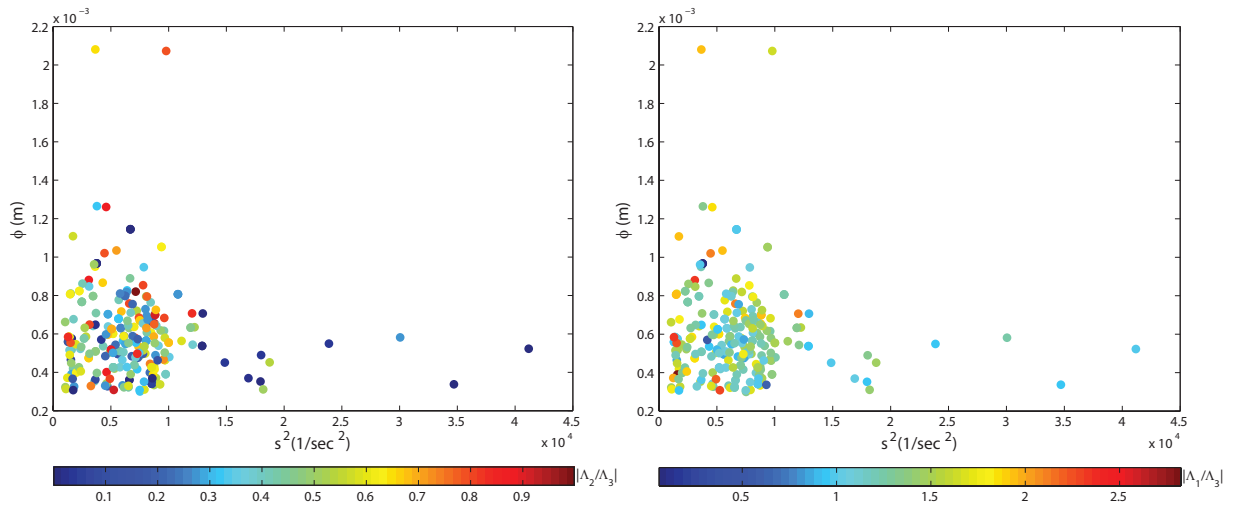


Figure 3.55: Aggregate size does not show any clear scaling with the corresponding strain responsible for breakage. The aggregates of size $\sim 1\text{mm}$ are subject to break at a wide range of strain implying internal mechanical inhomogeneity. The size is encoded by the ratio of the intermediate to most compressive eigen value of the rate of strain, i.e., $|\frac{\Lambda_2}{\Lambda_3}|$ (left) which shows that majority of the breakage events take place due to almost uniaxial straining during the breakup. This is also confirmed by looking at the ratio of the most stretching to compressive eigen values of the rate of strain $|\frac{\Lambda_1}{\Lambda_3}|$ (right).

of the aggregates is also not pronounced as similar sized aggregates could experience contrasting values of Λ_i 's. This means that an aggregate at the time of breakage might be elongated or sheared unlike the breakage phenomena in axisymmetric extensional flow in the orifice where most of the aggregates were broken due to elongation.

3.6 Concluding remark: Breakup in homogeneous quasi isotropic turbulence

We summarize the findings of the aggregate breakup in homogeneous quasi isotropic turbulence as:

- Unlike in the orifice experiment, where most of aggregates broke in the flow domain where strain is maximum, an aggregate in turbulent flow very often breaks at a strain magnitude smaller than the strain intensity back in time along its Lagrangian trajectory.
- We investigated the Lagrangian history of individual aggregate trajectory and found that there exists no critical strain which can uniquely define the breakage.
- The axis along which two fragments separate at the time of breakage is not always aligned with the strain. Therefore strain has no persistent effect on the axis of breakage in history.
- The axis of breakage, i.e., the direction along which two fragments separate is also not consistently aligned with the eigen frame of rate of strain tensor. So, the predominant effect of the most stretching eigen vector is not pronounced back in history.
- We confirm that, there exists a time scale, as we found it as two Batchelor times, over which the integrated deformation define the breakage statistically, i.e., when an aggregate deformation is approximated by the Cauchy-Green deformation tensor integrating over two Batchelor times, equivalently four Kolmogorov times in our experiment, exhibits critical deformation at which all the aggregates undergo breakage. Therefore we conclude deformation over two Batchelor time as the defining criteria for the breakup.

Chapter 4

Conclusion

Particle tracking experiments on the breakup of clusters made of nano particles, known as aggregates, are carried out in axisymmetric extensional laminar flow and homogeneous quasi isotropic turbulence. For uniaxial converging flow, we used Brownian motion driven aggregates, i.e., aggregation in quiescent flow conditions whereas to investigate the breakup in turbulent flow we used aggregates produced under shear flow. In both the experiments the mean aggregate size was $\langle d_p \rangle \sim 1\text{mm}$ with a standard deviation of 0.5 mm and a fractal dimension $d_f \sim 1.88$ which is indicative of an open structure. To the best of our knowledge, this is the first experimental work on breakup of fractal aggregates where the underlying breakup mechanism is investigated fully three dimensionally and in a Lagrangian frame using state of the art optical instruments. Most importantly the simultaneous measurement of the fluid and the particle phase sets a new milestone from the technical point of view.

For the converging laminar flow where the rate of strain, s^2 , increases monotonically approaching the orifice where it reaches the maximum value of order $\mathcal{O}(10^4)(1/\text{sec}^2)$, we found that most of the aggregates are broken in the proximity of the orifice due to uniaxial straining by the most extensional eigen value of the rate of strain tensor, Λ_1 . From the spatial distribution of the eigen values of s_{ij} , we found a non vanishing intermediate eigen value Λ_2 which appeared to be mostly compressive in nature in front of the orifice and with the compressive eigen vector λ_3 are compressing the aggregate on the plane normal to the most extensional eigen vector λ_1 . Beyond the orifice, i.e., inside the channel in the limit of vanishing Λ_2 , Λ_1 and Λ_3 are of equal magnitude and the associated eigen vectors approximately form a 45° angle with respect to the wall, like in a canonical wall bounded shear flow. The stresses due to the simple shear are lower in magnitude compared to the orifice entrance, but yet there are a few breakage events that occur under the action of simple shear. We attribute the breakup of aggregates occurring inside the channel, which indeed survived the maximum strain in front of the orifice, to the fact that the mechanical strength of the aggregates is very heterogeneous. Simple shear is reported to rotate the aggregates rather than deforming them and hence morphological compactification resists disintegration. But in our experiment, the surviving aggregates having endured stretching in front of the orifice that already weakens the cohesive bonds undergo fragmentation under the action of simple shear at relatively low strain magnitude. Due to this unavoidable elongational effect a fair comparison between the breakage governed by axisymmetric straining and simple shear is not possible in our laminar flow experiment. Therefore, we infer that the breakup in the simple shear flow domain is actively assisted by axisymmetric straining. In an attempt to establish a correlation between the size of the aggregate and the critical strain, we found an inverse dependency of the size on critical strain, i.e., a smaller aggregate

requires higher strain for breakage and vice versa. This is the first of our major findings. Despite the fact the aggregates are very heterogeneous in strength, their breakage is consistent with the canonical power law $\langle d_p \rangle \propto (\sqrt{s^2})^{-n}$ where $n \in [-0.35, -0.55]$ by comparing the result as measured by 3D-PTV with small angle light scattering (SALS). The variation of the individual size and strain ratio is significant and possibly should be included into future breakage kernels.

In a second set of experiments we measured aggregate breakage in a fully turbulent flow. We follow the aggregates in a Lagrangian way, measuring the full set of velocity gradient tensor, $\frac{\partial u_i}{\partial x_j}$ along the trajectories via simultaneous Lagrangian tracking of tracer particles. We find that the scaling between the initial size of the aggregates and strain at breakage exhibits qualitative similarity with that of the one found in axisymmetric straining flow. Going beyond the instantaneous state of straining at the time of breakage, we emphasized on the history of straining and rotation *prior* to the breakage event. That means, our result point to the importance of the Lagrangian history rather than the instantaneous contribution of the small scale dynamics in pursuit of a critical parameter governing the breakup. Systematically studying the strain and enstrophy that uniquely define the velocity gradient field along the aggregate trajectory we found a competing mechanism between strain and enstrophy for the entire set of the experiments. The critical values of s^2 and ω^2 appear not only completely stochastic but also they do not explain the phenomena where an aggregate is broken after sustaining higher intensity of s^2 at a significant time *prior* to the actual failure. Similar to some breakage events in orifice experiments, this may be pointing to a sort of fatigue process, where a major part of the bonds are already broken, while a few remaining bonds still manage to hold the aggregate together for some time.

We found that the direction along which the fragments are separated predominantly aligns with λ_1 in agreement with the expectation that two parts belonging to an unbroken aggregate under stretching should break and separate along the direction of stretching. Finally we analyzed the critical deformation of the aggregate volume over a characteristic time scale. Integrating the Cauchy-Green deformation tensor over the recent Lagrangian history, we found persistent alignment of the separation direction with the most stretching eigen vector of the Cauchy-Green tensor for almost all of the breakup events. We note that this alignment of the separation vector with the eigen frame of the Cauchy-Green tensor is more pronounced than the corresponding alignment with s_{ij} , which is reflecting the predominance of the Lagrangian history prior to breakage over the instantaneous state at breakage. It turns out that this alignment is most prominent if the integration time spans two Batchelor times, in our particular case equivalent to four Kolmogorov times. Thus we conclude that the Lagrangian retrospective of the integrated deformation of the aggregates over $2\tau_B$, is the critical time scale needed for the breakup.

Bibliography

- [1] ANDREAE, M. O., AND CRUTZEN, P. J. Atmospheric aerosols: Biogeochemical sources and role in atmospheric chemistry. *Science* 276 (1997), 1052–1058.
- [2] AS. MOUSSA, M. SOOS, J. S., AND MORBIDELLI, M. Effect of solid volume fraction on aggregation and breakage in colloidal suspensions in batch continuous stirred tanks. *Langmuir* 23 (2007), 1664–1673.
- [3] AUTON, T. R., HUNT, J. C. R., AND PRUDHOMME, M. The force exerted on a body in inviscid unsteady non-uniform rotational flow. *J. Fluid Mech.* 197 (1988), 241–257.
- [4] BABIANO, A., CARTWRIGHT, J. H. E., PIRO, O., AND PROVENZALE, A. Dynamics of a small neutrally buoyant sphere in a fluid and targeting in hamiltonian systems. *Phys. Rev. Lett.* 84 (2000), 5764–5767.
- [5] BABLER, M. U., BIFERALE, L., AND LANOTTE, A. S. Breakup of small aggregates driven by turbulent hydrodynamical stress. *Phys. Rev. E* 85 (2012).
- [6] BABLER, M. U., MORBIDELLI, M., AND BALDYGA, J. Modelling the breakup of solid aggregates in turbulent flows. *J. Fluid Mech.* 612 (2008), 261–289.
- [7] BAEBLER, M. U. A collision efficiency model for flow-induced coagulation of fractal aggregates. *AIChE Journal* 54 (2008), 1748–1760.
- [8] BAEBLER, M. U., MOUSSA, A. S., SOOS, M., AND MORBIDELLI, M. Structure and kinetics of shear aggregation in turbulent flows. I. early stage of aggregation. *Langmuir* 26 (2010), 13142–13152.
- [9] BAGCHI, P., AND BALACHANDAR, S. Effect of turbulence on the drag and lift of a particle. *Phys. Fluids* 15 (2003), 3496–3513.
- [10] BAGCHI, P., AND BALACHANDAR, S. Inertial and viscous forces on a rigid sphere in straining flows at moderate reynolds numbers. *J. Fluid Mech.* 481 (2003), 105–148.
- [11] BAGSTER, D., AND TOMI, D. The stresses within a sphere in simple flow fields. *Chemical Engineering Science* 29 (1974), 1773 – 1783.
- [12] BATCHELOR, G. Transport properties of 2-phase materials with random structure. *Annu. Rev. Fluid Mech.* 6 (1974), 227–255.
- [13] BECKER, V., SCHLAUCH, E., BEHR, M., AND BRIESEN, H. Restructuring of colloidal aggregates in shear flows and limitations of the free-draining approximation. *Journal of Colloid and Interface Science* 339 (2009), 362–372.

- [14] BINDER, C., FEICHTINGER, C., SCHMID, H.-J., THUERREY, N., PEUKERT, W., AND RUEDE, U. Simulation of the hydrodynamic drag of aggregated particles. *Journal of Colloid and Interface Science* 301 (2006), 155–167.
- [15] BLASER, S. Break-up of flocs in contraction and swirling flows. *Colloids and Surfaces A-physicochemical and Engineering Aspects* 166 (2000), 215–223.
- [16] BLASER, S. Flocs in shear and strain flows. *Journal of Colloid and Interface Science* 225 (2000), 273–284.
- [17] BORGAS, M. S., AND YEUNG, P. Relative dispersion in isotropic turbulence. Part 2. A new stochastic model with Reynolds-number dependence. *J. Fluid Mech.* 503 (2004), 125–160.
- [18] BORUE, V., AND ORZAG, S. A. Local energy flux and subgrid-scale statistics in three-dimensional turbulence. *J. Fluid Mech.* 366 (1998), 1–31.
- [19] BRADY, J. F., AND BOSSIS, G. Stokesian dynamics. *Annu. Rev. Fluid Mech.* 20 (1988), 111–157.
- [20] BRENNER, H., AND CONDIFF, D. W. Transport mechanics in systems of orientable particles .3. arbitrary particles. *Journal of Colloid and Interface Science* 41 (1972), 228–235.
- [21] BROWN, D., AND GLATZ, C. Aggregate breakage in protein precipitation. *Chemical Engineering Science* 42 (1987), 1831–1839.
- [22] BROWN, R. D., WARHAFT, Z., AND VOTH, G. A. Acceleration statistics of neutrally buoyant spherical particles in intense turbulence. *Phys. Rev. Lett.* 103 (2009), 194501.
- [23] BURTON, T. M., AND EATON, J. K. Fully resolved simulations of particle-turbulence interaction. *J. Fluid Mech.* 545 (2005), 67–111.
- [24] CALZAVARINI, E., KERSCHER, M., LOHSE, D., AND TOSCHI, F. Dimensionality and morphology of particle and bubble clusters in turbulent flow. *J. Fluid Mech.* 607 (2008), 13–24.
- [25] CALZAVARINI, E., VOLK, R., BOURGOIN, M., LEVEQUE, E., PINTON, J. . F., AND TOSCHI, F. Acceleration statistics of finite-sized particles in turbulent flow: the role of faxen forces. *J. Fluid Mech.* 630 (2009), 179–189.
- [26] CANTWELL, B. Exact solution of a restricted euler equation for the velocity-gradient tensor. *Phys. Fluids* 4 (1992), 782–793.
- [27] CHACIN, J. M., AND CANTWELL, B. J. Dynamics of a low reynolds number turbulent boundary layer. *J. Fluid Mech.* 404 (2000), 87–115.
- [28] COULALOGLOU, C. A., AND TAVLARIDES, L. L. Description of interaction processes in agitated liquid-liquid dispersions. *Chemical Engineering Science* 32 (1977), 1289–1297.
- [29] DER BOS, F. V., TAO, B., MENEVEAU, C., AND KATZ, J. Effects of small-scale turbulent motions on the filtered velocity gradient tensor as deduced from holographic particle image velocimetry measurements. *Phys. Fluids* 14 (2002), 2456–2474.
- [30] EGGERSDORFER, M. L., KADAU, D., HERRMANN, H. J., AND PRATSINIS, S. E. Fragmentation and restructuring of soft-agglomerates under shear. *Journal of Colloid and Interface Science* 342 (2010), 261–268.

- [31] EHRL, L., SOOS, M., AND LATTUADA, M. Generation and geometrical analysis of dense clusters with variable fractal dimension. *Journal of Physical Chemistry B* 113 (2009), 10587–10599.
- [32] EHRL, L., SOOS, M., AND MORBIDELLI, M. Dependence of aggregate strength, structure, and light scattering properties on primary particle size under turbulent conditions in stirred tank. *Langmuir* 24 (2008), 3070–3081.
- [33] EHRL, L., SOOS, M., MORBIDELLI, M., AND BAEBLER, M. U. Dependence of initial cluster aggregation kinetics on shear rate for particles of different sizes under turbulence. *AIChE Journal* 55 (2009), 3076–3087.
- [34] FAIR, G. M., AND GEMMELL, R. S. Mathematical model of coagulation. *Journal of Colloid Science* 19 (1964), 360–370.
- [35] FAXEN, H. Der widerstand gegen die bewegung einer starren kugel in einer zähen flüssigkeit, die zwischen zwei parallelen ebenen wänden eingeschlossen ist. *Ann. Phys.* 373, 10 (1922), 89–119.
- [36] FENG, X., AND XIAO-YAN, L. Modelling the kinetics of aggregate breakage using improved breakage kernel. *Water Science and Technology* 57 (2008), 151–157.
- [37] FILIPPOV, A. V., ZURITA, M., AND ROSNER, D. E. Fractal-like aggregates: Relation between morphology and physical properties. *Journal of Colloid and Interface Science* 229 (2000), 261–273.
- [38] GATIGNOL, R. The faxen formulas for a rigid particle in an unsteady non-uniform stokes-flow. *Journal De Mecanique Theorique Et Appliquee* 2, 2 (1983), 143–160.
- [39] GIRIMAJI, S. S., AND POPE, S. B. Material-element deformation in isotropic turbulence. *J. Fluid Mech.* 220 (1990), 427–458.
- [40] GLASGOW, L. A., AND HSU, J. P. An experimental-study of floc strength. *AIChE Journal* 28 (1982), 779–785.
- [41] GLASGOW, L. A., AND LIU, X. Response of aggregate structures to hydrodynamic stress. *AIChE Journal* 37 (1991), 1411–1414.
- [42] GRUEN, A. W., AND BALTSAVIAS, E. P. Geometrically constrained multiphoto matching. *Photogrammetric Engineering and Remote Sensing* 54 (1988), 633–641.
- [43] GUEZENNEC, Y. G., BRODKEY, R. S., TRIGUI, N., AND KENT, J. C. Algorithms for fully automated 3-dimensional particle tracking velocimetry. *Exp. Fluids* 17 (1994), 209–219.
- [44] HARADA, S., TANAKA, R., NOGAMI, H., AND SAWADA, M. Dependence of fragmentation behavior of colloidal aggregates on their fractal structure. *Journal of Colloid and Interface Science* 301 (2006), 123–129.
- [45] HARSHE, Y. M., AND LATTUADA, M. Breakage rate of colloidal aggregates in shear flow through stokesian dynamics. *Langmuir* 28 (2012), 283–292.
- [46] HARSHE, Y. M., LATTUADA, M., AND SOOS, M. Experimental and modeling study of breakage and restructuring of open and dense colloidal aggregates. *Langmuir* 27 (2011), 5739–5752.

- [47] HASSAN, Y. A., AND CANAAN, R. E. Full-field bubbly flow velocity-measurements using a multi-frame particle tracking technique. *Exp. Fluids* 12 (1991), 49–60.
- [48] HIGASHITANI, K., AND IIMURA, K. Two-dimensional simulation of the breakup process of aggregates in shear and elongational flows. *Journal of Colloid and Interface Science* 204 (1998), 320–327.
- [49] HIGASHITANI, K., IIMURA, K., AND SANDA, H. Simulation of deformation and breakup of large aggregates in flows of viscous fluids. *Chemical Engineering Science* 56 (2001), 2927–2938.
- [50] HIGASHITANI, K., INADA, N., AND OCHI, T. Floc breakup along centerline of contractile flow to orifice. *Colloids and Surfaces* 56 (1991), 13–23.
- [51] HOYER, K., HOLZNER, M., LUTHI, B., GUALA, M., LIBERZON, A., AND KINZELBACH, W. 3d scanning particle tracking velocimetry. *Exp. Fluids* 39, 5 (Nov. 2005), 923–934.
- [52] HUNTER, R. J., AND FRAYNE, J. Flow behavior of coagulated colloidal sols. 5. dynamics of floc growth under shear. *Journal of Colloid and Interface Science* 76 (1980), 107 – 115.
- [53] JANKOWSKI, J. A., MALCHEREK, A., AND ZIELKE, W. Numerical modeling of suspended sediment due to deep-sea mining. *Journal of Geophysical Research-oceans* 101 (1996), 3545–3560.
- [54] K. HIGASHITANI, N. I., AND OCHI, T. Floc breakup along centerline of contractile flow to orifice. *Colloids and surfaces* 56 (1991), 13–28.
- [55] KAO, S. V., AND MASON, S. G. Dispersion of particles by shear. *Nature* 253 (1975), 621–2.
- [56] KHOLMYANSKY, M., TSINOBER, A., AND YORISH, S. Velocity derivatives in the atmospheric surface layer at $Re_{\lambda}=10^4$. *Phys. Fluids* 13, 1 (2001), 311–314.
- [57] KOBAYASHI, M. Breakup and strength of polystyrene latex flocs subjected to a converging flow. *Colloids and Surfaces A-physicochemical and Engineering Aspects* 235 (2004), 73–78.
- [58] KOBAYASHI, M., ADACHI, Y., AND OOI, S. Breakup of fractal flocs in a turbulent flow. *Langmuir* 15, 13 (1999), 4351–4356.
- [59] KOTOWSKI, R. Phototriangulation in multi-media-photogrammetry. *International Archives of Photogrammetry and Remote Sensing XXVII* (1988).
- [60] KRUTZER, L. L. M., VANDIEMEN, A. J. G., AND STEIN, H. N. The influence of the type of flow on the orthokinetic coagulation rate. *Journal of Colloid and Interface Science* 171 (1995), 429–438.
- [61] KULMALA, M., VEHKAMAKI, H., PETAJA, T., DAL MASO, M., LAURI, A., KERMINEN, V. M., BIRMILI, W., AND MCMURRY, P. H. Formation and growth rates of ultrafine atmospheric particles: a review of observations. *Journal of Aerosol Science* 35 (2004), 143–176.
- [62] KUSTERS, K. A., WIJERS, J. G., AND THOENES, D. Aggregation kinetics of small particles in agitated vessels. *Chemical Engineering Science* 52 (1997), 107–121.
- [63] L. GUO, C. C., AND SANTSCHI, P. The distribution of colloidal and dissolved organic carbon in the gulf of mexico. *Mar. Chem.* 45 (1994), 105–109.

- [64] LATTUADA, M., AND MORBIDELLI, M. Effect of repulsive interactions on the rate of doublet formation of colloidal nanoparticles in the presence of convective transport. *Journal of Colloid and Interface Science* 355 (2011), 42–53.
- [65] LATTUADA, M., WU, H., SANDKUHLER, P., SEFCIK, J., AND MORBIDELLI, M. Modelling of aggregation kinetics of colloidal systems and its validation by light scattering measurements. *Chemical Engineering Science* 59 (2004), 1783–1798.
- [66] LATTUADA, M., WU, H., SEFCIK, J., AND MORBIDELLI, M. Detailed model of the aggregation event between two fractal clusters. *Journal of Physical Chemistry B* 110 (2006), 6574–6586.
- [67] LIN, M. Y., LINDSAY, H. M., WEITY, D. A., KLEIN, R., BALL, R. C., AND MEAKIN, P. Universal diffusion-limited colloid aggregation. *Journal of Physics-condensed Matter* 2 (1990), 3093–3113.
- [68] LIU, S. X., AND GLASGOW, L. A. Aggregate disintegration in turbulent jets. *Water Air and Soil Pollution* 95 (1997), 257–275.
- [69] LOTH, E., AND DORGAN, A. J. An equation of motion for particles of finite reynolds number and size. *Environmental Fluid Mechanics* 9, 2 (Apr. 2009), 187–206.
- [70] LOVALENTI, P. M., AND BRADY, J. F. The hydrodynamic force on a rigid particle undergoing arbitrary time-dependent motion at small reynolds-number. *J. Fluid Mech.* 256 (1993), 561–605.
- [71] LU, P. J., CONRAD, J. C., WYSS, H. M., SCHOFIELD, A. B., AND WEITZ, D. A. Fluids of clusters in attractive colloids. *Phys. Rev. Lett.* 96 (2006).
- [72] LUMLEY, J. L. Drag reduction by additives. *Annu. Rev. Fluid Mech.* 1 (1969), 367–387.
- [73] LÜTHI, B., OTT, S., BERG, J., AND MANN, J. Lagrangian multi-particle statistics. *J. Turbulence* 8, 45 (2007), 1–17.
- [74] LÜTHI, B., TSINOBER, A., AND KINZELBACH, W. Lagrangian measurement of vorticity dynamics in turbulent flow. *J. Fluid Mech.* 528 (2005), 87–118.
- [75] M. ELIMELECH, J. GREGORY, X. J., AND WILLIAMS, R. *Particle Deposition and Aggregation-Measurement, Modelling and simulation*. New York, 1995.
- [76] M. ELIMELECH, J. GREGORY, X. J. R. W. *Particle Deposition & Aggregation*. Butterworth-Heinemann, 1998.
- [77] M. GUALA, B.LÜTHI, A. L. A. T., AND KINZELBACH, W. On the evolution of material lines and vorticity in homogeneous turbulence. *J. Fluid Mech.* 533 (2005), 339–359.
- [78] MAAS, H. G. Digital photogrammetry for determination of tracer particle coordinates in turbulent-flow research. *Photogrammetric Engineering and Remote Sensing* 57, 12 (1991), 1593–1597.
- [79] MAAS, H. G. Complexity analysis for the determination of image correspondence in dense spatial target fields. *International Archives of Photogrammetry and Remote Sensing XXIX, Part B5* (1992), 102–107.
- [80] MAAS, H. G. High-speed solid state camera systems for digital photogrammetry. *International Archives of Photogrammetry and Remote Sensing XXIX* (1992).

- [81] MAAS, H. G. Automated dem generation by multi-image featured based matching. *IAPRS 31, Part3* (1996).
- [82] MAAS, H. G., GRUEN, A., AND PAPANTONIOU, D. Particle tracking velocimetry in 3-dimensional flows .1. photogrammetric determination of particle coordinates. *Exp. Fluids 15* (1993), 133–146.
- [83] MAGNAUDET, J., AND LEGENDRE, D. Some aspects of the lift force on a spherical bubble. *Applied Scientific Research 58* (1998).
- [84] MALIK, N. A., AND DRACOS, T. Interpolation schemes for 3-dimensional velocity-fields from scattered data using taylor expansions. *Journal of Computational Physics 119* (1995), 231–243.
- [85] MALIK, N. A., DRACOS, T., AND PAPANTONIOU, D. A. Particle tracking velocimetry in 3-dimensional flows .2. particle tracking. *Exp. Fluids 15* (1993).
- [86] MARCHISIO, D. L., SOOS, M., SEFCIK, J., MORBIDELLI, M., BARRESI, A. A., AND BALDI, G. Effect of fluid dynamics on particle size distribution in particulate processes. *Chemical Engineering & Technology 29* (2006), 191–199.
- [87] MARCHISIO, D. L., VIGIL, R. D., AND FOX, R. O. Implementation of the quadrature method of moments in cfd codes for aggregation-breakage problems. *Chemical Engineering Science 58* (2003), 3337–3351.
- [88] MARTIN, J. M., DAI, M. H., AND CAUWET, G. Significance of colloids in the biogeochemical cycling of organic-carbon and trace-metals in the venice lagoon (italy). *Limnology and Oceanography 40* (1995), 119–131.
- [89] MAXEY, M. R., AND RILEY, J. J. Equation of motion for a small rigid sphere in a nonuniform flow. *Phys. Fluids 26* (1983), 883–889.
- [90] MÜHLE, K., D. B. M. D. *Coagulation and Flocculation*. New York, 1993.
- [91] MICHAELIDES, E. Review-the transient equation of motion for particles, bubbles and. droplets. *J. Fluids Engin. 119* (1997), 233.
- [92] MONIN, A., AND YAGLOM, A. M. *Statistical Fluid Mechanics*. MIT pres, Cambridge, MA, 1975.
- [93] MORAN, S., AND MOORE, R. The distribution of colloidal aluminum and organic carbon in coastal and open ocean waters off nova scotia. *Geochim. Cosmochim 53* (1989), 2519–2527.
- [94] NATANEL KORIN, MATHUMAI KANAPATHIPILLAI, B. D. M. M. C. A. B., AND MAMMOTO, T. Shear-activated nanotherapeutics for drug targeting to obstructed blood vessels. *Science 337* (2012), 738–742.
- [95] NAVARRETE, R. C., SCRIVEN, L. E., AND MACOSKO, C. W. Rheology and structure of flocculated iron oxide suspensions. *Journal of Colloid and Interface Science 180* (1996), 200–211.
- [96] NISHINO, K., KASAGI, N., AND HIRATA, M. Three-dimensional particle tracking velocimetry based on automated digital image processing. *Transactions of the ASME. Journal of Fluids Engineering 111* (1989), 384–91.
- [97] OTTINO J.M., DEROUSSEL, H., AND KHAKHAR, D., V. Mixing and dispersion of viscous liquids and powdered solids. *Adv. Chem. Engg 25* (1999), 105.

- [98] PAPANTONIOU, D., AND DRACOS, T. Lagrangian statistics in open channel flow by 3-D particle tracking velocimetry. *Engineering Turbulence Modelling and Experiments* (1990), 315–324.
- [99] PARKER, D. S., ASCE, A. M., KAUFMAN, W. J., AND JENKINS, D. Flocculation processes. *Journal of the Sanitary Engineering Division-asce* 98 (1972), 79–87.
- [100] PENG, S. J., AND WILLIAMS, R. S. Direct measurement of flocculation in flowing suspensions. *Journal of Colloid and Interface Science* 166 (1994), 321–332.
- [101] POTANIN, A. A. On the mechanism of aggregation in the shear-flow of suspensions. *Journal of Colloid and Interface Science* 145 (1991), 140–157.
- [102] POWELL, R. L., AND MASON, S. G. Dispersion by laminar flow. *AIChE Journal* 28 (1982), 286–293.
- [103] QURESHI, N. M., BOURGOIN, M., BAUDET, C., CARTELLIER, A., AND GAGNE, Y. Turbulent transport of material particles: an experimental study of finite size effects. *Phys. Rev. Lett.* 99 (2007), 184502–1–4.
- [104] RAPHAEL, M., AND ROHANI, S. Isoelectric precipitation of sunflower protein in a msmpr precipitator: Modeling of psd with aggregation. *Chemical Engineering Science* 51 (1996), 4879–4384.
- [105] SANDKUHLER, P., LATTUADA, M., WU, H., SEFCIK, J., AND MORBIDELLI, M. Further insights into the universality of colloidal aggregation. *Advances In Colloid and Interface Science* 113 (2005), 65–83.
- [106] SB. MORAN, P. Y., AND BALLS, P. On the role of colloids in trace metals solid-solution partitioning in continental shelf waters: A comparison of model results and field data. *Cont. Shelf Res.* 16 (1996), 397–408.
- [107] SCHMITT, F. G., AND SEURONT, L. Intermittent turbulence and copepod dynamics: Increase in encounter rates through preferential concentration. *Journal of Marine Systems* 70 (2008), Baltic Sea Res Inst.
- [108] SERRA, T., COLOMER, J., AND CASAMITJANA, X. Aggregation and breakup of particles in a shear flow. *Journal of Colloid and Interface Science* 187 (1997), 466–473.
- [109] SMITH, P. G., AND VANDEVEN, T. G. M. Shear-induced deformation and rupture of suspended solid liquid clusters. *Colloids and Surfaces* 15 (1985), 191–210.
- [110] SMOLUCHOWSKI, M. *Phys. Z.* 17 (1916), 585.
- [111] SMOLUCHOWSKI, M. *J. Phys.Chem* 92 (1917), 129.
- [112] SONNTAG, R. C., AND RUSSEL, W. B. Structure and breakup of flocs subjected to fluid stresses .1. shear experiments. *Journal of Colloid and Interface Science* 113 (1986), 399–413.
- [113] SOOS, M., EHRL, L., BAEBLER, M. U., AND MORBIDELLI, M. Aggregate breakup in a contracting nozzle. *Langmuir* 26 (2010), 10–18.
- [114] SOOS, M., MOUSSA, A. S., EHRL, L., SEFCIK, J., WU, H., AND MORBIDELLI, M. Effect of shear rate on aggregate size and morphology investigated under turbulent conditions in stirred tank. *Journal of Colloid and Interface Science* 319 (2008), 577–589.

- [115] SOOS, M., SEFCIK, J., AND MORBIDELLI, M. Investigation of aggregation, breakage and restructuring kinetics of colloidal dispersions in turbulent flows by population balance modeling and static light scattering. *Chemical Engineering Science* 61 (2006), 2349–2363.
- [116] SOOS, M., SEFCIK, J., AND MORBIDELLI, M. Master curves for aggregation and gelation: Effects of cluster structure and polydispersity. *Industrial & Engineering Chemistry Research* 46, 6 (Mar. 2007), 1709–1720.
- [117] SOOS, M., WANG, L., FOX, R. O., SEFCIK, J., AND MORBIDELLI, M. Population balance modeling of aggregation and breakage in turbulent taylor-couette flow. *Journal of Colloid and Interface Science* 307 (2007), 433–446.
- [118] SOOS, M., WU, H., AND MORBIDELLI, M. Taylor-couette unit with a lobed inner cylinder cross section. *AIChE Journal* 53 (2007), 1109–1120.
- [119] SPICER, P. T., KELLER, W., AND PRATSINIS, S. E. The effect of impeller type on floc size and structure during shear-induced flocculation. *Journal of Colloid and Interface Science* 184 (1996), 112–122.
- [120] TAMBO, N. Physical characteristics of flocs. *Water research* 13 (1979), 421–427.
- [121] TANG, S., PREECE, J. M., MCFARLANE, C. M., AND ZHANG, Z. Fractal morphology and breakage of dlca and rlca aggregates. *Journal of Colloid and Interface Science* 221 (2000), 114–123.
- [122] THOMAS, D. G. Turbulent disruption of flocs in small particle size suspensions. *AIChE Journal* 10 (1964), 517–523.
- [123] TOSCHI, F., AND BODENSCHATZ, E. Lagrangian properties of particles in turbulence. *Annual Review of Fluid Mechanics* 41 (2009), 375–404.
- [124] TSINOBER, A. *An Informal Introduction to Turbulence*. Kluwer Academic Publishers, 2001.
- [125] VAN DE VEN, T. *Colloidal hydrodynamics*. London Academic Press, 1989.
- [126] VANDEVEN, T. G. M., AND HUNTER, R. J. Energy-dissipation in sheared coagulated sols. *Rheologica Acta* 16 (1977), 534–543.
- [127] VASSILEVA, N. D., VAN DEN ENDE, D., MUGELE, F., AND MELLEMA, J. Fragmentation and erosion of two-dimensional aggregates in shear flow. *Langmuir* 23 (2007), 2352–2361.
- [128] VISSER, J. Measurement of force of adhesion between submicron carbon-black particles and a cellulose film in aqueous solution. *Journal of Colloid and Interface Science* 34 (1970), 26–32.
- [129] VOLK, R., CALZAVARINI, E., LEVEQUE, E., AND PINTON, J. F. Dynamics of inertial particles in a turbulent von karman flow. *Journal of Fluid Mechanics* 668 (2011), 223–235.
- [130] VOTH, G. A., LA PORTA, A., CRAWFORD, A. M., ALEXANDER, J., AND BODENSCHATZ, E. Measurement of particle accelerations in fully developed turbulence. *Journal of Fluid Mechanics* 469 (2002), 121–160.
- [131] WELLS, M. L., AND GOLDBERG, E. D. Occurrence of small colloids in sea-water. *Nature* 353 (1991), 342–344.

- [132] WILLIAMS, R. A., PENG, S. J., AND NAYLOR, A. In situ measurement of particle aggregation and breakage kinetics in a concentrated suspension. *Powder Tech.* 73 (1992), 75–83.
- [133] XU, H., AND BODENSCHATZ, E. Motion of inertial particles with size larger than kolmogorov scale in turbulent flows. *Physica D* 237 (2008), 2095–100.
- [134] YEUNG, A. K. C., AND PELTON, R. Micromechanics: A new approach to studying the strength and breakup of flocs. *Journal of Colloid and Interface Science* 184 (1996), 579–585.
- [135] ZACCONE, A., GENTILI, D., WU, H., AND MORBIDELLI, M. Shear-induced reaction-limited aggregation kinetics of brownian particles at arbitrary concentrations. *Journal of Chemical Physics* 132 (2010).
- [136] ZACCONE, A., WU, H., GENTILI, D., AND MORBIDELLI, M. Theory of activated-rate processes under shear with application to shear-induced aggregation of colloids. *Phys. Rev. E* 80 (2009).
- [137] ZEIDAN, M., XU, B. H., JIA, X., AND WILLIAMS, R. A. Simulation of aggregate deformation and breakup in simple shear flows using a combined continuum and discrete model. *Chemical Engineering Research & Design* 85 (2007), 1645–1654.
- [138] ZENG, L., BALACHANDAR, S., FISCHER, P., AND NAJJAR, F. Interactions of a stationary finite-sized particle with wall turbulence. *J. Fluid Mech.* 594 (2008), 271–305.
- [139] ZIMMERMANN, R., GASTEUIL, Y., BOURGOIN, M., VOLK, R., PUMIR, A., AND PINTON, J.-F. Rotational intermittency and turbulence induced lift experienced by large particles in a turbulent flow. *Phys. Rev. Lett.* 106 (2011), 154501.
- [140] ZIMMERMANN, R., GASTEUIL, Y., BOURGOIN, M., VOLK, R., PUMIR, A., AND PINTON, J.-F. Tracking the dynamics of translation and absolute orientation of a sphere in a turbulent flow. *Review of Scientific Instruments* 82 (2011), 033906.